

Mechanistic Insights into Alkane C-H
Activation and Functionalization by Metal
Oxide Surfaces and Organometallic Complexes

Thesis by

Mu-Jeng Cheng

In Partial Fulfillment of the Requirements for the

degree of

Doctor of Philosophy

CALIFORNIA INSTITUTE OF TECHNOLOGY

Pasadena, California

2012

(Defended May 18, 2012)

©2012

Mu-Jeng Cheng

All Rights Reserved

To my family and my wife

ACKNOWLEDGEMENTS

My Ph.D. journey is enriched and completed by the presence of several important individuals who help me either in my research or in my daily life, and accompany me through happiness and sadness of my days at Caltech. It is my great pleasure to acknowledge their support.

First, I would like to thank Prof. William A. Goddard III. I am extremely grateful to have Bill as my research advisor. During my entire Ph.D., Bill has always been very supportive and patient in guiding me and training me to become a better scientist. I have learned a great deal of knowledge from him in terms of how to choose a good research topic and how to execute and complete a project. I could not have accomplished what I have without him.

I would like to thank my thesis committee members: Prof. Harry Gray, Prof. Robert Grubbs, Prof. James Heath, and Prof. Aron Kuppermann. My committee is immensely supportive and helpful in giving me both excellent suggestions and encouragement. Especially, I would like to thank Prof. Aron Kuppermann for helping me and my family to go through the saddest days of our life.

I am very indebted to the current and former members in the Goddard group. I would like to thank Robert Nielsen (Smith) for being a good mentor, collaborator, and friend. I will forever remember the enormous time he spent to teach me scientific writing, computational chemistry, and organometallics. I would like to thank Jonathan Mueller and Hyungjun Kim for being my good friends, classmates, and colleagues. I would like to

thank Julius Su, Tod Pascal, Jonas Oxgaard, Kimberly Chenoweth, Adri van Duin, and Andres Jaramillo-Botero for their help in my research. I also would like to thank Patrick Theofanis, Qi An, Hai Xiao, Vaclav Cvicek, Wei-Guang Liu, Fan Liu, Himanshu Mishra, and Ross Fu. Their participation enriched my days in the Goddard group.

I would like to thank my collaborators, Prof. John Groves, Wei Liu, Prof. Periana, and Steven Bischof. I have learned a great deal of knowledge about alkane functionalization chemistry (radical or nonradical approach) from them. I would like to acknowledge Chevron-Texaco Energy Research and Technology Company and the Center for Catalytic Hydrocarbon Functionalization, an Energy Frontier Research Center, for supporting me financially.

I would like to thank my friends in the Taiwanese student community at Caltech: I-Ren Lee, Hsuan-Tien Lin, Bor-Ching Su, Chia-Chieh Chu, Chun-Yang Chen, Chi-Hao Liu, Jen-Kan Yu, and Tsui-Fen Chou. The time we shared brought a lot of fun to my Ph.D. journey. I will always remember the day that I-Ren Lee and Hsuan-Tien Lin picked me up from LAX and helped me to setup when I arrived in LA at June 30th 2005.

I would like to thank my parents and my parents-in-law for their support and encouragement. I would like to thank my brother and sister for taking care of my father. Finally and most importantly, I would like to thank my wife Kuang-Jung Chang for accompanying me and making my Ph.D. a wonderful voyage.

ABSTRACT

Alkanes are the major components of natural gas and petroleum; however, there are only few practical processes that can functionalize them into more valuable products such as alkene or alcohols. The reason for this difficulty is because alkanes possess strong and inert C-H bonds. The development of such a process that can convert alkanes to other more valuable functionalized hydrocarbons in a catalytic fashion would produce enormous economic benefits. The key to achieve this goal is to develop a proper catalyst. The catalysts can be organometallic complexes or metal oxide surfaces that catalyze alkane C-H activation and functionalization in homogeneous or heterogeneous conditions.

In this thesis, we apply quantum mechanics to study the known alkane functionalization reactions to provide more insight into those catalytic processes, and we further utilize our computational results to design new reaction pathways for alkane functionalization. Each chapter presented herein constitutes an independent publication focusing on different aspects of the problem.

Chapter 1: Single-Site Vanadyl Activation, Functionalization, and Reoxidation Reaction Mechanism for Propane Oxidative Dehydrogenation on the Cubic V₄O₁₀ Cluster: Vanadium oxide is a powerful heterogeneous catalyst that can convert oxidative dehydrogenation

(ODH) of propane. Despite numerous studies, either computational or experimental, on this topic, no complete catalytic cycle is provided. In this paper, we examined the detailed mechanism for propane reacting with a V_4O_{10} cluster to model the catalytic oxidative dehydrogenation (ODH) of propane on the $V_2O_5(001)$ surface. We reported the mechanism of the complete catalytic cycle, including the regeneration of the reduced catalyst using gaseous O_2 , in which only a single vanadyl site is involved. This mechanism is applicable to propane ODH on the supported vanadium oxide catalysts where only monovanadate ($O=V-(O)_4^-$) species is present.

Chapter 2: The Magnetic and Electronic Structure of Vanadyl Pyrophosphate from Density Functional Theory: We have studied the magnetic structure of the high-symmetry vanadyl pyrophosphate, focusing on the spin exchange couplings, applying density functional theory with exact exchange and the full three-dimensional periodicity to this system for the first time. Based on the local density of states and the response of spin couplings to varying the cell parameter a , we found that two major types of spin exchange couplings originate from different mechanisms: one from a super-exchange interaction and the other from a direct exchange interaction. Based on the variations in V–O bond length as a function of strain along a , we found that the V–O bonds of $V-(OPO)_2-V$ are covalent and rigid, whereas the bonds of $V-(O)_2-V$ are fragile and dative.

Chapter 3: The *Para*-Substituent Effect and pH-Dependence of the Organometallic Baeyer-Villiger Oxidation of Rhenium-Carbon Bonds:

Organometallic Baeyer-Villiger represents another means of oxidizing M-R to M-OR. In this work, we conducted a series of calculations with the goal of providing more insights into the reaction. We find that during this organometallic BV oxidation, the migrating phenyl plays the role of a nucleophile and the leaving group OH is nucleophile. Moreover, we also find that for R = Ph the reaction rate is much faster than that for R = Me, which is later confirmed by experiments.

Chapter 4: Carbon-Oxygen Bond-Forming Mechanisms in Rhenium Oxo-Alkyl Complexes: Intramolecular 1,2-migration of hydrocarbyl across metal-oxo bonds is one of the few means of oxy-functionalizing M-R to M-OR bonds. This strategy works for R = Ph, but fails for R = Me and Et. In this work, we study these systems with the goal of understanding the reason. We find that when R = Me and Et the α -hydrogen is very acidic and easy to abstract even with weak base, such as the counter ion of the complex, leading to unwanted by-products. We find that these side reactions can be avoided by two means: (1) use counter ions with weaker basicity to increase proton abstraction barriers, and (2) use R = *i*Pr, which has a higher migratory aptitude, to accelerate the 1,2-migration rate.

Chapter 5: A Homolytic Oxy-Functionalization Mechanism: Intermolecular Hydrocarbyl Migration from M-R to Vanadyl Oxo: Oxy-functionalization $M^{\delta+}-R^{\delta-}$ to M-OR bonds is one of the key challenges in the development of hydrocarbon hydroxylation catalysts. This can be achieved by

limited means: (1) organometallic Baeyer-Villiger oxidation, and (2) intramolecular 1,2-migration of hydrocarbyl across metal-oxo bonds. In this work, we have examined C-O bond formation in the reaction of OVCl_3 with Ph_2Hg to generate phenol using quantum mechanics. Surprisingly, we find this reaction is through an unprecedented bimolecular, one-electron oxidation of the V-Ph bond by a second V=O moiety, not through the experimentally proposed intramolecular phenyl 1,2-migration across V=O bonds. Our calculations on the oxidation of Rh-CH₃ and Ir-CH₃ complexes by OVCl_3 further suggest that the possibility of integrating this new oxidation mechanism into alkane oxidation catalytic cycles. We also give guidelines to choose the systems in which this oxidation mechanism may play an important role.

TABLE OF CONTENTS

Acknowledgements	iv
Abstract	vi
Table of Contents	x
List of Tables	xiii
List of Figures	xiv
Chapter 1: Single-Site Vanadyl Activation, Functionalization, and Reoxidation Reaction Mechanism for Propane Oxidative Dehydrogenation on the Cubic V₄O₁₀ Cluster	1
1.1 Introduction	1
1.2 Computational Details	6
1.3 Results	7
1.4 Discussion	29
1.5 Conclusions	36
1.6 References	37
Chapter 2: The Magnetic and Electronic Structure of Vandyl Pyrophosphate from Density Functional Theory	42
2.1 Introduction	42
2.2 Computational Details	45
2.3 Results and Discussion	47
2.4 Conclusions	59

	xi
2.5 Appendix	60
2.6 Notes and References.....	62
 <i>Chapter 3: The Para-Substituent Effect and pH-Dependence of the Organometallic Baeyer-Villiger Oxidation of Rhenium-Carbon Bonds</i>	
Bonds	65
3.1 Introduction	65
3.2 Results and Discussion	66
3.3 Conclusions	77
3.4 Computational Details	78
3.5 Notes and References.....	79
 <i>Chapter 4: Carbon-Oxygen Bond-Forming Mechanism in Rhenium Oxo-Alkyl Complexes</i>	
Oxo-Alkyl Complexes	84
4.1 Introduction	84
4.2 Computational Details	86
4.3 Results and Discussion	87
4.4 Conclusions	103
4.5 Notes and References.....	103
 <i>Chapter 5: A Homolytic Oxy-Functionalization Mechanism: Intermolecular Hydrocarbyl Migration from M-R to Vanadyl Oxo</i>	
Intermolecular Hydrocarbyl Migration from M-R to Vanadyl Oxo	106
5.1 Introduction	106
5.2 Results and Discussion	107
5.3 Conclusions	116
5.4 Computational Details	117

5.5 References	118
----------------------	-----

*Appendix A (unpublished results): Explanation of the Dramatic Difference between the Mechanism of Activation and Functionalization of Methane by Ru(II) and OsII/Re: Guidelines for Improved Catalysts.....*121

A.1 Introduction	121
A.2 Computational Details and Evaluations	123
A.3 Results and Discussion	127
A.4 Conclusions	158
A.5 References	159

*Appendix B (future work): A Computational Study on the Catalytic Oxidation of n-Butane to Maleic Anhydride by Vanadium Phosphorus Oxide.....*162

B.1 Project Overview.....	162
B.2 Specific Aims	163
B.3 Background and Significance.....	163
B.4 Preliminary Work.....	173
B.5 Research Design and Methods	178
B.6 Reference.....	187

LIST OF TABLES

<i>Number</i>	<i>Page</i>
2.1 Relative energies for various spin configurations of VOPO	52
2.2 Comparison between experimental and theoretical predicted values of <i>J</i> parameters in the high symmetry, high pressure form of VOPO	53
3.1 Gibbs free energy surfaces of the BV oxidation of <i>p</i> -X-C ₆ H ₄ -ReO ₃ (X = CF ₃ , CH ₃ , OCH ₃ , OH, and NH ₂) by H ₂ O ₂ at pH = 7 including aqueous solvation	74
4.1 The reaction barrier and energy for alkyl 1,2-migration at 298K.....	91

LIST OF FIGURES

<i>Number</i>	<i>Page</i>
1.1 The three types of oxygen atoms on the $V_2O_5(001)$ surface where the vanadium atoms are shown in gray and oxygen atoms are represented as white circles.	3
1.2 Structural parameters for the singlet state and triplet state of the V_4O_{10} cluster.....	5
1.3 Reaction pathways and energies (ΔE) for initial C-H bond activation of methane (the number in parenthesis is $\Delta H_{0K} = \Delta E + ZPE$).	11
1.4 The first and second steps of propane ODH on V_4O_{10}	16
1.5 The three pathways for binding of iso-propyl radical (<i>iPr</i>) to the V_4O_{10} followed by the second hydrogen abstraction to release the propene product.	17
1.6 Energy profiles for propane ODH on V_4O_{10}	19
1.7 Structural parameters for the intermediates and transition states of the vanadium reoxidation step.	20
1.8 The structure parameters and relative energy for the lowest singlet, triplet, and quintet states of 6	23
1.9 The catalytic cycle for propane ODH on V_4O_{10} derived from the QM calculations.	27
2.1 Polyhedral views of the crystal structure of VOPO and the schematic description of the spin exchange couplings.....	44
2.2 Calculated band structure of VOPO	48
2.3 The projected density of states for V, O(1), and O(2) atoms superimposed on the total density of states for VOPO	50
2.4 The dependence of spin couplings on the cell parameter <i>a</i>	55
2.5 The dependence of the spin coupling on the V-V distance in the $V_2O(3)_2$ cluster model.....	58

3.1 Variation of the fragment Mulliken charges along the BV intrinsic reaction coordinate based on M06/LACVP** level with solvent effect....	73
3.2 Correlations between the coordination energies and phenyl migration barrier to the Hammett's parameter of X	73
3.3 Correlations between the reaction rates at different pH to the Hammett's parameter of X	75
4.1 Free energy surface of Ph 1,2-migration (kcal/mol) at 298K.....	89
4.2 Free energy surface of α - and β -hydrogen abstraction by oxo (kcal/mol) at 298K	93
4.3 Free energy surface of α - and β -hydrogen abstraction by external base, OTf (kcal/mol) at 298K	95
4.4 Free energy surface of the acetaldehyde formation through the oxo-ethylidene coupling pathway (kcal/mol) at 298K.....	98
4.5 Free energy surfaces of the acetaldehyde formation through direct oxygen transfer from DMSO (kcal/mol) at 298K.....	99
4.6 Overall free energy surface of the oxidation of (HBpz ₃)ReO(Et)(OTf) by DMSO (kcal/mol) at 298K.....	100
4.7 Free energy surface of the H ₂ O and NH ₃ nucleophilic attack on (HBpz ₃)ReO(OH)(CHCH ₃)+1 (kcal/mol) at 298K	101
5.1 The comparison of three intramolecular phenyl metal-to-oxo migrations (Intra-M ^{2e} , free energies in kcal/mol).....	108
5.2 The free energy surface of the phenyl intermolecular migration from OVPhCl ₂ to the oxo of O=VCl ₃ (kcal/mol).....	109
5.3 The comparison of the new oxy-functionalization to previous proposed mechanisms	111
5.4 The free energy surface of the methyl intermolecular migration from VOMeCl ₂ to the oxo of VOCl ₃ (kcal/mol).....	112
5.5 Possible mechanisms involving a vanadyl oxidant in a hydrocarbon oxidation cycle using CH ₄ as the substrate.....	113

5.6 Gibbs free energy surface (kcal/mol) for methane functionalization by Rh and Ir pincer complexes and OVCl_3 at 298K in aqueous solution at pH = 0 (Rh) or pH = 4 (Ir)	115
--	------------

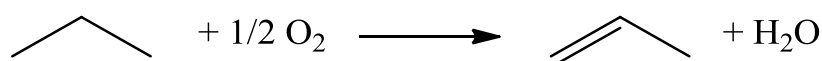
**SINGLE-SITE VANADYL ACTIVATION, FUNCTIONALIZATION, AND
REOXIDATION REACTION MECHANISM FOR PROPANE OXIDATIVE
DEHYDROGENATION ON THE CUBIC V₄O₁₀ CLUSTER**

1.1 Introduction

Selective oxidation of saturated hydrocarbons (ethane, propane, butane) to feedstocks for polymers and chemicals is increasingly important for both economic and environmental reasons. However, activation and selective production of products has been much more of a challenge for these saturated hydrocarbons than for unsaturated systems (ethene, propene, butene). Even so, industrially successful heterogeneous catalysts have been developed, including vanadium phosphorous oxide (VPO) for conversion of *n*-butane to maleic anhydride, and mixed metal oxide (MMO) catalysts for selective oxidation and ammoxidation of propene to acrolein and acrylonitrile. In all of these systems, there is considerable uncertainty about the detailed chemical mechanism involved, which has made improvements and optimization difficult. Characteristic of the catalysts listed above is the use of vanadyl oxide to activate the very strong bond of the saturated alkanes. As a starting point for determining the mechanism, we chose to start with V₂O₅ and the oxidative dehydrogenation of propane to propene.

Dehydrogenation of alkanes to give the corresponding alkenes and H₂ is strongly endothermic and can be carried out only at temperatures above 900 K.¹⁻³ In addition to

being uneconomical, these high reaction temperatures cause unwanted side reactions, leading to coke formation. In contrast, the oxidative dehydrogenation (ODH) reaction is an attractive alternative to simple dehydrogenation, because it is exothermic due to the formation of water.¹



However, a selective catalyst is required to avoid complete oxidation to CO_2 and CO . Currently, the best alkane ODH catalysts contain either dispersed vanadia or particles of V_2O_5 that have a variety of vanadium coordination geometries and oxidation states, ranging from +2 to +5.³

Figure 1.1 shows the structure of the V_2O_5 (001) surface, the most stable surface of the bulk V_2O_5 . This surface includes three types of oxygen atoms: (a) O(1) is bonded to one V, forming a double bond, with a bond distance of $V=O(1) = 1.58 \text{ \AA}$; (b) O(2) is bonded to two V, forming two single bonds: $V-O(2)-V$ with bond lengths of $V-O(2) = 1.78 \text{ \AA}$; and (c) O(3) is coordinated to three V but with two bond $V-O(3)$ distances of 1.88 \AA , somewhat longer than a single bond (1.78 \AA) and one much longer distance ($V-O(3) = 2.02 \text{ \AA}$), which we consider as a donor-acceptor or coordination bond.

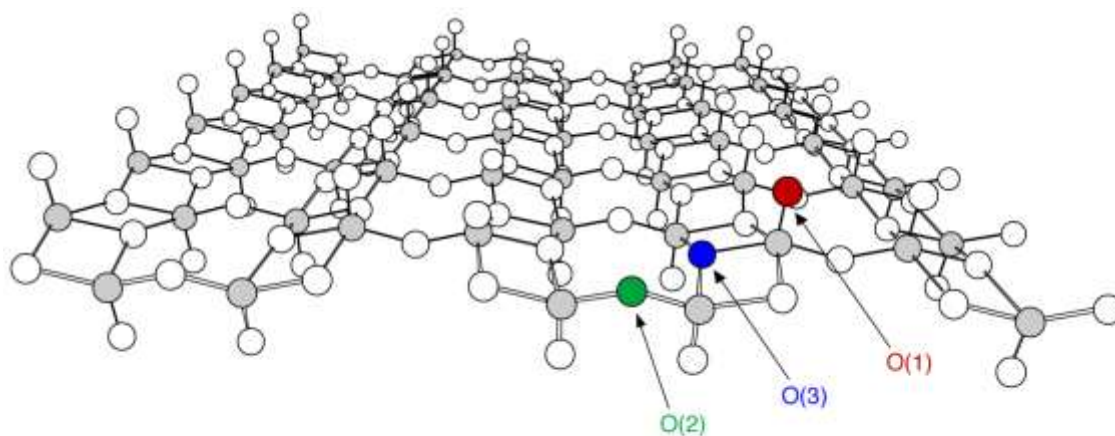


Figure 1.1 The three types of oxygen atoms on the $V_2O_5(001)$ surface where the vanadium atoms are shown in gray and oxygen atoms are represented as white circles. The bonding types $V=O(1)$, $V-O(2)-V$ are in the V_4O_{10} cluster, but not the $O(3)$.

Experimental studies have provided some insight into the mechanism of alkane ODH.¹⁻¹⁶ Most studies have focused on the alkane ODH on supported vanadium oxides rather than bulk V_2O_5 , because highly dispersed vanadium oxides on supports display higher selectivity (29-90%) than the bulk V_2O_5 (18-31%).^{2,3,11,17} Went *et al.*⁴ used laser Raman spectroscopy to investigate supported vanadium oxide catalysts (V_2O_5/SiO_2 , V_2O_5/TiO_2 , and V_2O_5/Al_2O_3) and found that three vanadia species, monovanadate, one- and two-dimensional vanadate chains (polyvanadate), and crystallites of V_2O_5 were present on the supports depending on the V_2O_5 loading, which has been confirmed in more recent experimental results.¹¹ On the basis of the relationship between the ethylene turnover rate and vanadium oxide concentration on an SiO_2 support, Oyama⁷ concluded that only a

single vanadium center is necessary for ethane ODH. These conclusions are consistent with the results obtained by Busca *et al.*¹⁰ and Kung.⁹ Recently, Pieck *et al.*¹⁶ studied propane ODH on V_2O_5/ZrO_2 catalysts and showed that monovanadates have both higher activity and better selectivity to propene than bulk V_2O_5 and polyvanadates. In contrast, Khodakov *et al.*¹¹ found that the polyvanadate structures are significantly more active than monovanadate structure. It is not clear whether the ODH reaction occurs on mono- or polyvanadate sites, but it appears likely that these sites are more important than crystalline V_2O_5 .

Several studies give hints about the individual steps. Le Bars *et al.*⁸ carried out a calorimetric experiment of ethane ODH on unsupported V_2O_5 to show that O_2 is important in regenerating the vanadia surface and maintaining a high olefin yield, most likely by keeping vanadium in its highest oxidation state. Chen *et al.*^{12,13} used deuterium and ^{13}C isotopes to study the reaction pathways of propane ODH on V_2O_5/ZrO_2 catalysts. The authors determined that the C-H bond activation step is irreversible and that the methylene C-H bond of propane is activated in the rate-determining step.^{12,13} Argyle *et al.*^{14,15} measured the activation barrier for both propane and ethane ODH on alumina-supported vanadia and found both to be 27.0 kcal/mol. It has generally been assumed that the oxygen reacting with the alkane comes from the lattice and the reduced catalyst is reoxidized by gaseous O_2 , which is referred to as a Mars-van Krevelen model.^{12,13,18,19} Computational studies on related systems reported by Gilardoni *et al.*,²⁰ Redfern *et al.*,²¹ and Fu *et al.*²² are described in the discussion section.

Because of the considerable uncertainties in the details of the reaction mechanism for these systems, we determined the propane ODH mechanisms on the cubic V_4O_{10} cluster (**Figure 1.2**). We examined both the mechanism for activating the C-H bond of propane with subsequent formation of propene and the mechanism for reoxidation of the reduced vanadium oxide catalyst.

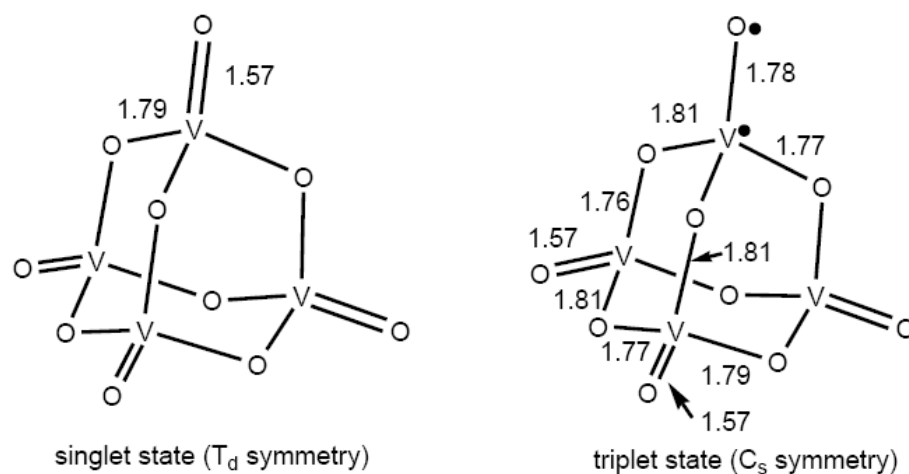


Figure 1.2 Structural parameters for the singlet state and triplet state of the V_4O_{10} cluster. The singlet state has T_d symmetry, whereas the triplet state has C_s symmetry ($3A'$).

Although we believe that most of the chemistry of the V_2O_5 (001) surface is captured by the V_4O_{10} model, it is not a perfect model for the surface because it contains only O(1)- and O(2)-like oxygens. However, we believe that the results from the V_4O_{10} model are directly applicable to mechanisms for supported vanadia catalysts, where the relevant chemistry is

likely to take place at a single site. In particular, this paper aims to answer the following questions: (1) How do the structural parameters, vibrational spectra, and electronic states of the V_4O_{10} cluster compare to the V_2O_5 (001) surface? (2) What is the mechanism for C-H activation of alkanes? (3) What are the subsequent steps for formation of propene and H_2O products? (4) By what mechanism is the surface reoxidized? (5) Can we find a coherent mechanistic cycle from theory that is consistent with available experimental results on the V_2O_5 crystal?

1.2 Computational Details

Our DFT calculations used the B3LYP functional,²³ which combines exact HF exchange with the Becke generalized gradient exchange functional of Becke²⁴ (B) and the Lee, Yang, and Parr²⁵ (LYP) correlation functional. This functional is known to provide a good description of the potential energy surface (PES) of transition metal-containing compounds.²⁶⁻³⁶ The metals were described using the Wadt and Hay³⁷ core-valence (relativistic) effective core potential (treating the 13 electrons in $3s$, $3p$, and $3d$ orbitals of V explicitly) with the valence double- ζ contraction of the basis functions (denoted as LACVP** in Jaguar). All electrons were included on the H, C, and O atoms using a modified variant of the Pople^{38,39} 6-31G** basis set.

The analytic Hessian was calculated for each local minimum and each transition state and used to calculate the vibrational frequencies. We ensured that each local minimum had

zero imaginary frequencies, while each transition state structure had one imaginary frequency. These vibrational frequencies were used to calculate the zero-point energy (ZPE) to obtain enthalpies at 0 K for each structure and to calculate the enthalpy and entropy corrections to obtain the Gibbs free energy at 298.15 K. All calculations were performed using the Jaguar 6.5 program package.⁴⁰

1.3 Results

V₄O₁₀ Cluster Model The V₄O₁₀ (1) cluster in **Figure 1.2** can be considered as a topological equivalent of the top surface layer of the V₂O₅ (001) surface mapped onto a sphere. This cluster contains the vanadyl V=O(1) site and the V-O(2)-V site, but does not contain the three-fold coordinated oxygen O(3) site. However, the crystal structure⁴¹ shows that this site has two short V-O(3) bonds of 1.88 Å, similar to the V-O(2) bonds (1.78 Å), which we consider as partially ionic-covalent bonds, while the third V-O(3) bond length is 2.02 Å, which we consider as a donor-acceptor bond. This means that O(3) is connected with two covalent bonds instead of three. Therefore, we consider the V₂O₅ (001) surface to have one V=O(1) bond and three V-O(2) bonds, making it structurally similar to our V₄O₁₀ cluster model. All vanadium atoms in V₄O₁₀ have a formal oxidation state of +5, with each vanadium atom connected through an O(2) to three V^V. Thus, we consider the V₄O₁₀ cluster suitable for modeling the chemistry of the V₂O₅ (001) surface.

Figure 1.2 shows the structural parameters of the singlet of V_4O_{10} (**1**). The bond distances are $V=O(1) = 1.57 \text{ \AA}$ and $V-O(2) = 1.79 \text{ \AA}$, in good agreement with the experimental values of $V=O(1) = 1.58 \text{ \AA}$ and $V-O(2) = 1.78 \text{ \AA}$ obtained for the bulk V_2O_5 .⁴¹ Periodic DFT calculations on the $V_2O_5(001)$ surface also lead to $V=O(1) = 1.59 \text{ \AA}$ and $V-O(2) = 1.80 \text{ \AA}$.⁴²

We consider that the $V=O(1)$ bond involves six electrons: two from the V [say in the $(d_{xz}) (d_{yz})$ configuration] and four from the O [say in the $(p_z)^2(p_x)(p_y)$ configuration], leading to a bond that can be considered as a double bond plus a donor acceptor bond. Thus, the ground state is $(\sigma)^2(\pi_x)^2(\pi_y)^2$, where σ has a_1 symmetry and (π_x, π_y) belongs to the e irreducible representation, in the C_{3v} point group. Thus we will write this configuration as $(\sigma)^2(\pi)^4$. Then we consider that each V makes three somewhat polar covalent bonds to the three O(2) neighbors.

The Mulliken populations of V_4O_{10} are $Q_V = 1.41$, $Q_{O(1)} = -0.31$, and $Q_{O(2)} = -0.73$ electrons. This is in good agreement with the values of $Q_V = 1.46$, $Q_{O(1)} = -0.39$, and $Q_{O(2)} = -0.71$ electrons derived from analyzing the electrostatic fields. Thus, each $V-O(2)$ bond can be considered to have a charge transfer of $0.37 e^-$ from V to O, while the net transfer in the $V=O(1)$ bond is only $0.31 e^-$ despite two partially polar covalent bonds. This is because of back transfer in the donor-acceptor bond. We should point out that the small charge transfer from V to O is due to the high oxidation state. For the $V=O$ diatomic, we would expect more charge transfer. We calculated four vibrational frequencies in the range of $1126-1149 \text{ cm}^{-1}$ for the $V=O(1)$ bond stretch, consistent with experimental values of 1040 cm^{-1} for bulk V_2O_5 ,⁴³ 1010 cm^{-1} for V_2O_5/ZrO_2 ,¹⁶ and 1042

cm⁻¹ for V₂O₅/SiO₂.⁴⁴

We also calculated the triplet state of V₄O₁₀. Here we expect a $\pi \rightarrow \pi^*$ transition (that is $e \rightarrow e^*$) in one of the V=O(1) bonds, leading to a $(\sigma)^2(\pi)^3(\pi^*)^1$ configuration. For the C_{∞v} point group this would lead to four states: ³Σ⁺, ³Δ, and ³Σ⁻ (in increasing energy), which become ³A₁, ³E, and ³A₂ in C_{3v}. Thus the lowest triplet state would lead to a distortion from the Td symmetry of the ground state to C_{3v}. However to obtain these correct symmetries requires two configuration wavefunctions (e.g., [$\pi_x^2 \pi_y \pi_y^* + \pi_x \pi_x^* \pi_y^2$]). Our QM calculations use a single configuration and hence would mix the ³Σ⁺ and ³Δ⁺ states, which should lower the symmetry to C_s, with degenerate states of the A' and A'' irreducible representation.

The triplet state has both unpaired electrons localized on one V=O(1) group, as expected, with 0.75 unpaired spin on the on the V atom and 0.94 unpaired spin on the O(1) atom, consistent with slight polarity in the bond. This V=O(1) bond elongates from 1.57 to 1.78 Å, as expected since the total bond order is 1 rather than 2. [The other V=O(1) bond lengths do not change from the value in the singlet state.] In addition, the distance of one of the three V-O(2) bonded to the excited V=O increases to 1.81 Å, while the other two decrease to 1.77 Å (**Figure 1.2**).

The singlet-triplet gap is $\Delta E_{S-T} = E_{\text{Triplet}} - E_{\text{Singlet}} = 47.2$ kcal/mol, which is 12% lower than the experimental band gap for V₂O₅ crystal of 53.0-54.4 kcal/mol.^{45,46} This may be because that the V₄O₁₀ cluster permits the triplet state to relax more completely than in the bulk crystal. Indeed, using the ground state geometry, vertical triplet excitation energy is 61.6 kcal/mol, suggesting that the relaxation is responsible for this discrepancy.

Based on the structural and energetic similarities of the V_4O_{10} cluster to V_2O_5 (001), we conclude that the V_4O_{10} cluster is a plausible model for studying both the initial C-H activation of alkane ODH reaction on V_2O_5 (001) surface and for gaining insight into the whole mechanism.

C-H Bond Activation In order to reduce computational expense, the initial investigations on C-H activation were performed with the smaller CH_4 system. Four possible mechanisms of C-H bond activation were studied, including two types of addition reactions, which involve heterolytic C-H bond cleavage, and two types of hydrogen abstraction reactions, which involve homolytic C-H bond cleavage. The optimized geometries and the calculated energies of the four pathways are summarized in **Figure 1.3**.

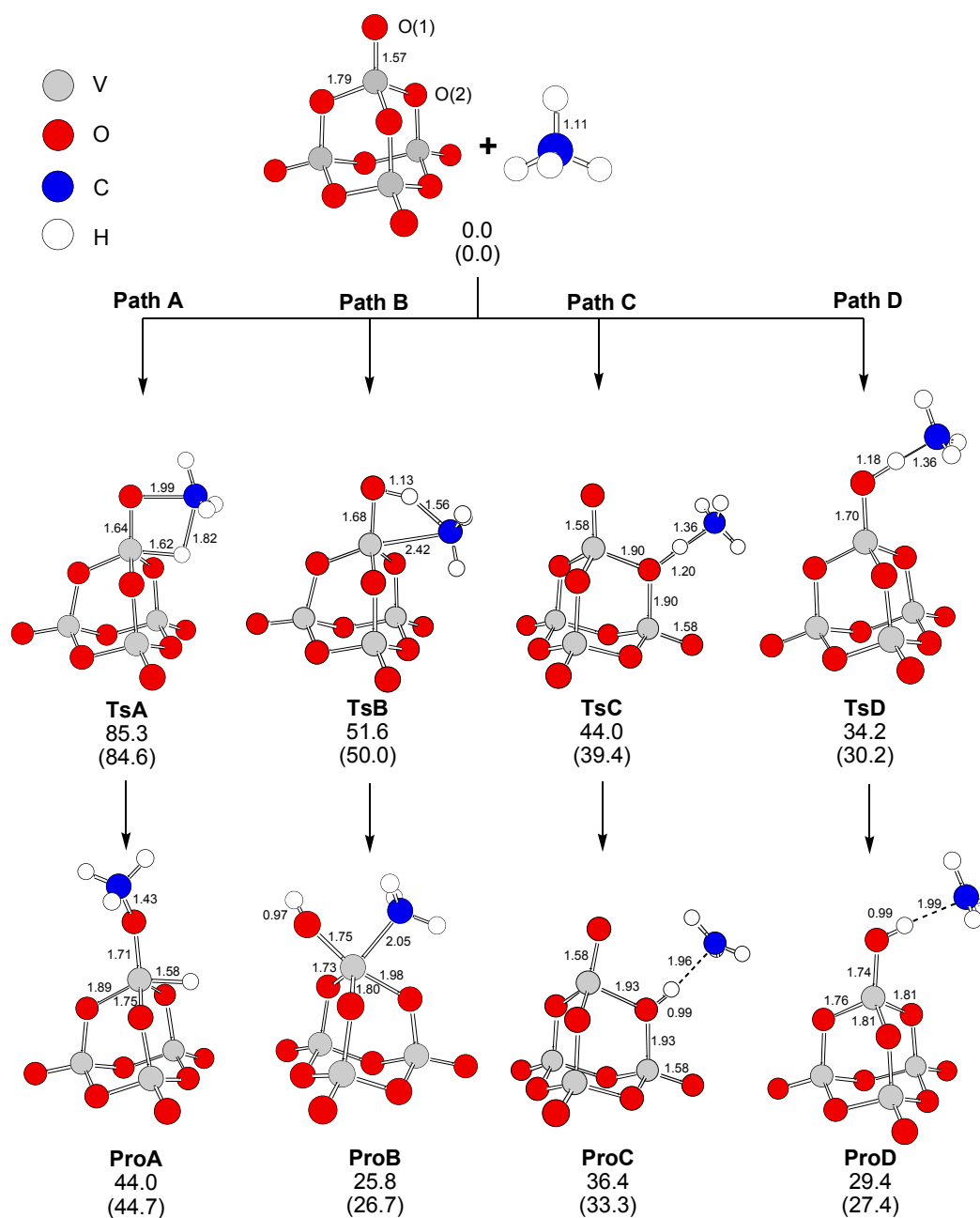


Figure 1.3 Reaction pathways and energies (ΔE) for initial C-H bond activation of methane (the number in parenthesis is $\Delta H_{0\text{K}} = \Delta E + \text{ZPE}$). The H abstraction by V=O(1), Path D, is clearly the most favorable process, although **ProB** is lower than **ProD**.

Path A involves an addition reaction utilizing the V=O(1) group, where the methyl group binds to O(1) and the hydrogen atom binds to the V atom. In the transition state structure (**TsA**), the V=O(1) bond elongates from 1.57 to 1.64 Å; the C-H bond distance of methane elongates from 1.11 to 1.82 Å. The CH₃-O(1) and H-V bond distances are 1.99 and 1.62 Å, respectively. Vanadium hydride and an adsorbed methoxy are formed in the product (**ProA**) with CH₃-O(1), H-V, and V-O(1) bond distances of 1.43, 1.58, and 1.71 Å, respectively. Two of the three V-O(2) bond distances increase to 1.89 and 1.85 Å, while the other decreases to 1.75 Å. The activation barrier for **Path A** is 85.3 kcal/mol, which is highest among four pathways discussed here.

Path B is also a V=O(1) addition reaction, but with the methyl group attaching to vanadium atom and the hydrogen atom attaching to the O(1) atom. In the transition state (**TsB**), the V=O(1), C-H, H-O(1), and CH₃-V bond distances are 1.68, 1.56, 1.13, and 2.42 Å, respectively. Vanadium carbide and an adsorbed hydroxyl are formed in the product, **ProB**, with V=O(1), H-O(1), and CH₃-V(1) bond distances of 1.75, 0.97, and 2.05 Å, respectively. A significant structural change was observed where one of the three V-O(2) bonds elongates to 1.98 Å, while the other two bond distances are 1.73 and 1.80 Å, similar to those of the V₄O₁₀ reactant. The barrier for **Path B** is still quite high (51.6 kcal/mol), but it is much smaller than that for **Path A**, probably due to better electrostatic interactions (V^{δ+}-C^{δ-} and O^{δ-}-H^{δ+}). Nevertheless, we conclude that the V=O(1) addition reactions are sufficiently unfavorable energetically that they need not be considered for the alkane ODH reaction mechanism.

Paths C and D involve hydrogen abstraction reactions. Both reactions led to transition

states and products having diradicaloid electronic structures, which we described as open-shell singlet states. In **Path C**, the bridging oxygen O(2) abstracts the hydrogen atom from methane. The O(2)-H and H-CH₃ bond distances in the transition state (**TsC**) are 1.20 and 1.36 Å, respectively. The bond distances between the O(2) and the two neighbor V atoms are both 1.90 Å, which are 0.11 Å longer than those in the V₄O₁₀ structure. There is no significant change in the four V=O(1) bond distances. The $\langle S^2 \rangle$ is equal to 0.83, indicating a slight correlation of the spins, but overall we consider this state as diradicaloid. The structure of the product (**ProC**) is very similar to that of **TsC** but with the O(2)-H bond decreased to 0.99 Å and the H-CH₃ distance increased to 1.96 Å. It can be described as a radical pair with very weak interactions between the two radical fragments, with $\langle S^2 \rangle = 1.05$. We also calculated the triplet state of **ProC** and found that both the structure and the energy are almost identical to those of the singlet state (RMSD of singlet/triplet bonds = 0.0002 Å, triplet energy is 0.02 kcal/mol lower than the singlet energy). The reaction barrier for **Path C** is 44.0 kcal/mol, which is 7.6 kcal/mol lower than **Path B** (and 41.3 kcal/mol lower than **Path A**).

Path D uses the terminal oxygen O(1) to abstract the hydrogen atom from methane, going through transition state structure **TsD**, where V-O(1) = 1.70, O(1)-H = 1.18, and H-CH₃ = 1.36 Å. The corresponding product (**ProD**) has bond distances of V=O(1) = 1.74, O(1)-H = 0.99, and H-CH₃ = 1.99 Å. Both **TsD** and **ProD** have a nonzero $\langle S^2 \rangle$ (0.82 for **TsD** and 1.01 for **ProD**), similar to the corresponding values in **Path C**. Thus, **TsD** is a diradicaloid structure, and **ProD** is also a radical-paired molecule very similar the corresponding triplet state (RMSD of singlet/triplet bond lengths = 0.002 Å. The triplet energy is 0.3 kcal/mol higher than singlet energy). **The activation barrier for this**

pathway is only 34.2 kcal/mol, which is the most energetically favorable pathway among the four reactions studied here. This should be contrasted with the reaction of methane with $V_4O_{10}^+$ investigated by Feyel et al.⁴⁷, where there is no barrier for the hydrogen migration from methane to O(1). This indicates that the chemistry is very different between cationic and neutral V_4O_{10} .

Thus we conclude that hydrogen abstraction pathways are much more favorable than the addition pathways. This is reasonable since the π bond of V=O(1) has a singly occupied orbital available to bond to the H and pointing toward it, whereas for O(2) the orbital overlapping the H is a filled lone pair orbital. In addition, the hydrogen abstraction reactions have the σ -orbital of C-H bond aligned with the lone pair electrons orbital of O(1) or O(2), so that there is no orbital alteration during the reaction process. In contrast, the addition reaction requires the σ -orbital of C-H bond in methane to break almost completely before it can overlap with the filled lone pair orbital on oxygen and the empty d -orbital on vanadium, leading to a high barrier. Based on the C-H activation of methane on the V_4O_{10} model, **we conclude that hydrogen abstraction by O(1) is the most likely first step for alkane ODH reaction on the $V_2O_5(001)$ surface**, and thus we consider it as the initial step for the propane ODH mechanism.

Oxidative Dehydrogenation of Propane on V_4O_{10} Next we consider the propane ODH reaction on V_4O_{10} leading to propene and $V_4O_{10}H_2$. We consider four important steps for each possible reaction pathway:

- **Vanadyl-H^{1st}-abs:** An hydrogen atom is abstracted from the methylene group in propane by V=O(1) to form a singlet radical-paired intermediate.

- **Spin conversion:** The electronic state of the intermediate changes from the singlet to the energetically nearly degenerate triplet state ($\Delta E_{S-T} \sim 0.1$ kcal/mol).
- **Radical trapping:** The *iso*-propyl radical bonds with one of the oxygens [O(1)H or O(2)] to form a triplet intermediate.
- **Propene formation:** O(2), O(1)H, or O(1) is used to abstract the second hydrogen from a methyl group to form propene and $V_4O_{10}H_2$.

The energetics and structures for step 1 and 2 are summarized in **Figure 1.4**, while the results for step 3 and 4 are shown in **Figure 1.5**. **Figure 1.6** shows the potential energy surfaces of the four possible reaction pathways.

Based on the barriers for C-H activation in methane, *we expect the initial step in propane ODH to be hydrogen abstraction of the methylene hydrogen from propane by the $V=O(1)$ site, producing an iso-propyl radical (vanadyl- H^{1st} -abs step)*. We calculate an activation energy for this reaction of 23.9 kcal/mol (**Figure 1.4**), which is in good agreement with the experimental barrier of propane ODH on supported vanadium oxides ($E_a=27.0$ kcal/mol).^{14,15}

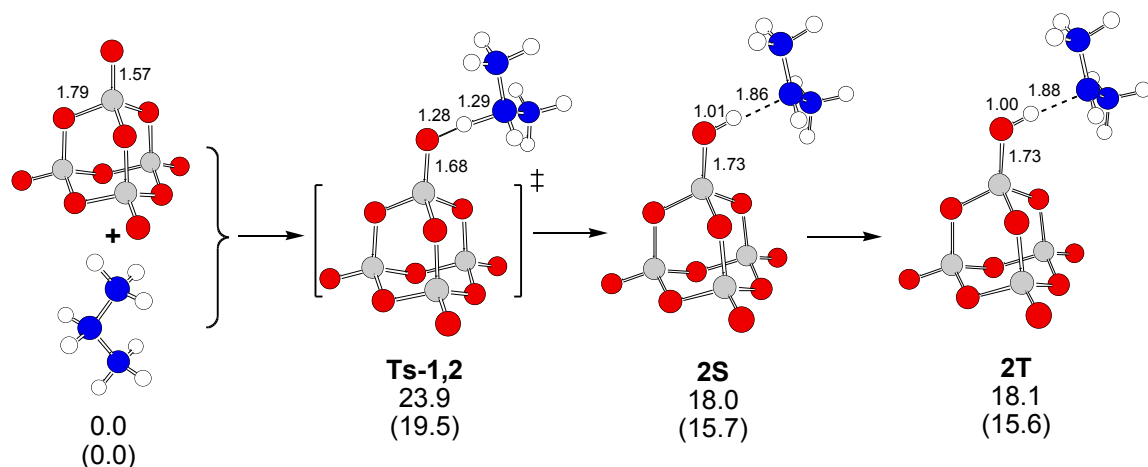


Figure 1.4 The first and second steps of propane ODH on V_4O_{10} (the first row of the energetic parameters is ΔE , while the second row is $\Delta H_{0K} = \Delta E + ZPE$). The near degeneracy of 2S and 2T demonstrates the diradical character of this state (one unpaired spin on the β -Carbon and one on the V).

In **Path 1** (**Figure 1.5**), the *iso*-propyl radical binds to the O(1)H group to form **3A**, which is 34.4 kcal/mol more stable than **2T**. **3A** is a triplet state lying 24.8 kcal/mol below the corresponding singlet state and can be considered a complex of *iso*-propanol and the triplet V_4O_9 cluster with two unpaired electrons located on the vanadium atom that bonds with *iso*-propanol. (The *iso*-propanol V_4O_9 fragment bond distance is 2.01 Å). In the final step in **Path 1**, O(2) abstracts the second hydrogen from the methyl group, leading to propene and **4A**, with an activation barrier of 31.2 kcal/mol.

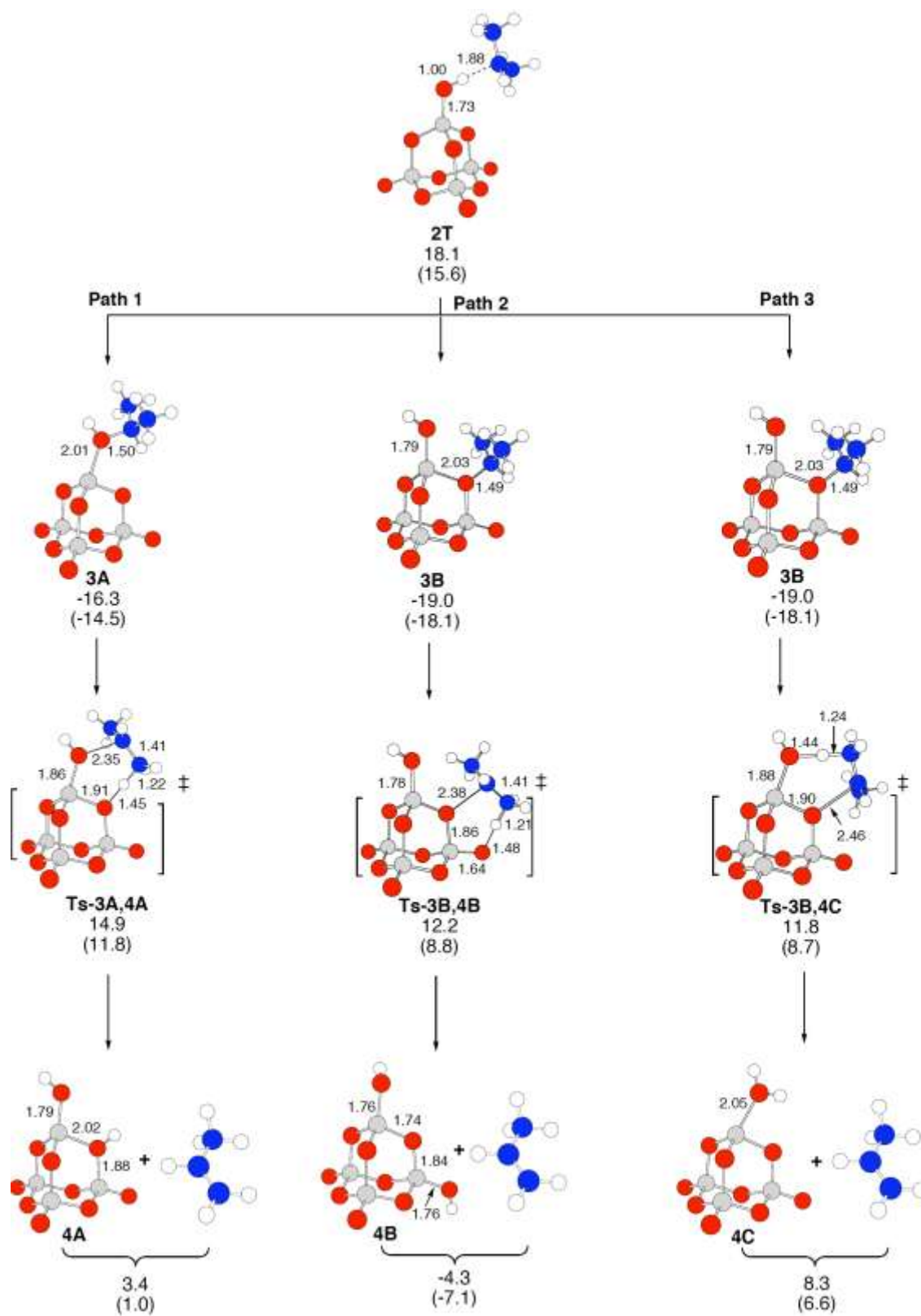


Figure 1.5 The three pathways for binding of *iso*-propyl radical (iPr) to the V_4O_{10} followed by the second hydrogen abstraction to release the propene product (the first row of the energetic parameters is ΔE , while the second row is $\Delta H_{0K} = \Delta E + ZPE$).

Path 2 and **3** start with the formation of the same intermediate (**3B**), through a bond formed between the *iso*-propyl radical and O(2). Similar to **3A**, **3B** is a triplet ground state lying 19.4 kcal/mol below the corresponding singlet state. Spin density analysis of **3B** shows that the two unpaired electrons are located on the same vanadium atom bonded to the hydroxyl group. In **Path 2**, O(1) abstracts an hydrogen from the methyl group with a 31.2 kcal/mol barrier (**Ts-3B,4B**) to form propene and **4B**.

Path 3 (hydroxyl-H^{2nd}-abs step), starting from the same intermediate, **3B**, uses the O(1)H group to abstract an hydrogen atom from the methyl group, leading to the formation of propene and **4C**, with a 30.8 kcal/mol barrier (**Ts-3B,4C**). We find that the spin distribution of **Ts-3B,4C** is the same as in **3B**. In the **Ts-3B,4C** structure, the bond distance of V-O(1)H increases from 1.79 Å in **3C** to 1.88 Å, while the V-O(2) bond distance decreases from 2.03 to 1.90 Å. For the product **4C**, spin density analysis shows that the two unpaired electrons are located on the same V atom bonded to the water fragment, which is similar to **3B** and **Ts-3B,4C**. Therefore, **4C** can be considered a complex of water and triplet V_4O_9 , with a 2.05 Å bond distance between the two fragments.

Path 3 has the lowest reaction barrier among the three possible reaction pathways studied in this work, 30.8 kcal/mol. The similar activation energies of the **Path 2** and

Path 3 implies that O(1) and O(1)H have very similar electrophilic characteristics, which contradicts the prediction by Chen^{9,10} that a new O(1) is needed to abstract the second hydrogen atom. We will use this lowest energy pathway, **Path 3**, in the next section to study the catalytic cycle for propane ODH.

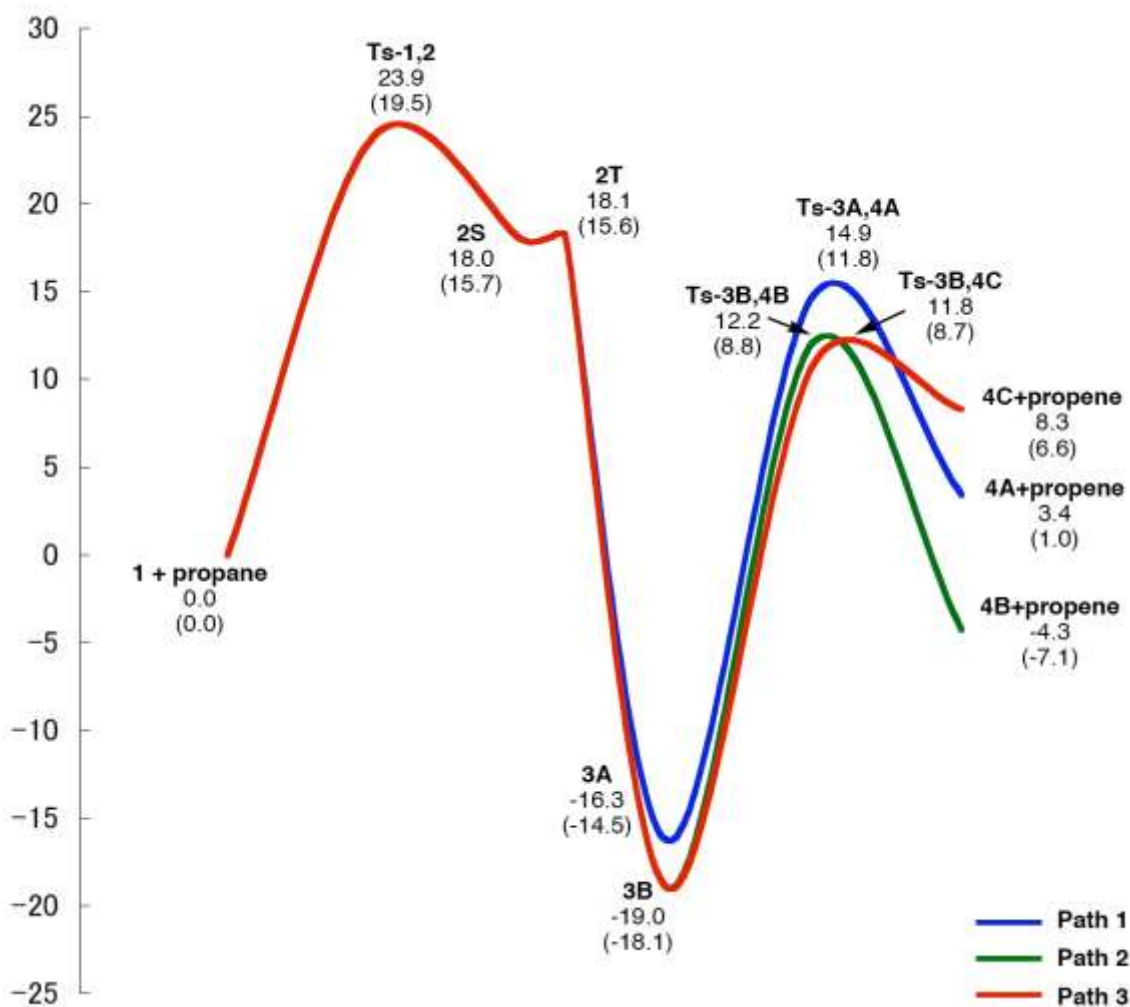


Figure 1.6 Energy profiles for propane ODH on V_4O_{10} (the first row of the energetic parameters is ΔE , while the second row is $\Delta H_{0K} = \Delta E + ZPE$)

Vanadium Reoxidation The optimized structures of the intermediates and products on the reaction pathways discussed below are summarized in **Figure 1.7**. The most favorable steps lead to **4C**, which we now consider as the starting point for the final part of the mechanism, dissociation of product and catalyst reoxidation. Recall that **4C** is a triplet state with the H₂O is bound through the lone pair of O. Considering the VOH₂ plane as yz with the z axis pointing along the axis of the V₄O₉ cluster, the V-OH₂ bond distance is 2.05 Å (a donor-acceptor bond), with an angle of 30.1° from the z axis. Thus, the O lone pair is coordinated with the empty d_{yz} orbital of the V. This leaves the d_{z^2} and d_{xz} orbitals singly occupied and triplet paired.

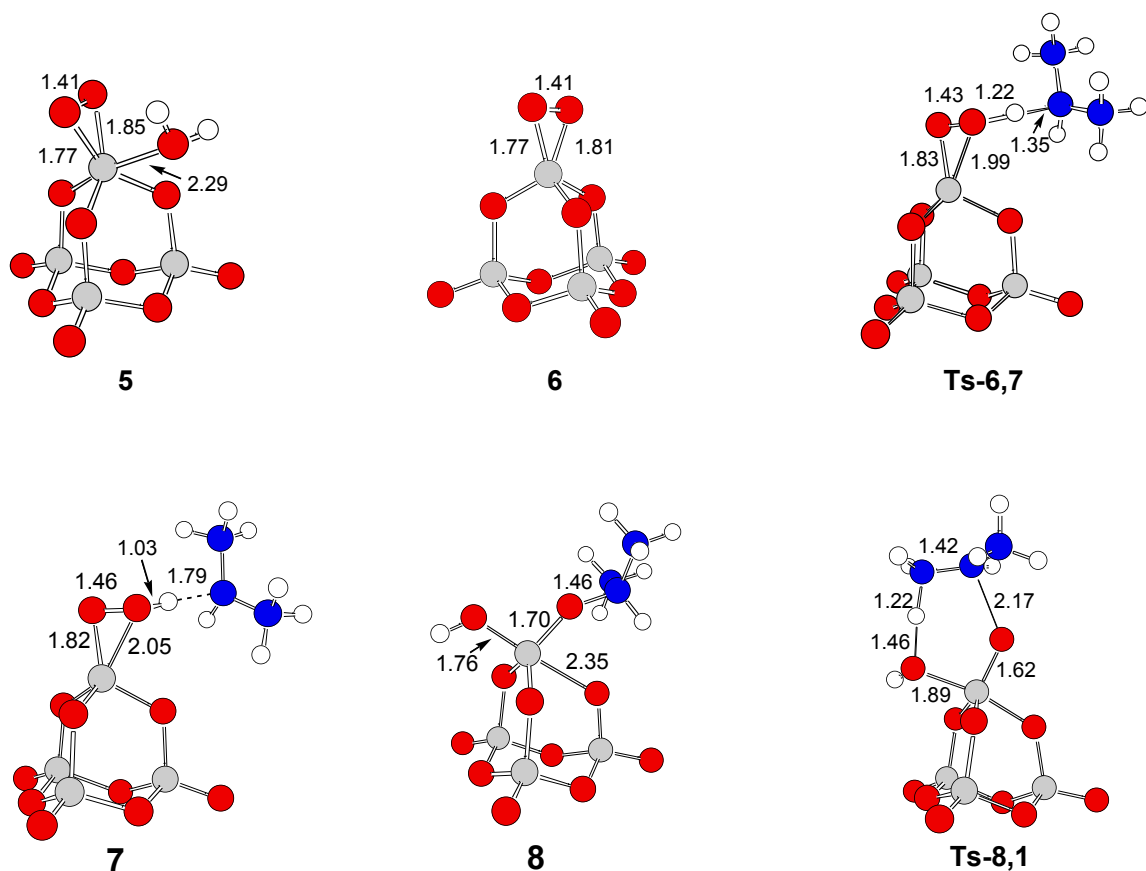


Figure 1.7 Structural parameters for the intermediates and transition states of the vanadium reoxidation step

Dissociation of the H₂O from 4C is not favorable It might be expected that water would easily dissociate from **4C** (an H₂O-V₄O₉ complex with a V^{III}) to create a vacant V^{III} site. However, we calculate a dissociation energy of 37.8 kcal/mol, which is significantly higher than the activation barriers for the conversion of propane to propene. Instead, we explored associative mechanisms where water dissociation is assisted by the oxidant, O₂.

Bonding of O₂ to 4C The bond energy of ³O₂ to **4C** to form **5**, a complex of V₄O₁₁ and water is 12.2 kcal/mol. Since both O₂ and **4C** are triplet states, we can form 2 singlets, 3 triplets, and 1 quintet state. We find that the ground state is the singlet, with the triplet state just 0.1 kcal/mol higher and the quintet state 7.7 kcal/mol higher.

Forming new bonds between such triplet states leads to the loss of half the exchange stabilization of the isolated triples, which might be expected to lead to a small barrier. However, the spin couplings can change continuously from that of the separated entities (the GF coupling^{48,49}) to that of the molecule (the G1 coupling^{48,49}), so that there is no net barrier (as shown by Voter and Goddard⁵⁰ for ³CH₂ + ³CH₂ to form ethene).

Indeed, we could find no barrier for the bonding of dioxygen to **4C**. All attempts at scanning the distance between **4C** and O₂ showed a monotonous decrease in energy, eventually resulting in the stable complex **5**, which can be considered as a complex of V₄O₁₁ (**6**) and water.

As will be described more completely in our discussion of **6** below, the VOO forms a

cyclic peroxide. Taking the VOO plane as xz , this involves rehybridizing the d_{z^2} and d_{xz} orbitals on the V to obtain orbitals that can spin pair directly with the O p_z orbitals on each O to form VO bonds, reducing the OO bond order to 1. Here the OH₂ lone pair continues to coordinate with the empty d_{yz} orbital of the V, although the V-H₂O bond distance in **5** is 2.29 Å, which is 0.24 Å longer than in **4C**, indicating a dramatically weakened bond.

Desorption of H₂O from 5 to form 6 Binding O₂ to **4C** has the effect of destabilizing the bonding of H₂O. Thus, the energy to desorb H₂O from **5** is only 12.9 kcal/mol (rather than the 37.8 kcal/mol from **4C**). Dissociating water from **5** produces the V₄O₁₁ cluster **6**, which can be thought of as the result of binding triplet dioxygen (³O₂) to the triplet state of the V₄O₉ cluster formed from V₄O₁₀ by removing a single O(1) atom. This combination of two triplet states leads to two singlets, three triplets, and one quintet state. Considering the axis of the V=O(1) bond of the original V₄O₁₀ cluster as the z axis, this V=O(1) bond can be thought of as a σ bond of V d_{z^2} to O p_z and a σ bond of V d_{xz} to the singly occupied O p_x (double bond in the xz plane) with the remaining doubly occupied O p_y orbital overlapping the empty V d_{yz} . Then there is resonance between this state with the bond in the xz plane and the equivalent state with the bond in the yz plane. Thus the triplet V₄O₉ cluster can be considered as having singly occupied V d_{z^2} and V d_{xz} (or singly occupied V d_{z^2} and V d_{yz}) available for binding.

We find that the ground state of **6** has the O₂ bonded sideways (VO₂ ring) to form a cyclic peroxide with V-O bond distances of 1.77 and 1.81 Å and an O-O bond distance of 1.41 Å, as shown in **Figure 1.8**. This suggests a single covalent O-O bond and a single

covalent bond between V and each O. Considering the VO_2 plane as xz , one can think of the bond as formed from hybrids of V d_{z^2} and V d_{xz} bonded to the p_z singly occupied orbitals from each of the two O atoms. This leads to a net bond energy for O_2 to the V_4O_9 cluster in **6** of 37.1 kcal/mol (dissociating to $^3\text{O}_2$ and the triplet state of V_4O_9).

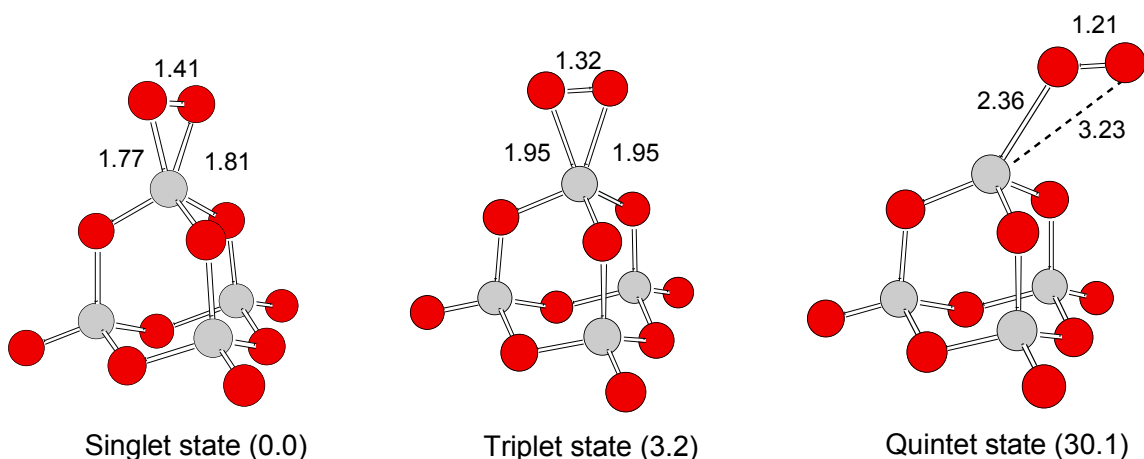


Figure 1.8 The structure parameters and relative energy for the lowest singlet, triplet, and quintet states of **6**. The bond energies relative to free $^3\text{O}_2$ are 37.1, 33.9, and 7.0, respectively.

The triplet state of **6** is only 3.2 kcal/mol higher in energy than the singlet. The 1.32 Å bond length of the triplet indicates a bond order of 3/2, the same as in the HO_2 radical (bond distance = 1.33 Å). Indeed, we find that one of the two unpaired electrons is in an $\text{OO } \pi^*$ antibonding orbital (xz and yz nodal planes, leading to xy overall symmetry) distributed evenly between the oxygen atoms in the peroxo group, thus forming a 3-electron/2-center O-O bond. The other unpaired spin of the triplet state is in the VO_2 plane, but in a V d_{xy} -like orbital. The bonding interaction between the O-O fragment and

V can be thought of as a spin pairing of the $O_2 \pi^*$ orbital in the xz plane with the V d_{xz} orbital. This leads to three electrons in the xz plane between the V and O_2 , suggesting a net bond order of 1.5. Indeed, the VO bonds of the triplet state are 0.18 and 0.14 Å longer than those of the singlet state, about what one would expect of bonds have 3/4 bond order. The bond is to the $O_2 \pi^*$ orbital. Since the fragments of **6** (O_2 and V_4O_9) both have triplet ground states, we also investigated the quintet state of **6**. However, as this state cannot form bonds between any of the 4 singly occupied orbitals, the quintet state of **6** is 30.1 kcal/mol higher in energy than the singlet state, with a calculated V- O_2 bond energy of 7.0 kcal/mol. This state leads to an OO bond distance of 1.21 Å, (same as we calculate for a free 3O_2) and V-O bond distances of 2.36 and 3.23 Å. Here the two unpaired spins on the V are d_{xz} and d_{z^2} . Thus one can think of the quintet state as a weakly bound van der Waals complex, with perhaps an electrostatic component due to the quadrupole moment on the O_2 .

Recently, a V-peroxo moiety was observed experimentally at low temperature (90 K) in the reaction of gaseous O_2 with $V_2O_3(0001)$ surface, a product of deep reduction of V_2O_5 .⁵¹ The vibrational frequency observed in the IRAS spectra was 951 cm^{-1} (indicative of a peroxo species). As the temperature was increased, this species disappeared below 225 K and was replaced by a normal V=O(1) frequency at 1040 cm^{-1} . We calculate 1042 cm^{-1} for the O-O stretching mode in singlet **6** and 1122 to 1142 for the three V=O(1) modes. [Our calculated vibrational frequency for the O-O stretching mode in the triplet state is 1233 cm^{-1} and for the quintet state is 1644 cm^{-1} (we calculate 1662 cm^{-1} for the free O_2)] Our V_4O_{10} cluster puts the peroxo vibration at 90 cm^{-1} below the V=O(1)

stretch, which is in good agreement with the experimental observation on reduced V_2O_3 (89 cm^{-1} shift). Consequently, we agree with the assignment by ref 51 of the 951 cm^{-1} species as a peroxo bound species, $V-(O_2^{2-})$. The observation of such an OO species in IRAS has been attributed to the change in the V-O distance as the OO bond is modified.⁵¹

Conversion of 6 to reform the initial catalyst, V_4O_{10} To complete the catalytic cycle, the peroxy species **6** must be converted back to the initial V_4O_{10} complex. We expected that **6**, with its nearly degenerate singlet and triplet states, would be more reactive than the initial model catalyst, $V_4O_{10}(1)$. However, bonding an H atom to **6** to form a bound V-OOH gains 80.3 kcal/mol , compared to 78.0 kcal/mol for bonding H to the $V=O(1)$ of $V_4O_{10}(1)$, indicating similar reactivity. Even so, this is much weaker than the OH bond of H_2O (calculated to be 119.9 kcal/mol) and consequently we would not expect to find reactions such as sequential hydrogen transfers from water, [$6 + H_2O \rightarrow V_4O_9(OOH)(OH) \rightarrow V_4O_{10} + HOOH$]. Indeed, experimental studies found no traces of hydrogen peroxide even as a transient intermediate.

Instead, we hypothesized that **6** might instead activate a second propane. We find a very facile mechanism for hydrogen abstraction using the peroxo moiety (**peroxo-H^{1st}-abs step**), with a calculated barrier of 16.5 kcal/mol , 7.4 kcal/mol lower than the barrier for the initial hydrogen abstraction step (**Ts-1,2**) using the V_4O_{10} catalyst. [Because the transition state (**Ts-6,7**) and product (**7**) of this new hydrogen abstraction step have diradical character, the broken symmetry approach was used to calculate the open-shell singlet states.]

In the subsequent step, the *iso*-propyl radical fragment in **7** bonds with the other

oxygen atom of the peroxo group to form **8** without a barrier. The second molecule of propene and water are formed by passing through a six-membered ring transition state, **Ts-8,1**. For this step, the activation energy is 30.0 kcal/mol and the reaction energy is 29.1 kcal/mol (**peroxo-H^{2nd}-abs step**). At 298.15 K, the Gibbs free energy barrier reduces to 24.2 kcal/mol. The initial V₄O₁₀ catalyst is regenerated, completing the catalytic cycle.

The Catalytic Cycle for Single-Site Vanadyl Activation, Functionalization, and Reoxidation mechanism (SS-VAFR) Combining the lowest energy steps from the previous sections, we can now determine the complete catalytic cycle, summarized schematically in **Figure 1.9**. The potential energy surface for this cycle is shown in **Figure 1.10**. The overall reaction is



The four reaction barriers (kcal/mol) in this catalytic cycle are

$$\Delta E = 23.9 \text{ kcal/mol, } \Delta G_{298.15} = 29.6 \text{ kcal/mol (vanadyl-H}^{1\text{st}}\text{-abs step)}$$

$$\Delta E = 30.8 \text{ kcal/mol, } \Delta G_{298.15} = 26.9 \text{ kcal/mol (hydroxyl-H}^{2\text{nd}}\text{-abs step)}$$

$$\Delta E = 16.5 \text{ kcal/mol, } \Delta G_{298.15} = 22.2 \text{ kcal/mol (peroxo-H}^{1\text{st}}\text{-abs step)}$$

$$\Delta E = 30.0 \text{ kcal/mol, } \Delta G_{298.15} = 24.2 \text{ kcal/mol (peroxo-H}^{2\text{nd}}\text{-abs step)}$$

Thus, although the highest barrier on the ΔE surface is 30.8 kcal/mol for **hydroxyl-H^{2nd}-abs**, the free energy barrier at 298.15 K (rate-determining) is activating the methylene C-H bond of propane (**vanadyl-H^{1st}-abs step**). This is consistent with experiments.^{12,13,19}

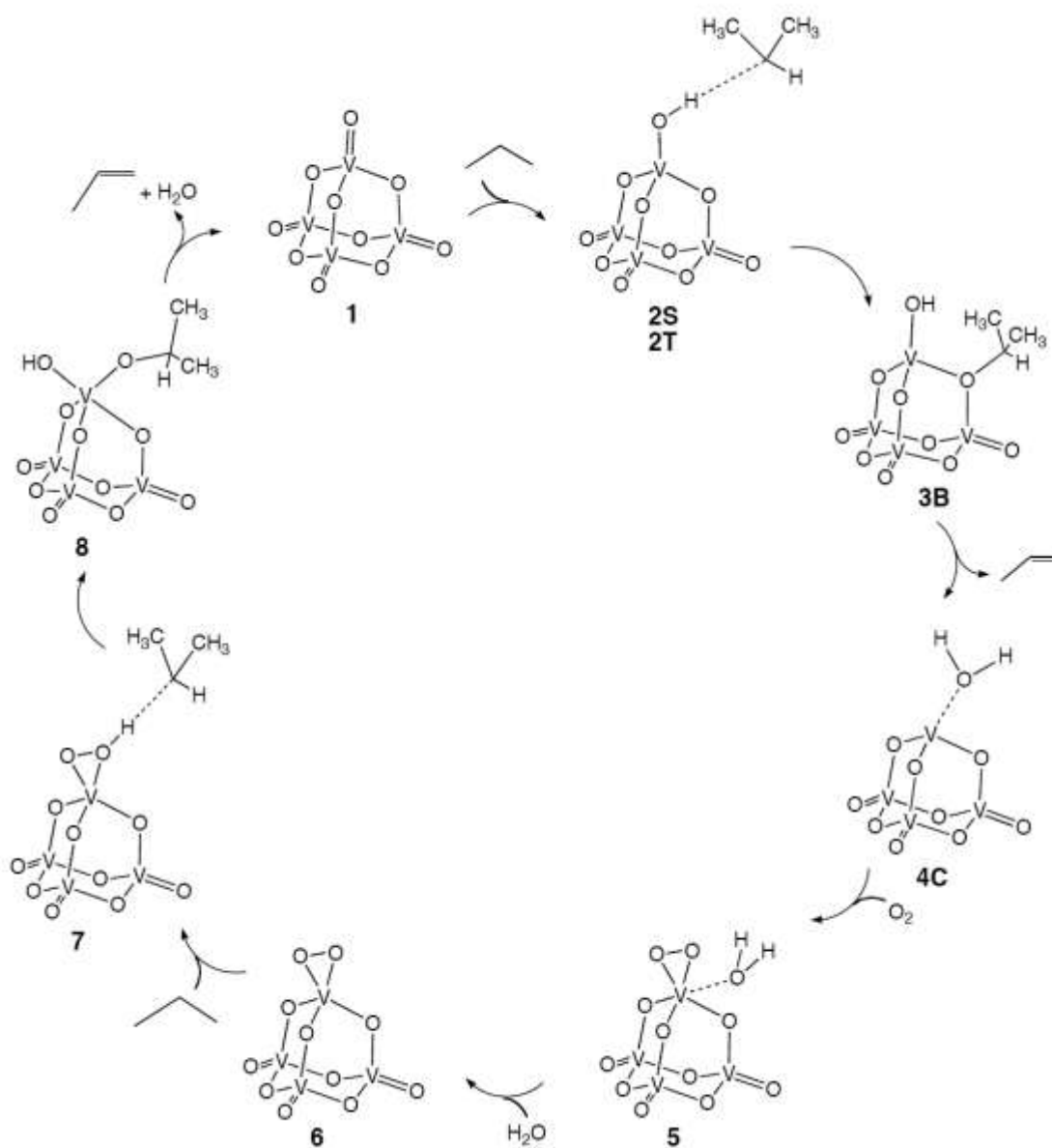


Figure 1.9 The catalytic cycle for propane ODH on V₄O₁₀ derived from the QM calculations. The energies are in **Figure 1.10**. We refer to this as the *single-site vanadyl activation, functionalization, and reoxidation* mechanism. (SS-VAFR).

In our catalytic cycle, the V=O(1) is the active site for all steps with O(2) only playing

the role of stabilizing the *iso*-propyl radical by forming the stable intermediate **3C**.

Thus we refer to this as the Single-Site Vanadyl Activation, Functionalization, and Re-oxidation (SS-VAFR) mechanism. The SS-VAFR mechanism is appropriate for describing the propane ODH reaction on supported vanadium oxide catalysts where it is expected that only isolated monovanadates species are present with are no adjacent V-O(2)-V or V=O(1) groups. Particularly interesting is that this novel mechanism accounts for reoxidation of the reduced vanadium center with simultaneous dissociation of water to generates a V-peroxo moiety with higher reactivity than the original V=O(1).

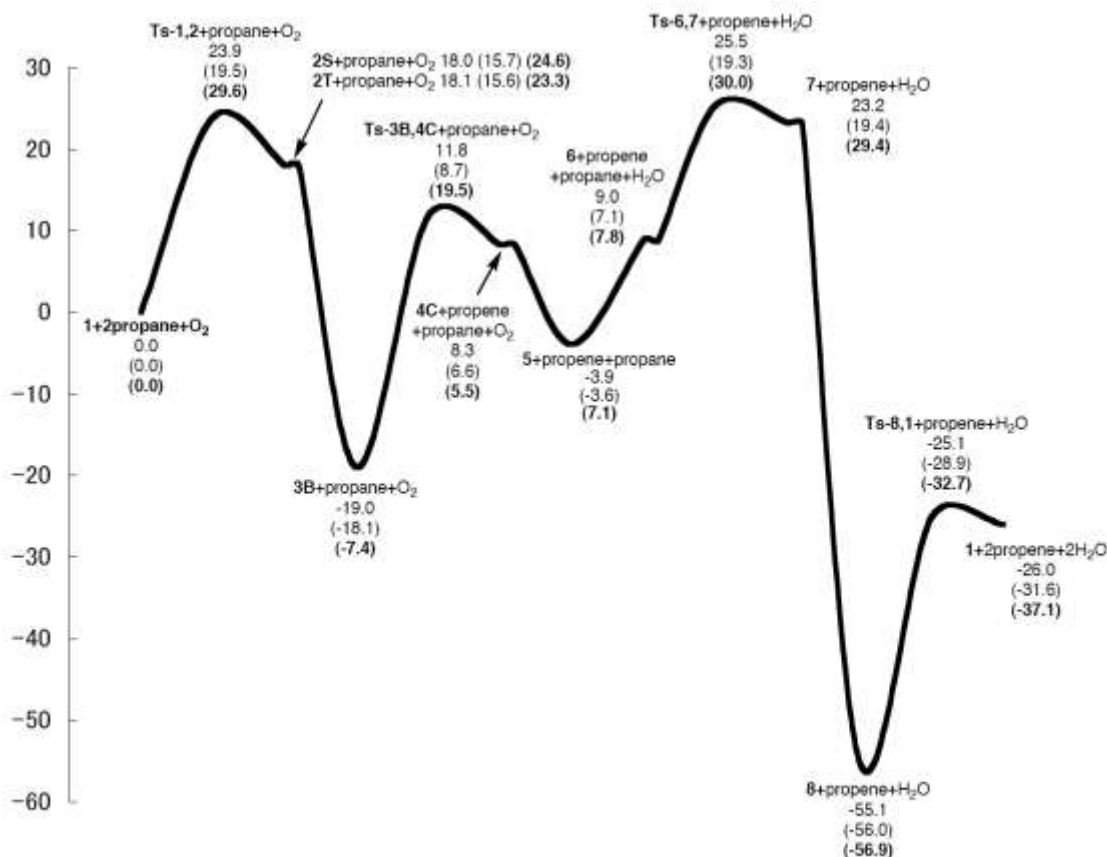


Figure 1.10 Energy profiles of the SS-VAFR catalytic cycle for propane ODH on V_4O_{10} (the first row of the energetic parameters is ΔE , the second row is $\Delta H_{0K} = \Delta E + ZPE$, and the third row is $\Delta G(298.15\text{ K})$).

1.4 Discussion

Previous theoretical investigations of $V_2O_5(001)$ surface by Hermann *et al.*⁵² suggested that the water dissociation energy could be decreased by forming bonds between the reduced V atom and the V=O(1) group of the second layer. However, the supported vanadium oxide catalysts have vanadia concentrations of less than the one monolayer limit, with structures that do not have the layered structure suggested would facilitate water dissociation. Our current calculations do not allow us to directly compare the two possible pathways, but instead we provide an alternative way to reoxidize the reduced vanadium center and remove water from the surface simultaneously without the need to postulate assistance of bonding between layers in $V_2O_5(001)$.

Energetics of H-O bond formation Hermann *et al.*⁵² studied binding energies of hydrogen on V_2O_5 using the Zhang-Yang modification (rev-PBE)⁵³ of the PBE DFT to calculate single point energies on Vosko–Wilk–Nusair functional optimized structures. The authors calculated the binding energy of hydrogen atoms to the three different types of oxygen atoms on a one layer $V_2O_5(001)$ cluster model containing five formula units terminated by hydroxyl groups, and concluded that the bond strength is 54.0 kcal/mol to O(1), 51.0 kcal/mol with O(2), and 43.4 kcal/mol with O(3).

Yin *et al.*⁵⁴ performed periodic BLYP calculations on a one-layer periodic $V_2O_5(001)$

slab. The authors also found a similar trend in bond strengths of the hydrogen atom to the different oxygen types: 62.2 kcal/mol with O(1), 60.3 kcal/mol with O(2), and 59.3 kcal/mol with O(3). However, the difference between the O(1)-H and O(3)-H bond strengths is calculated to 2.9 kcal/mol, rather than 10.6 kcal/mol, as calculated by Hermann *et al.*⁵²

Fu *et al.*²² also performed periodic QM calculations, using the GGA-PW91 flavor of DFT, on a one-layer periodic $V_2O_5(001)$ slab to determine the strength of the H-O bond. They found a trend consistent with Yin⁵⁴ and Hermann⁵² and calculated the energy of adsorption of the H atom on O(1) = 66.3 kcal/mol, on O(2) = 61.2 kcal/mol, and on O(3) = 58.0 kcal/mol. [Their reported numbers were O(1) = 12.7 kcal/mol, on O(2) = 7.6 kcal/mol, and on O(3) = 4.4 kcal/mol relative to $1/2H_2$. We converted this to values relative to H atom using the PW91 bond energy for H_2 of 107.1 kcal/mol.] Thus, here the difference between the O(1)-H and O(3)-H bond strengths is 8.3 kcal/mol, in between the values from Yin⁵⁴ and Hermann.⁵²

Our HO bond energies are 78.0 for O(1) and 69.5 kcal/mol for O(2). Our calculations in this paper are all based on the B3LYP flavor of DFT, which gives the most accurate cohesive energies among the various DFT methods (average error in cohesive energy of 3.1 kcal/mol versus 17.1 kcal/mol for PBE and 7.9 kcal/mol for PW91).^{55,56}

To test this, we used PBE to find HO bond energies of 68.6 kcal/mol for O(1) and 61.4 kcal/mol for O(2), which compares to the Hermann's values of 54.0 kcal/mol for O(1) and 51.0 kcal/mol for O(2) using rev-PBE. This difference may be a peculiarity of rev-PBE or of their cluster model.

For PW91 we find HO bond energies of 71.3 kcal/mol for O(1) and 63.9 kcal/mol for O(2). This compares to the Fu values of H-O(1) = 66.3 kcal/mol and H-O(2) = 61.2 kcal/mol. This difference may be a difference between their single periodic layer model and our cluster model.

All calculations agree that it is easier to bond the H to V=O(1) than to V-O(2)-V, as expected from having a weaker V=O π bond. The differences are 8.5 kcal/mol in our work, 3.0 for Hermann⁵² and 1.9 for Yin.⁵⁴

Energetics of O removal Sauer *et al.*^{42,57} calculated the energy for formation of an oxygen vacancy using both a two-layer cluster (10 formula units terminated with hydroxyl groups) and a two-layer periodic slab (12 formula units per cell). The authors used the PW91 flavor of DFT for periodic calculations⁴² and BP86, B3LYP, and PBE flavors of DFT for cluster calculations.⁵⁷ The V=O bond dissociation energy in VO₂⁺ calculated using hybrid DFT (B3LYP) provided the best results and was within 4 kcal/mol of experiment, while gradient corrected but nonhybrid functionals (BP86 and PBE) yielded large errors of 18 to 37 kcal/mol. The authors concluded from the periodic slab calculations that the energy to remove O(1) is 45.0 kcal/mol, O(2) is 84.9 kcal/mol and O(3) is 90.9 kcal/mol.⁴² In contrast, the authors found that the finite cluster leads to an oxygen vacancy energy of 27 kcal/mol for removal of O(1).⁵⁷ The authors attributed the ease of removing oxygens from the two-layer slab to the formation of V-O-V bonds between the crystal layers.

Hermann *et al.*⁵² calculated the energy to form an oxygen vacancy using a one-layer model consisting of five V₂O₅ formula units terminated by hydrogen atoms. Using rev-

PBE they found that the energy to remove O(1) is 149.2 kcal/mol, O(2) is 165.8 kcal/mol, and O(3) is 149.7 kcal/mol.

We also calculated the energy for formation of an oxygen vacancy in the V_4O_{10} cluster and found that energy to remove O(1) is 121.9 kcal/mol and O(2) is 140.2 kcal/mol using the B3LYP level. The difference between this and the results of Sauer *et al.* (also B3LYP) is most likely due to the 2nd layer that they include.

To compare with Hermann we also carried out PBE calculations obtaining values of 145.8 kcal/mol for O(1) and 173.2 kcal/mol for O(2), in rough agreement with Hermann. This suggests that the difference between our results and the Hermann results are due to our using a more accurate level of DFT. Nevertheless, while the two-layer periodic slab has significantly smaller values, the qualitative trend in the oxygen vacancy energy is consistent for the different V_2O_5 systems.

Removal of an OH bond Hermann *et al.*⁵² found that the energy to remove a hydroxyl group, formed by adding a hydrogen atom to the O(1), O(2), and O(3) of a one-layer model (consisting of five formula units terminated with hydrogen atoms), was 91.8 kcal/mol, 105.4 kcal/mol, and 81.6 kcal/mol, respectively.

The one-layer periodic calculations of Yin *et al.*⁵⁴ also reveal the same trend in binding energies of the hydroxyl group, with 94.5 kcal/mol for removal of O(1)H, 109.0 kcal/mol for removal of O(2)H, and 88.0 for removal of O(3)H.

We find that the strength of the V-OH bond using the V_4O_{10} model is 94.3 kcal/mol for O(1)H and 104.1 kcal/mol for O(2)H which is consistent with both the Hermann⁵² and

Yin⁵⁴ results.

Removal of a surface H₂O Hermann *et al.*⁵² calculated the energy to remove water formed at an O(1) to be 11.1 kcal/mol, at an O(2) 3.7 kcal/mol and at an O(3) -10.1 kcal/mol. Therefore, the energy for oxygen removal is reduced by as much as 40% via dissociation of a hydroxyl group and 90% through dissociation of water when compared to removal of an oxygen atom.

We also calculated the strength of the V-OH₂ bond using the V₄O₁₀ cluster and found the strength of the V-O(1)H₂ bond to be 37.8 kcal/mol and the strength of the V-O(2)H₂ to be 5.4 kcal/mol. While our binding energy of O(1)H₂ is very different from Hermann's,⁵² it is not clear where this discrepancy comes from. Single point PBE calculations on our geometries show that it is not depending on the functional used (34.5 kcal/mol), while control calculations on a smaller system (Cl₃V-OH₂) shows a similar gap. Moreover, all our calculated clusters are C₁ symmetric, and we have ensured that all lowest energy orbital populations have been used. However, it should be noted that the singlet-triplet gaps for the species V₄O₉-H₂O and V₄O₉ are 22.3 and 15.0 kcal/mol, respectively, and it is thus possible that if Hermann *et al.*⁵² used the singlet state for the water complex, the overall binding energy would be significantly less. In our case, we calculate that V₄O₉-H₂O (singlet state) → V₄O₉ (triplet state) + H₂O is uphill by 15.5 kcal/mol. Moreover, from Fu's two layers periodic calculations,²² the V-H₂O binding energy is 13.0 kcal/mol with the assistance of an extra V-O-V bond between the two layers. It is reasonable to assume that the V-H₂O binding energy will increase, if only one layer periodic model is used. Although there is discrepancy between our and

Hermann's results, both calculations agree that the presence of hydrogen on the $V_2O_5(001)$ surface facilitates removal of H_2O from the surface.

Reaction Mechanism Several recent theoretical papers have provided new insight into the alkane ODH mechanism.^{20,21,22} Gilardoni *et al.*²⁰ used DFT (BPW91 and Becke 1998) to investigate the propane ODH reaction mechanism on finite clusters. They found that the initial step is a barrierless O(1) insertion into the C-H bond of the propane methylene group. They also found that the highest barrier for conversion of propane to propene (15 kcal/mol) arises from hydrogen migration from the methyl group in absorbed *iso*-propyl to protonated O(3) to form water. Redfern *et al.*²¹ re-examined this mechanism using a different V_2O_5 model, and found a 79.4 kcal/mol barrier for the O(1) insertion into the C-H bond and an overall barrier of 80.5 kcal/mol for the reaction pathway. For this reason, Redfern *et al.*²¹ concluded that the $V_2O_5(001)$ surface is unfavorable for propane ODH, contradicting Gilardoni's²⁰ results.

However, several potential mechanistic pathways were left unexplored in the previous studies, particularly the direct hydrogen abstraction leading to a propyl radical. Our studies find that this mechanism is quite feasible on a finite cluster model. We find that the energetically most favorable activation of propane occurs through hydrogen abstraction of the methylene hydrogen by a vanadyl group with a barrier of 23.9 kcal/mol. We find that the highest ΔE barrier for the overall mechanism is 30.8 kcal/mol, corresponding to extraction of the 2nd H from the CH_3 of *iso*-propyl bonding to O(2) by the OH bonded to the original O(1) site that activated the propane.

While this manuscript was in preparation, a paper by Fu *et al.*²² appeared that also

considered ODH, but using periodic DFT calculations (PBE rather than B3LYP) on a periodic slab with one layer of $V_2O_5(001)$. They found that the vanadyl-H^{1st}-abs step is most favorable with a ΔE barrier of 27.3 kcal/mol, in agreement with our conclusion and with a quantitative result quite similar to our value of 23.9 kcal/mol. Thus, both our results and those of Fu et al.²² contradict the conclusions from Gilardoni *et al.*²⁰ and Redfern *et al.*²⁷ that activation occurs by O(1) insertion into the C-H bond of propane.

Fu *et al.* also proposed an alternative C-H activation pathway of O(2) insertion into the methylene C-H bond propane, reporting a ΔE barrier of 30.4 kcal/mol. We did not consider this pathway for propane ODH on the V_4O_{10} model, as we assumed that such a direct insertion would have a prohibitively high barrier.

Fu *et al.*²² described two mechanisms for abstraction of the second hydrogen from one of the methyl groups of the chemisorbed *iso*-propyl. Mechanism Fu-1 uses an second O(1) to abstract hydrogen from an *iso*-propyl group bonded to a second O(1) with a calculated ΔE barrier of 30.9 kcal/mol. Mechanism Fu-2 uses an O(3) to abstract a hydrogen from an *iso*-propyl group bonded to O(2) with a barrier of $\Delta E = 33.7$ kcal/mol. Fu did not consider the process that we find most favorable (30.8 kcal/mol barrier), namely extraction of the 2nd H from the CH_3 of *iso*-propyl bonding to O(2) by the OH bonded to the original O(1) site that activated the propane. We did not consider the Fu mechanisms because they do not seem plausible for the V_4O_{10} cluster geometry. For mechanism Fu-1, the distance between two O(1) atoms in the V_4O_{10} model is 5.62 Å, much longer than that of 3.56 Å in $V_2O_5(001)$ surface. Moreover, the two V=O(1) groups are not parallel in V_4O_{10} model, and we do not believe that a mechanism using this geometry would be realistic. Mechanism Fu-2 involves O(3) which does not exist in

our V_4O_{10} cluster model.

Nevertheless, the most favorable ΔE barrier for abstracting the 2nd barrier using a second O(1) that Fu *et al.* calculate (30.9 kcal/mol) is quite similar to our most favorable ΔE barrier (30.8 kcal/mol) using the O(1)H.

We consider that our mechanism is probably relevant for supported V_2O_5 catalysts where the O(1) sites are likely isolated. For bulk V_2O_5 catalysts, Sauer^{42,57} has shown that there are major effects due to the 2nd layer of V_2O_5 and hence the Fu mechanisms (based on a single layer) might not be relevant here.

1.5 Conclusions

We conclude from the consistency of these studies with experimental mechanistic results that the cubic V_4O_{10} cluster is a valid model for studying the catalysis on V_2O_5 , particularly for supported catalysts which have only separated monovanadate (VO_4) species. The advantage over other cluster models is that there are no broken bonds to O and no OH groups, each of which can affect the energies and mechanism. However, we have not shown that this model describes the chemistry of the bulk catalyst where effects involving the second layer could play a role.

We report here the complete catalytic cycle for conversion of propane to propene on a V_4O_{10} cluster *including reoxidation of the active site*. This is the Single-Site Vanadyl Activation, Functionalization, and Reoxidation mechanism (SS-VAFR).

At 298.15 K, we find that the rate determining step (highest barrier of 29.6 kcal/mol)

corresponds to the first hydrogen abstraction from the methylene group of propane by the terminal oxygen (V=O(1)). This is consistent with experimental results.^{12,13,19} Particularly remarkable about our catalytic cycle is that gaseous $^3\text{O}_2$ promotes water desorption while simultaneously reoxidizing the reduced vanadium oxide catalyst. Without this promotion by $^3\text{O}_2$, the barrier for water dissociation would increase significantly from 12.9 kcal/mol to 37.8 kcal/mol! Indeed, the resulting peroxo- V_4O_9 cluster (**6**) has been observed experimentally.⁵¹ We predict that **6** activates the methylene C-H bond in propane with a reaction barrier 7.4 kcal/mol lower than for the V_4O_{10} cluster. Experiments on this now isolated system would provide an interesting test of our predictions.

Since the C-H bond of propene product is ~ 7 kcal/mol *weaker* than the H-*i*Pr bond in propane, the V=O(1) sites could react more quickly with product than reactant, likely leading to products such as CO_2 . To avoid such a loss in selectivity it may be important that the product not be exposed to V=O sites. This may be why the supported catalysts have high selectivity. In the SS-VAFR catalytic cycle, the V=O(1) sites play the essential role for all reaction steps while bridging oxygens (V-O(2)-V) play the role stabilizing the *iso*-propyl intermediate. This mechanism should be most suitable for understanding the propane ODH reaction on supported vanadium oxide catalysts, where only monovanadates species are expected to be present.

1.6 References

1. Le Bars, J.; Vadrine, J. C.; Auroux, A.; Trautmann, S.; Baerns, M. *Appl. Catal., A* **1992**, 88, 179.
2. Blasco, T.; Nieto, J. M. L. *Appl. Catal., A* **1997**, 157, 117.
3. Surney, S.; Ramsey, M. G.; Netzer, F. P. *Prog. Surf. Sci.* **2003**, 73, 117.
4. Went, G. T.; Oyama, S. T.; Bell, A. T. *J. Phys. Chem.* **1990**, 94, 4240.
5. Oyama, S. T.; Somorjai, G. A. *J. Phys. Chem.* **1990**, 94, 5022.
6. Oyama, S. T.; Middlebrook, A. M.; Somorjai, G. A. *J. Phys. Chem.* **1990**, 94, 5029.
7. Oyama, S. T. *J. Catal.* **1991**, 128, 210.
8. Le Bars, J.; Vadrine, J. C.; Auroux, A.; Pommier, B.; Pajonk, G. M. *J. Phys. Chem.* **1992**, 96, 2217.
9. Kung, H. H. *Adv. Catal.* **1994**, 40, 1.
10. Busca, G. *Catal. Today* **1996**, 27, 457.
11. Khodakov, A.; Olthof, B.; Bell, A. T.; Iglesia, E. *J. Catal.* **1999**, 181, 205.
12. Chen, K. D.; Khodakov, A.; Yang, J.; Bell, A. T.; Iglesia, E. *J. Catal.* **1999**, 186, 325.
13. Chen, K. D.; Iglesia, E.; Bell, A. T. *J. Catal.* **2000**, 192, 197.
14. Argyle, M. D.; Chen, K. D.; Bell, A. T.; Iglesia, E. *J. Catal.* **2002**, 208, 139.
15. Argyle, M. D.; Chen, K. D.; Bell, A. T.; Iglesia, E. *J. Phys. Chem. B* **2002**, 106, 5421.
16. Pieck, C. L.; Banares, M. A.; Fierro, J. L. G. *J. Catal.* **2004**, 224, 1.
17. Mamedov, E. A.; Corberan, V. C. *Appl. Catal., A* **1995**, 127, 1.
18. Mars, P.; van Krevelen, D. W. *Chem. Eng. Sci., Special Suppl.* **1954**, 3, 41.

19. Chen, K. D.; Bell, A. T.; Iglesia, E. *J. Phys. Chem. B* **2000**, 104, 1292.
20. Gilardoni, F.; Bell, A. T.; Chakraborty, A.; Boulet, P. *J. Phys. Chem. B* **2000**, 104, 12250.
21. Redfern, P. C.; Zapol, P.; Sternberg, M.; Adiga, S. P.; Zygmunt, S. A.; Curtiss, L. *J. Phys. Chem. B* **2006**, 110, 8363.
22. Fu, H.; Liu, Z.-P.; Li, Z.-H.; Wang, W.-N.; Fan, K.-N. *J. Am. Chem. Soc.* **2006**, 128, 11114.
23. Becke, A. D. *J. Chem. Phys.* **1993**, 98, 5648.
24. Becke, A. D. *Phys. Rev. A* **1988**, 38, 3098.
25. Lee, C. T.; Yang, W. T.; Parr, R. G. *Phys. Rev. B* **1988**, 37, 785.
26. Baker, J.; Muir, M.; Andzelm, J.; Scheiner, A. In *Chemical Applications of Density Function Theory*; Laird, B. B.; Ross, R. B.; Ziegler, T.; Eds.; ACS Symposium Series 629; American Chemical Society: Washington, DC, 1996.
27. Niu, S. Q.; Hall, M. B. *Chem. Rev.* **2000**, 100, 353.
28. Oxgaard, J.; Periana, R. A.; Goddard, W. A., III. *J. Am. Chem. Soc.* **2004**, 126, 11658.
29. Benitez, D.; Goddard, W. A., III. *J. Am. Chem. Soc.* **2005**, 127, 12218.
30. Keith, J. M.; Nielsen, R. J.; Oxgaard, J.; Goddard, W. A., III. *J. Am. Chem. Soc.* **2005**, 127, 13172.
31. Jacob, T.; Goddard, W. A., III. *J. Phys. Chem. B* **2005**, 109, 297.
32. Keith, J. A.; Oxgaard, J.; Goddard, W. A., III. *J. Am. Chem. Soc.* **2006**, 128, 3132.
33. Ziatdinov, V. R.; Oxgaard, J.; Mironov, O. A.; Young, K. J. H.; Goddard, W. A., III.; Periana, R. A. *J. Am. Chem. Soc.* **2006**, 128, 7404.

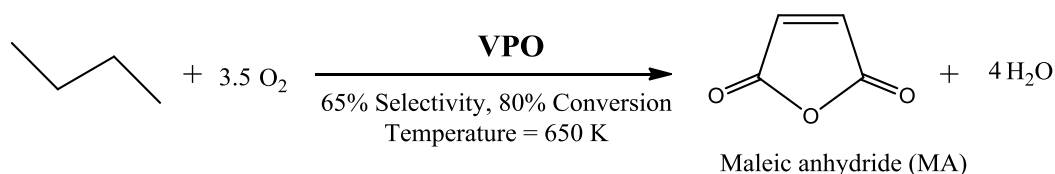
34. Nielsen, R. J.; Goddard, W.A., III. *J. Am. Chem. Soc.* **2006**, 128, 9651.
35. Oxgaard, J.; Bhalla, G.; Periana, R. A.; Goddard, W. A., III. *Organometallics* **2006**, 25, 1618.
36. Persson, P.; Lundqvist, M. J.; Ernstorfer, R.; Goddard, W. A., III.; Willig, F. J. *Chem. Theory Comput.* **2006**, 2, 441.
37. (a) Hay, P. J.; Wadt, W. R. *J. Chem. Phys.* **1985**, 82, 299. (b) Melius, C. F.; Goddard, W. A., III. *Phys. Rev. A* **1974**, 10, 1541. (c) Melius, C. F.; Olafson, B. O.; Goddard, W. A., III. *Chem. Phys. Lett.* **1974**, 28, 457.
38. Harihara, P. C.; Pople, J. A. *Chem. Phys. Lett.* **1972**, 16, 217.
39. Francl, M. M.; Pietro, W. J.; Hehre, W. J.; Binkley, J. S.; Gordon, M. S.; Defrees, D. J.; Pople, J. A. *J. Chem. Phys.* **1982**, 77, 3654.
40. Jaguar 6.5; Schrodinger, LLC: Portland, OR, **2005**.
41. Enjalbert, R.; Galy, J. *Acta Crystallogr., Sect. C: Cryst. Struct. Commun.* **1986**, 42, 1467.
42. Ganduglia-Pirovano, M. V.; Sauer, J. *Phys. Rev. B* **2004**, 70, 045422.
43. Gilson, T. R.; Bizri, O. F.; Cheetham, N. *J. Chem. Soc., Dalton Trans.* **1973**, 291.
44. Oyama, S. T.; Went, G. T.; Lewis, K. B.; Bell, A. T.; Somorjai, G. A. *J. Phys. Chem. A* **1989**, 93, 6786.
45. Kenny, N.; Kanneur, C. R.; Whitmore, D. H. *J. Phys. Chem. Solids* **1966**, 27, 1237.
46. Bodo, Z.; Hevesi, I. *Phys. Status Solidi* **1967**, 20, K45.
47. Feyel, S.; Dobler, J.; Schroder, D.; Sauer, J.; Schwarz, H. *Angew. Chem., Int. Ed.* **2006**, 45, 4681.

48. Goddard, W. A., III. *Phys. Rev.* **1967**, 157, 73.
49. Goddard, W. A., III. *Phys. Rev.* **1967**, 157, 81.
50. Voter, A. F.; Goodgame, M. M.; and W. A. Goddard, W. A., III. *Chem. Phys.* **1985**, 98, 7.
51. Abu Haija, M.; Guimond, S.; Romanyshyn, Y.; Uhl, A.; Kuhlenbeck, H.; Todorova, T. K.; Ganduglia-Pirovano, M. V.; Dobler, J.; Sauer, J.; Freund, H. J. *Surf. Sci.* **2006**, 600, 1497.
52. Hermann, K.; Witko, M.; Druzinic, R.; Tokarz, R. *Appl. Phys., A* **2001**, 72, 429.
53. Zhang, Y.; Yang, W. *Phys. Rev. Lett.* **1998**, 80, 890.
54. Yin, X. L.; Han, H. M.; Endou, A.; Kubo, M.; Teraishi, K.; Chatterjee, A.; Miyamoto, A. *J. Phys. Chem. B* **1999**, 103, 1263.
55. Xu, X.; Goddard, W. A., III. *Proc. Nat. Acad. Sci.* **2004**, 101, 2673.
56. Xu, X.; Zhang, Q. S.; Muller, R. P.; Goddard, W. A., III. *J. Chem. Phys.* **2005**, 122, 014105.
57. Sauer, J.; Dobler, J. *J. Dalton Trans.* **2004**, 3116.

**THE MAGNETIC AND ELECTRONIC STRUCTURE OF VANADYL
PYROPHOSPHATE FROM DENSITY FUNCTIONAL THEORY**

2.1 Introduction

A most fascinating and unique catalyst system is vanadium phosphorus oxide (VPO), which selectively catalyzes the partial oxidation of *n*-butane (C₄H₁₀) to maleic anhydride (MA, C₄O₃H₂) (Scheme 2.1).



Scheme 2.1

This very deep oxidation process involves 14 electrons, leading to 65 % selectivity despite what must be a very complex and structure sensitive mechanism.¹ Yet, it is the only commercial application of alkane selective oxidation by a heterogeneous gas-solid catalytic process.¹ Numerous studies have been directed toward understanding the reaction mechanism underlying this remarkable system, but no clear consensus has emerged.¹ The most active phase has been identified as vanadyl pyrophosphate, (VO)₂P₂O₇ (denoted VOPO).¹

Particularly interesting is that each vanadium atom of VOPO is in the +4 oxidation state, leaving one unpaired electron in a $3d$ orbital. This leads to a particularly complex antiferromagnetic coupling and results in numerous studies both experimentally and computationally.

The magnetic structure of VOPO was first thought to be a Heisenberg spin-1/2 ladder model.^{2,3} However, Johnston *et al.* found that the powder magnetic susceptibility data of VOPO can be accurately fitted by the spin-1/2 alternating antiferromagnetic (AFM) Heisenberg chain model.³ More recently, Garrett *et al.* demonstrated that VOPO is best described as an AFM alternating spin-chain along the a axis (with alternating spin exchange couplings J_{OPO} and J_{O} in the chain, **Figure 2.1**) based on the inelastic neutron scattering studies.⁴ Yamauchi *et al.*⁵ and Kikuchi *et al.*⁶ confirmed this result by their NMR and high-field magnetization studies, and proposed that two magnetic components (two types of chains with only slight geometric differences) coexist leading to two spin gaps (33 and 62 K). Indeed, in high-symmetry, high-pressure form of VOPO with all the alternating chains along the a axis being identical, there is only one spin-gap.⁷

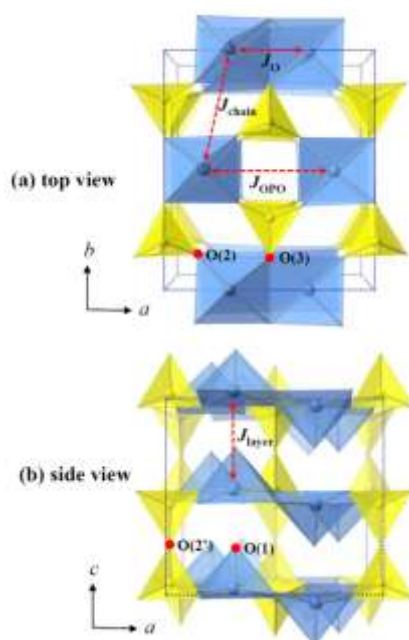


Figure 2.1 Polyhedral views of the crystal structure of VOPO and the schematic description of the spin exchange couplings. The blue polyhedron represents the V_2O_8 motif (V_2O_2 ring) while the yellow represents P_2O_7 . The bulk structure has four distinct types of oxygen: (a) O(1): forming a formal vanadyl double bond ($V=O$) to a single vanadium atom; (b) O(2): the doubly coordinated oxygen forming rather two covalent single bonds ($V-O-P-O-V$) that bridges the VO_5 square pyramid and the PO_4 tetrahedron along the a axis; (c) O(2'): the other doubly coordinated oxygen forming partial covalent bonds to the two phosphorus atoms ($P-O-P$) along the c axis; (d) O(3): the triply coordinated oxygen bridging the two VO_5 square pyramids to form the V_2O_8 motif. This type of oxygen forms $P=O$ double bonds to the P, making only dative (donor-acceptor) bonds to the V.

The magnetism of VOPO has also been studied theoretically based on cluster models.⁸⁻¹¹ By using density functional theory (DFT), Petit *et al.*⁹ have found that the magnetic

structure of VOPO can be approximated by a spin-1/2 alternating AFM Heisenberg model, since the intrachain spin couplings are one order larger in magnitude than interchain ones. The authors also found that amplitude of J_{OPO} is larger than that of J_{O} , suggesting -OPO- is a better pathway than -O- for spin exchange interactions.

Despite numerous studies on this system, a basic question remains unanswered: what is the nature of these spin couplings that leads to this unique magnetic structure? To answer this question, we carried out quantum mechanical (QM) studies of the orthorhombic high-pressure, high-symmetry form of VOPO.⁷

In the course of studying magnetic couplings and their dependence on the cell parameter a , the fragile, dative nature of bonds in the V-O-V bridges was revealed. This suggests a means of incorporating oxygen into VOPO surfaces, a crucial step in catalyzed butane oxidation.¹²

2.2 Computational Details

All calculations used the B3LYP¹³⁻¹⁵ flavor of density-functional theory (DFT) with full three-dimensional periodicity. B3LYP has been shown to predict band gaps of such inorganic oxides accurately since it provides a better description of the localization of the d orbitals.^{16, 17} Thus it is expected to yield spin exchange couplings more accurate than nonhybrid methods such as PBE and PW91.^{18, 19} To describe the various antiferromagnetic and ferromagnetic spin couplings, we used spin-unrestricted and spatially unrestricted B3LYP (UB3LYP, as implemented in the CRYSTAL06 code).

The reciprocal space was sampled with a shrink factor of 3 to define the k -point net (eight k -points in the irreducible Brillouin zone), which we found is sufficiently dense to

provide good numerical accuracy. Each atom is described by an all-electron Gaussian type basis set: 86-411d31G for V,^{20, 21} 85-21d1G for P,²² and 8-411d11G for O,²³ all of which have double zeta plus polarization quality.

We used the primitive orthorhombic $a \times b \times c$ unit cell to study the electronic structures of VOPO (**Figure 2.1**), which includes 52 atoms per unit cell. For studying the magnetic structure, we used a doubled $2a \times b \times c$ supercell, to allow the description of more complex spin configurations. We define the x-axis along a -direction, y-axis along b -direction, and z-axis along the c -direction.

We use DFT broken-symmetry wavefunctions to access to the diagonal elements of the Heisenberg spin Hamiltonian. The calculated J can be compared to the experimental number obtained based on the same Hamiltonian. This has been proved and verified in recent theoretical works.^{24, 25} The Hamiltonian and algorithm used to determine spin couplings from unrestricted DFT energies is detailed in the appendix of this charter.

Since DFT may lead to systematic small errors in determining the equilibrium geometries that might induce systematic changes in the spin exchange coupling, which are very sensitive to geometry, we used the experimental cell parameters and atomic positions⁷ in all studies of the VOPO magnetic and electronic structure, unless specifically stated otherwise.

In addition, we carried out a full optimization of the VOPO bulk structure, including atomic positions and cell parameters under orthorhombic symmetry. This was done to assess the adequacy of the DFT description of this system. The optimized cell parameters are $a = 7.669 \text{ \AA}$, $b = 9.617 \text{ \AA}$, and $c = 8.453 \text{ \AA}$ at 0 K, in a good agreement with

experimental values at 300K ($a = 7.571 \text{ \AA}$, $b = 9.536 \text{ \AA}$, and $c = 8.362 \text{ \AA}$).⁷ In addition, we found that the calculated atomic coordinates deviate from the experimental values an RMS of only 0.07 \AA . This indicates that the UB3LYP functional and basis set combination provides a good description of VOPO, making it suitable for this study.

2.3 Results and Discussion

Electronic structure of VOPO We first studied the electronic structure of this material to determine the bond character, band structure, and density of states.²⁶ From the spin density analysis of the unrestricted DFT wavefunction, we found that the singlet ground state (equal number of up and down spins) has one unpaired spin on each vanadium atom, as expected for V^{IV} (The Mulliken population analysis leads to net spin densities of $+1.11$ or $-1.11 e^-$). This shows that the unpaired electrons are highly localized on each vanadium. We also found that the optimum spin coupling configuration is antiferromagnetic (AFM) along the chains (a axis), while the coupling is ferromagnetic (FM) between the chains along the b and c axis, consistent with experimental results.^{4,7}

The Mulliken charge of VOPO shows that the most nucleophilic site is O(3) ($-1.08 e^-$), followed by O(2) ($-0.93 e^-$), O(2') ($-0.91 e^-$), and then O(1) ($-0.76 e^-$). The larger magnitude for O(3) is expected since it has a double bond to phosphorus and two electropositive vanadium neighbors. This suggests that O(3) may play a role in physical adsorption of the n -butane substrate through electrostatic interactions with the positive hydrogen atoms (Mulliken charges of $\sim +0.10 e^-$).

Our calculated band structure of VOPO (**Figure 2.2**) shows a direct band gap of 3.61 eV at the X point of the Brillouin zone, qualitatively consistent with the experimental

observation (The color is observed to be transparent green,⁷ suggesting a band gap larger than 1.8 eV). In contrast, DFT calculations at the PW91 and LDA level give much smaller band gaps of 0.81 and 0.48 eV, respectively. It is well known that these GGA- and LDA-type functionals lead to band gaps of oxides too small by 2 to 3 eV due to the inability to account for the self-exchange hole. This causes excess delocalization of the electron density in strongly correlated materials containing transition metal or rare-earth metal ions with partially filled $3d$ or $4f$ orbitals.²⁷

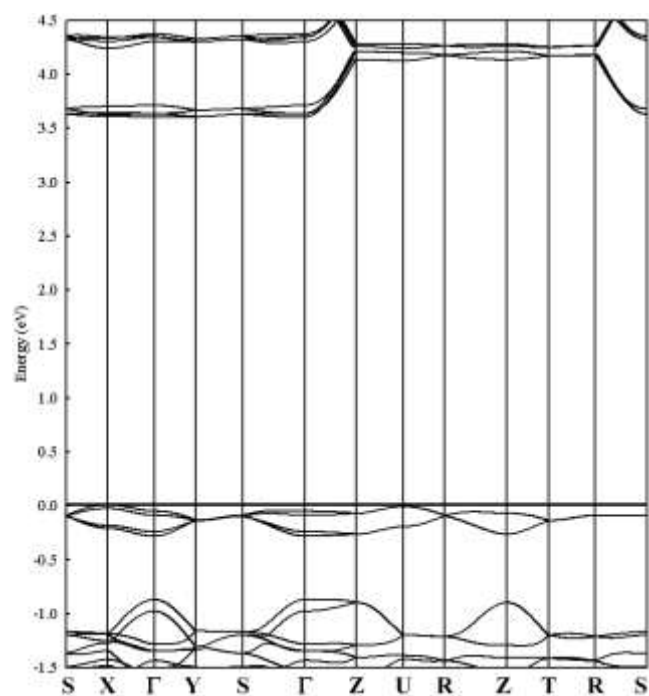
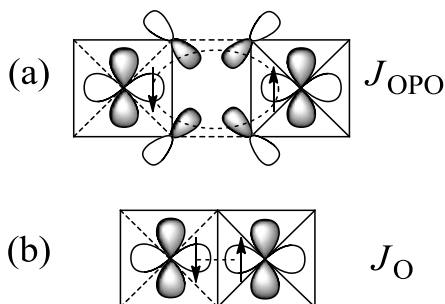


Figure 2.2 Calculated band structure of VOPO. The solid horizontal line marks the top of the valence bands, taken as zero energy.

We found that the HOMO bands (with energy of 0 to 0.3 eV below the red horizontal line) have band widths of only ~ 0.2 eV, which indicates highly localized atomic-like orbitals. In order to obtain more insight into these frontier orbitals, we projected the

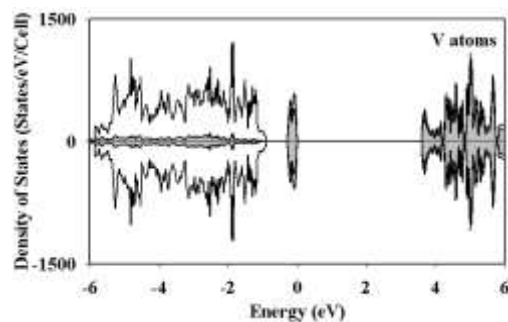
density of states (DOS) onto the various atoms (**Figure 2.3**) and orbitals. The result shows that the HOMO orbitals are comprised by V $3d(x^2-y^2)$ with slight delocalization onto the O(2) $2p(x, y)$. From analyzing the eigenvectors, we found that there is an antibonding coupling between V $3d(x^2-y^2)$ and O(2) $2p(x, y)$ (**Scheme 2.2** (a)). It is the overlap between the two O(2) on the same P (V-O(2)-P-O(2)-V) that is responsible for the superexchange coupling resulting in the AFM coupling. A similar description was proposed by Koo *et. al*⁸ based on reduced cluster models.

On the other hand, the LUMO orbitals (bands with energy of 3.6 to 4.5 eV above the red horizontal line) have widths of ~ 0.8 eV and a maximum energetic dispersion along the $\Gamma \rightarrow Z$ direction, implying a strong coupling of the antibonding orbitals on one V=O with those of the adjacent V=O along the c axis. Those orbitals are comprised of V $3d(xz, yz)$ and O(1) $2p(x, y)$, with V $3d(xz, yz)$ -O(1) $2p(x, y)$ π^* character. The V=O(1) could play a role in *n*-butane C-H activation through interactions between V=O(1) π^* and C-H σ bonds. The possible involvement of this orbital interaction in C-H bond cleavage is also suggested by Robert *et al.*²⁸ In contrast, O(2'), O(3), and P have no significant contributions to both HOMO and LUMO.

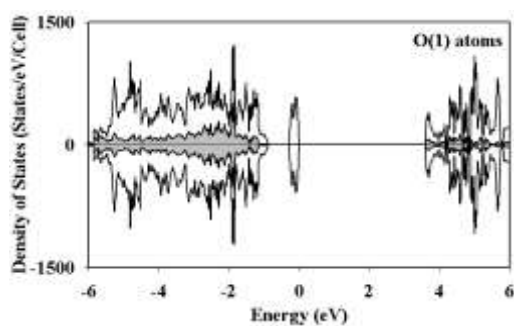


Scheme 2.2 Local molecular orbitals responsible for spin exchange couplings

(a) V atoms



(b) O(1) atoms



(c) O(2) atoms

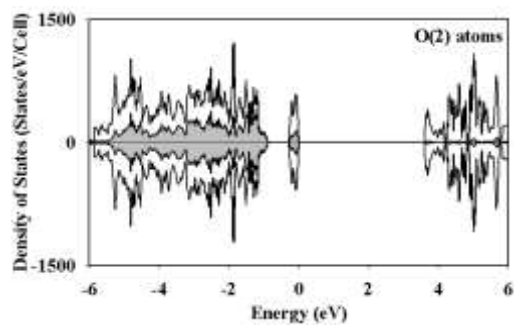


Figure 2.3 The projected density of states (shaded) for V, O(1), and O(2) atoms superimposed on the total density of states (unshaded) for VOPO. The energy zero is placed at the top of the valence bands.

Magnetic structure of VOPO Having elucidated the electronic structure of VOPO, we further studied its magnetic structure, focusing on spin exchange couplings between

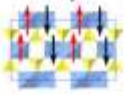
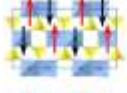
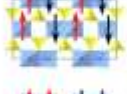
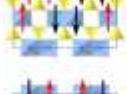
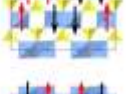
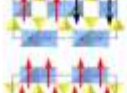
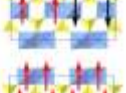
nearest-neighbor pairs of vanadium atoms. Four different types of spin couplings are present in VOPO (**Figure 2.1**):

1. J_O : the spin coupling between a pair of vanadium atoms within the V_2O_8 motif connected by two -O(3)(=P)- units.
2. J_{OPO} : the spin coupling between a pair of vanadium atoms linked by two -O(2)-P-O(2)- units.
3. J_{chain} : the spin coupling between vanadium atoms in two adjacent chains (interchain interaction), connected through -O(3)-P-O(2)-.
4. J_{layer} : the spin coupling between two vanadium atoms in two adjacent layers (interlayer interaction), connected indirectly through O(1).

The ground state from the UDFT calculations (denoted as Conf. 1, **Table 2.1**) is taken as the reference point.

We first determined J_{chain} by flipping all the spins in the second chain on both layers (Conf. 2), so that the interchain interactions all become AFM instead of FM. The energy of Conf. 2 increases by only 10.0 K, suggesting that interchain interactions are FM with $J_{\text{chain}} \approx +0.6$ K.

Table 2.1 Relative energies (in K) for various spin configurations of VOPO. The energy components for each spin configuration are based on the formula derived in the appendix.

	Configuration		Energy Component	ΔE
	1 st layer	2 nd layer		
1			$8J_O + 8J_{OPO}$	0.0
2			$8J_O + 8J_{OPO} + 16J_{chain}$	10.0
3			$8J_O + 8J_{OPO} + 16J_{layer}$	333.6
4			$8J_{OPO} + 8J_{chain}$	583.6
5			$8J_O + 8J_{chain}$	1292.2
6			0	1805.8

Next, we evaluated the interlayer interaction by flipping all the spins in the second layer, so that the interlayer interaction is AFM instead of FM (Conf. 3). We found that the energy increases by 333.6 K, indicating that interlayer interactions are FM with $J_{layer} \approx +21$ K. The stronger interlayer coupling compared to interchain is due to the closeness of each V=O(1) to the V=O(1) of the next layer and the small direct charge transfer.

We then investigated the two types of the intrachain interaction (J_O first and then J_{OPO}). Conf. 4 has FM coupling for J_O , but AFM coupling for J_{OPO} , leading to an energy 583.6 K higher than the ground state. This arises from eliminating $8J_O$ and adding $8J_{chain}$. On the other hand, Conf. 5 introduces FM coupling in J_{OPO} , while J_O and the interlayer interaction remain the same as the ground state. This leads to an energy 1292.2 K higher than the ground state, due to the removal of $8J_{OPO}$ and adding $8J_{chain}$. Thus comparing the energy between Conf. 4 and 5, we deduce $J_{OPO} - J_O \approx -89$ K indicating much stronger AFM

coupling for J_{OPO} than J_{O} . This shows that -O(2)-P-O(2)- provides a better exchange pathway than does -O(3)- in VOPO.

In order to calculate the most accurate spin exchange couplings, we calculated an additional 10 different spin configurations for VOPO. Then we did a least-square fitting to these energies to obtain the magnitude for each of the four J parameters defined above.

These results lead to spin couplings of $J_{\text{OPO}} = -156.8$ K and $J_{\text{O}} = -68.6$ K (**Table 2.2**), indicating that the dominant magnetic structure of VOPO can be captured by a one-dimensional Heisenberg alternating chain model as suggested by inelastic neutron scattering experiments,⁴ and the best interaction pathway is through the -O(2)-P-O(2)- bridge with a V-V separation of 5.22 Å rather than -O(3)- with a V-V distance of 3.23 Å, which also agrees with NMR experiments.⁶

Table 2.2 Comparison between experimental and theoretical predicted values of J parameters in the high-symmetry, high-pressure form of VOPO (unit: K)

reference	intrachain		interlayer	interchain
	J_{O}	J_{OPO}	J_{layer}	J_{chain}
this work	-68.6	-156.8	19.2	2.8
Saito	-114.5	-131.6	<i>na</i>	<i>na</i>
Petit	-105	-144 (200)	37	6

The interlayer interaction is $J_{\text{layer}} = 19.2$ K (FM) with a V-V separation of 3.79 Å, while the interchain coupling is $J_{\text{chain}} = 2.8$ K (FM) with a V-V separation of 4.87 Å. The smaller couplings compared to intrachain interactions suggest that direct, ferromagnetic exchange interactions dominate over antiferromagnetic ones.

Comparing with the experimental results, we found that our calculated J_{OPO} deviates from the experimental value ($J_{\text{OPO}} = -131.6 \text{ K}$)⁷ by 19.1 %. This is probably partly due to limitations of DFT but it may arise from the use of a one-dimensional model to extract J from the experiments, ignoring the interlayer (19.2 K) and interchain couplings (2.8 K), which may influence intrachain couplings. Our J_{OPO} is consistent with one of calculated number (-144 K) by Petit *et al.*,⁹ but not with the other number (-200 K) based on a different cluster model.

Of most concern is the large discrepancy (45.9 % deviation) between theory and experiment for J_{O} , with the experimental value (-114.5 K)⁷ nearly twice as high as the calculation (-68.6 K). As we show in the following sections, this may be due to weak dative V-O(3) bonds in the V_2O_8 motif making J_{O} , a direct spin exchange coupling, extremely sensitive to structural fluctuations.

Influence of the Cell Parameter a in the Magnetic Structure In order to elucidate the nature of the spin exchange couplings in VOPO, we examined the dependence of J on the cell parameter a . To do so, we compressed a from the experimental value by 3 % and expanded it by 5 %, optimizing in each case all atomic positions using the FM spin configuration. Here we solved for the six spin configurations and least-squares-fitted to obtain the spin couplings as a function of a . For the experimental structure, the use of just six spin configurations instead of 16 gives $J_{\text{OPO}} = -158.5 \text{ K}$, $J_{\text{O}} = -69.9 \text{ K}$, $J_{\text{layer}} = 17.8 \text{ K}$, and $J_{\text{chain}} = 8.4 \text{ K}$, quite similar to those obtained based on 16 configurations ($J_{\text{OPO}} = -156.8 \text{ K}$, $J_{\text{O}} = -68.6 \text{ K}$, $J_{\text{layer}} = 19.2 \text{ K}$, and $J_{\text{chain}} = 2.8 \text{ K}$).

Indeed the cell parameter a has a dramatic impact on J_{O} (**Figure 2.4**). At 3 % compression ($R(\text{V--V}) = 3.13 \text{ \AA}$), J_{O} is AFM with a value of -190.2 K, even larger in

magnitude than $J_{\text{OPO}} = -175.4$ K. As a expands, the magnitude of J_{O} decreases rapidly, changing sign to FM ($J_{\text{O}} = +31.2$ K) at 5% expansion ($R(\text{V--V}) = 3.48$ Å). The large variation of J_{O} with the cell parameter a (or V--V bond distance) and the insignificant contribution of O(3) to the HOMO indicate that J_{O} results from the overlap of $3d(x^2-y^2)$ orbitals of a pair vanadium in the same V_2O_8 motif, a direct through-space exchange coupling (**Scheme 2.2** (b)). The same type of exchange mechanism is also responsible for the AFM ground state for the hydroxo- and alkoxo-bridged dinuclear oxovanadium(IV) compounds.²⁹ Petit *et al.*⁹ also calculated J_{O} as a function of the V-V distances present in three phases of VOPO and observed a quasi-linear dependence over the smaller range of V-V distances (less than 3% variation) spanned by the three crystal structures.

In contrast, J_{OPO} , J_{layer} , and J_{chain} are relatively insensitive to the cell parameter a . J_{OPO} varies from -175.4 to -136.4 K, J_{layer} varies from 10.2 to 19.4 K, and J_{chain} varies from 8.8 to 1.8 K, none of which changes sign.

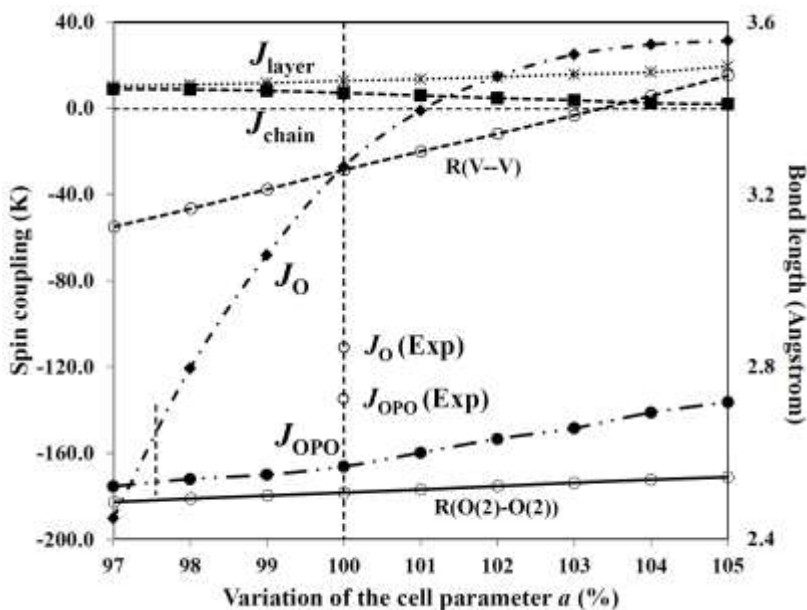
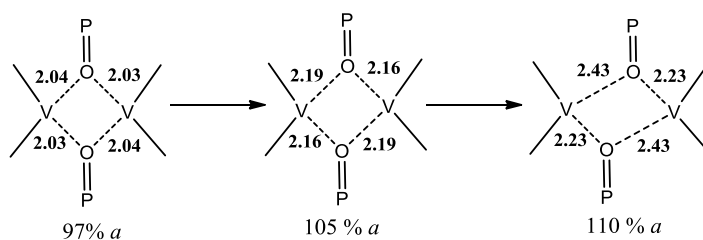


Figure 2.4 The dependence of spin couplings on the cell parameter a . At the experimental a , we calculated J_O/J_{OPO} to be 0.44. However, compressing a by just 2.5% (indicated by the short black vertical line) leads to $J_O/J_{OPO} = 0.89$, similar to the experimental value of 0.87. The horizontal dashed line marks $J = 0$.

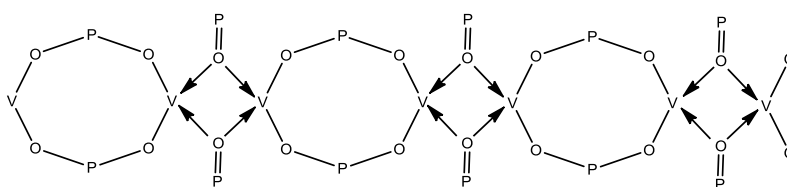
Our discovery that J_O is highly sensitive to the cell parameter a shows that the magnetic structure of VOPO depends on a . Thus for 3 % to 0 % compression, the system is best described by a spin-1/2 Heisenberg AFM-alternating-chain model, while at 1% to 3% expansion it is best described with a spin-dimer model. These results also suggest that the spin gap of the spin-1/2 Heisenberg alternating chain, which is a function of J_O and J_{OPO} ,³⁰ depends very sensitively on the cell parameter a . Consequently, we suggest that the spin gap and magnetic structure of VOPO should depend sensitively on pressure.

Analyzing the structural parameters at different a 's, we found that $R(V-O(3))$ increases from 2.04 and 2.03 Å to 2.19 and 2.16 Å (6.9 % variation), as the a lattice parameter increases from 97% to 105%. Further expanding a to 110 % increases the V-O(3) bond lengths to 2.43 and 2.23 Å. At this point we found that the V_2O_8 cluster distorts such that one P=O(3) group makes a donor-acceptor bond to one V, while the other P=O(3) group makes a donor-acceptor bond to the other V (**Scheme 2.3**).



Scheme 2.3

In contrast, V-O(2) increases from 1.92 to 1.98 Å (only 3.0 % variation), as the lattice parameter is changed from 97% to 105%. Further expanding to 110% leads to the V-O(2) bond length of 1.98 Å, the same as that at the 5 % expansion. Based on this asymmetric relaxation of atomic positions, we see that V-O(2) has a rigid covalent single bond while V-O(3) has a fragile dative bond. The Valence-Bond structure of VOPO is shown in **Scheme 2.4**.



Scheme 2.4 The Valence Bond description of the bonding along the chain. The P has three P-O bonds not shown plus a double bond to O(3), so that O(3) makes only dative bonds (donor-acceptor or Lewis Base-Acid bonds) to the two vanadium atoms. This weak bonding leads to no significant super-exchange so that the direct $V 3d(x^2-y^2) - V 3d(x^2-y^2)$ overlap dominates, leading to an exponential dependence of J_O on distance.

To illustrate this, we built the cluster model (the inset of **Figure 2.5**) containing this J_O spin coupling,³¹ in which the phenomenon is reproduced. The spin coupling is AFM with a $J_O = -274.7$ K when the V-V distance is fixed at 3.1 Å. This coupling is weakened as R(V-V) increases, and finally becomes FM with a value of +8.4 K at R(V-V) = 3.6 Å. Importantly, we found the energy cost to totally dissociate this cluster into two fragments is only 9.2 kcal/mol, suggesting V-O(3) binding energy is only 4.6 kcal/mol.

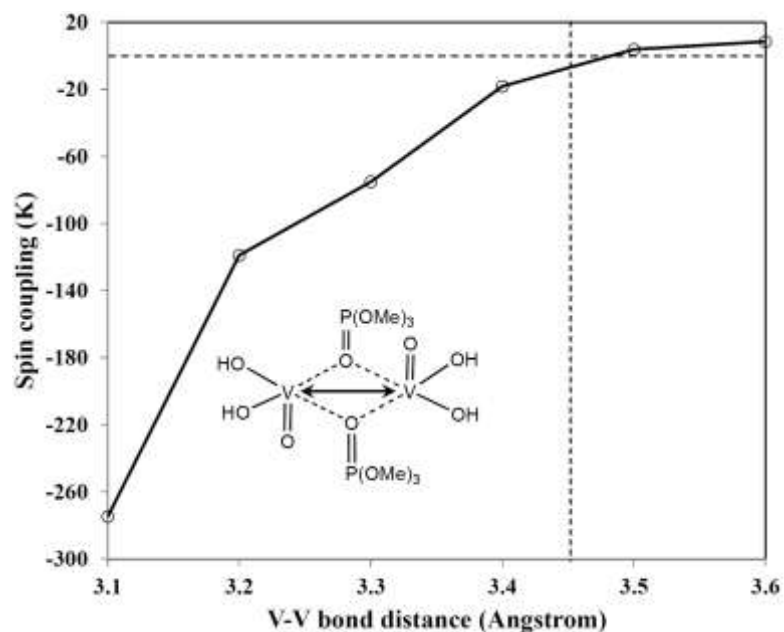


Figure 2.5 The dependence of the spin coupling on the V-V distance in the $V_2O(3)_2$ cluster model. The horizontal dashed line marks $J = 0$, and the vertical dashed line marks the equilibrium the V-V distance (3.47 Å).

Implication for the Catalytic Reaction TAP (temporal analysis of products) reactor experiments³² showed that with a sufficient dose of oxygen on the VOPO surface prior to exposure to *n*-butane, subsequent exposure to butane leads selectively to fully oxidized maleic anhydride without intermediates being released. This shows that the reaction is localized and that all seven oxygen required for completing the reaction are somehow stored near the surface and accessible to the substrate. Indeed, it has been shown by ³¹P NMR that in the working VOPO catalyst small portion of V^{+4} has been oxidized to V^{+5} .^{33, 34} Moreover, Coulston *et al.* showed that a small amount of V^{+5} is crucial for a successful catalyst, based on in situ X-ray absorption spectroscopy studies.¹²

We consider that the observation that there is essentially no interaction between O(3) and vanadium is important, because it suggests that gas phase O₂ can penetrate to subsurface layers, while oxidizing the vanadium atoms from +4 to +5 oxidation state to store sufficient O atoms for the full oxidation. That is, under thermal expansion or chemical reactions, the V₂O(3)₂ four-membered rings may open up forming a channel, so that gaseous O₂ molecules can go inside VOPO and oxidize multiple layers.

2.4 Conclusions

From DFT calculations, we found the magnetic structure of VOPO can be described in terms of four different types of spin couplings in VOPO: $J_{\text{OPO}} = -156.8$ K, $J_{\text{O}} = -68.6$ K, $J_{\text{layer}} = 19.2$ K, and $J_{\text{chain}} = 2.8$ K. This confirms that the magnetic structure of VOPO is best described by a spin-1/2 Heisenberg AFM alternating chain model, consistent with experiments by inelastic neutron scattering⁴ and NMR.^{5,6}

By varying the cell parameter a and analyzing the responses of spin exchange couplings and structural parameters, we found that J_{OPO} and J_{O} result from two very different exchange mechanisms: J_{OPO} originates from superexchange interactions through the -O(2)-P-O(2)- link, whereas J_{O} results from a direct overlap of $3d(x^2-y^2)$ orbitals of two vanadium atoms in the same V₂O₈ motif and therefore is very sensitive to structural fluctuations. Moreover, we also found that V-O bonds of V-(O(2)PO(2))₂-V are covalent and rigid, whereas the bonds of V-(O(3))₂-V are fragile and dative. These results suggest that pressure would dramatically change the magnetic structure and spin gap of VOPO, which should be observable experimentally.

Regarding catalysis, the bonding pattern suggests that under thermal expansions or chemical reactions, the $V_2O(3)_2$ four-membered rings may open up forming a channel, so that multiple O_2 molecules can be stored inside the VOPO by reacting with vanadium atoms beneath the surface.

2.5 Appendix

The interaction between two magnetic ions can be described by a Heisenberg spin Hamiltonian

$$\hat{H}^{spin} = -J\hat{S}_1 \cdot \hat{S}_2 \quad (1)$$

where J is the spin exchange parameter and \hat{S}_1 and \hat{S}_2 are the spin angular momentum operators for two adjacent magnetic sites. The system favors parallel spins (FM) if J is positive and antiparallel (AFM) if J is negative.

Considering just two spins, we can write the total spin operator as $\hat{S} = \hat{S}_1 + \hat{S}_2$ leading to $\hat{S}^2 = \hat{S}_1^2 + \hat{S}_2^2 + 2\hat{S}_1 \cdot \hat{S}_2$. Hence equation (1) can be rewritten as

$$\hat{H}^{spin} = -\frac{J}{2}(\hat{S}^2 - \hat{S}_1^2 - \hat{S}_2^2) \quad (2)$$

Assuming just one unpaired electron on each site, we take $\hat{S}_1 = \hat{S}_2 = 0.5$, leading to $E_T = -0.25J$ for the triplet state and $E_S = 0.75J$ for the singlet. Consequently, the J parameter can be obtained by comparing the energy difference between the singlet and triplet states

$$J = E_s - E_T \quad (3)$$

However, current generations of DFT methods do not allow the multiple determinants needed to describe pure singlet states. For two electrons the singlet state requires two determinants (the simple GVB wavefunction). Thus for two electrons our calculation on the AFM singlet state leads to the wave function:

$$\psi_{S'} = \frac{1}{\sqrt{2}} [a(1)\alpha(1)b(2)\beta(2) - b(1)\beta(1)a(2)\alpha(2)]$$

, where a and b are localized singly occupied orbitals. The wave functions of the correct singlet and triplet states are:

$$\psi_S = \frac{1}{2\sqrt{1+S_{ab}^2}} [a(1)b(2) + b(1)a(2)] [\alpha(1)\beta(2) - \beta(1)\alpha(2)]$$

$$\psi_T = \frac{1}{2\sqrt{1-S_{ab}^2}} [a(1)b(2) - b(1)a(2)] [\alpha(1)\beta(2) + \beta(1)\alpha(2)] .$$

where S_{ab} is the overlap of two singly occupied magnetic orbitals and we have assumed that the orbitals a and b are the same for singlet and triplet. Writing $\psi_{S'}$ as a linear combination of ψ_S and ψ_T :

$$\psi_{S'} = \sqrt{\frac{1+S_{ab}^2}{2}} \psi_S + \sqrt{\frac{1-S_{ab}^2}{2}} \psi_T$$

the energy becomes

$$E_{S'} = \left(\frac{1+S_{ab}^2}{2} \right) E_S + \left(\frac{1-S_{ab}^2}{2} \right) E_T = \left(\frac{1+2S_{ab}^2}{4} \right) J$$

This leads to a relation between J , $E_{S'}$, and E_T :

$$J = \frac{2(E_{S'} - E_T)}{1+S_{ab}^2} \quad (4)$$

In the VOPO systems, S_{ab} is approximately zero, since the unpaired electrons are highly localized at vanadium atoms. As a result, equation (4) becomes:

$$J = 2 \times (E_S - E_T). \quad (5)$$

This formula is first proposed by Noodleman³⁵ at 1981 and has been applied to numerous magnetic systems successfully. We use equation (5) to obtain the J parameters in VOPO.

2.6 Notes and References

1. B. K. Hodnett, *Heterogeneous Catalytic Oxidation*, John Wiley & Sons Ltd, New York, NY, 2000.
2. R. S. Eccleston, T. Barnes, J. Brody and J. W. Johnson, *Phys. Rev. Lett.*, 1994, **73**, 2626-2629.
3. D. C. Johnston, J. W. Johnson, D. P. Goshorn and A. J. Jacobson, *Phys. Rev. B*, 1987, **35**, 219-222.
4. A. W. Garrett, S. E. Nagler, D. A. Tennant, D. A. Sales and T. Barnes, *Phys. Rev. Lett.*, 1997, **79**, 745-748.
5. T. Yamauchi, Y. Narumi, J. Kikuchi, Y. Ueda, K. Tatani, T. C. Kobayashi, K. Kindo and K. Motoya, *Phys. Rev. Lett.*, 1999, **83**, 3729-3732.
6. J. Kikuchi, K. Motoya, T. Yamauchi and Y. Ueda, *Phys. Rev. B*, 1999, **60**, 6731-6739.
7. T. Saito, T. Terashima, M. Azuma, M. Takano, T. Goto, H. Ohta, W. Utsumi, P. Bordet and D. C. Johnston, *J. Solid State Chem.*, 2000, **153**, 124-131.
8. H. J. Koo and M. H. Whangbo, *Inorg. Chem.*, 2000, **39**, 3599-3604.
9. S. Petit, S. A. Borshch and V. Robert, *J. Am. Chem. Soc.*, 2002, **124**, 1744-1749.

10. H. J. Koo, M. H. Whangbo, P. D. VerNooy, C. C. Torardi and W. J. Marshall, *Inorg. Chem.*, 2002, **41**, 4664-4672.
11. M. L. Lawson Daku, S. Borshch, V. Robert and B. Bigot, *Phys. Rev. B*, 2001, **6317**, -.
12. G. W. Coulston, S. R. Bare, H. Kung, K. Birkeland, G. K. Bethke, R. Harlow, N. Herron and P. L. Lee, *Science*, 1997, **275**, 191-193.
13. A. D. Becke, *Phys Rev A*, 1988, **38**, 3098-3100.
14. A. D. Becke, *J. Chem. Phys.*, 1993, **98**, 5648-5652.
15. C. T. Lee, W. T. Yang and R. G. Parr, *Phys. Rev. B*, 1988, **37**, 785-789.
16. J. Muscat, A. Wander and N. M. Harrison, *Chem. Phys. Lett.*, 2001, **342**, 397-401.
17. J. K. Perry, J. Tahir-Kheli and W. A. Goddard, *Phys. Rev. B*, 2001, **6314**, 144510.
18. D. Munoz, N. M. Harrison and F. Illas, *Phys. Rev. B*, 2004, **69**, 085115.
19. R. L. Martin and F. Illas, *Phys. Rev. Lett.*, 1997, **79**, 1539-1542.
20. W. C. Mackrodt, N. M. Harrison, V. R. Saunders, N. L. Allan, M. D. Towler, E. Apra and R. Dovesi, *Philos. Magaz. A*, 1993, **68**, 653-666.
21. E. Ruiz, M. Llunell and P. Alemany, *J. Solid State Chem.*, 2003, **176**, 400-411.
22. C. M. Zicovich-Wilson, A. Bert, C. Roetti, R. Dovesi and V. R. Saunders, *J. Chem. Phys.*, 2002, **116**, 1120-1127.
23. L. Valenzano, F. J. Torres, D. Klaus, F. Pascale, C. M. Zicovich-Wilson and R. Dovesi, *Z. Phys. Chem.*, 2006, **220**, 893-912.
24. D. D. Dai and M. H. Whangbo, *J. Chem. Phys.*, 2003, **118**, 29-39.
25. I. D. R. Moreira and F. Illas, *Phys. Rev. B*, 1997, **55**, 4129-4137.
26. DFT fully optimized VOPO leads to the same Mulliken populations, band structure, and density of states, as found using the experimental structure.

27. V. I. Anisimov, A. I. Poteryaev, M. A. Korotin, A. O. Anokhin and G. Kotliar, *J. Phys. Condens. Matter*, 1997, **9**, 7359-7367.
28. V. Robert, S. A. Borshch and B. Bigot, *J. Mol. Catal. A*, 1997, **119**, 327-333.
29. A. Rodriguez-Forteza, P. Alemany, S. Alvarez and E. Ruiz, *Eur. J. Inorg. Chem.*, 2004, 143-153.
30. J. C. Bonner and M. E. Fisher, *Phys. Rev.*, 1964, **135**, A640.
31. For the finite cluster model, all calculations were carried out with Jaguar 7.0 using the B3LYP hybrid-density functional. For the geometry optimizations, we used the Los Alamos effective core potential (ECP) with the double- ζ contraction of valence functions for vanadium and phosphorus atoms and 6-31G** for the others.
32. J. T. Gleaves, J. R. Ebner and T. C. Kuechler, *Catal. Rev. Sci. Eng.*, 1988, **30**, 49-116.
33. J. Li, M. E. Lashier, G. L. Schrader and B. C. Gerstein, *Appl. Catal.*, 1991, **73**, 83-95.
34. M. T. Sananes, A. Tuel and J. C. Volta, *J. Catal.*, 1994, **145**, 251-255.
35. L. Noodleman, *J. Chem. Phys.*, 1981, **74**, 5737-5743.

*Chapter 3***THE PARA-SUBSTITUENT EFFECT AND PH-DEPENDENCE OF THE ORGANOMETALLIC BAEYER-VILLIGER OXIDATION OF RHENIUM-CARBON BONDS****3.1 Introduction**

The development of an efficient oxy-functionalization reaction that can be integrated with C-H activation reactions is a key challenge in developing selective, low-temperature (< 250 °C) hydrocarbon oxidation catalysts. Facile oxy-functionalization reactions of nucleophilic $M^{\delta+}-R^{\delta-}$ complexes are rare,¹⁻⁵ although functionalizations are well-known for $M^{\delta-}-R^{\delta+}$ intermediates of more electronegative metals.⁶⁻⁸

Some of us reported recently both theory and experiments on the reaction of methylrhenium trioxide (CH_3-ReO_3 , MTO) with oxidants (H_2O_2 , PhIO, and IO_4^-) in the aqueous phase.^{2,9} We concluded that the reaction proceeds through a Baeyer-Villiger (BV) type transition state⁹ leading to formation of methanol in high yields (> 80 %). More recently, we studied the oxidation of 2,4,6-trimethylphenylrhenium trioxide (Mes- ReO_3 , MesTO) in similar conditions.⁴ We found that the lowest-barrier pathway is also through a BV type oxygen insertion, and that the replacement of alkyl by aryl migrating groups leads to an increase in the reaction rate.

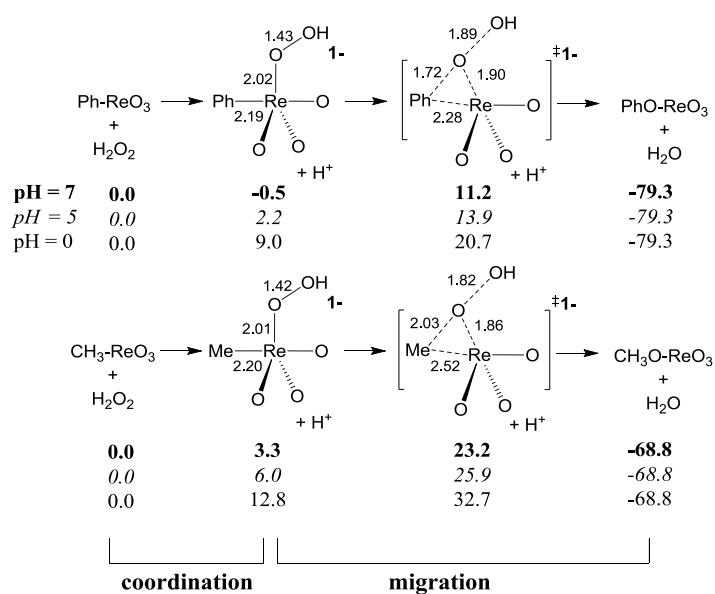
To aid in understanding how this stoichiometric transformation might be integrated into complete catalytic cycles, we here utilized density functional theory (M06 functional)¹⁰ to study the effect of *para*-substitution on the oxidation of phenylrhenium

trioxide (Ph-ReO₃, PTO) by H₂O₂. We also investigated the pH-dependence of this BV type oxidation, since the rate of complementary steps such as substrate coordination, C-H cleavage, and oxidation often are pH dependent.¹¹⁻¹⁵

3.2 Results and Discussion

We began this study by calculating the aqueous phase Gibbs free energy surface of the oxidation of PTO by H₂O₂ (1M) at pH = 7 and comparing to that of MTO (**Scheme 3.1**). The weaker electron-donating ability of phenyl relative to methyl¹⁶ leads to a less electron-rich Re center and stronger coordination of HOO⁻ to PTO. The coordination of HOO⁻ to Re is 0.5 kcal/mol downhill for PTO, whereas it is 3.3 kcal/mol uphill for MTO (BV-OH pathway). The barrier for oxy-insertion is 11.7 kcal/mol for PTO; whereas, it is 23.2 kcal/mol for MTO. This suggests that PTO is more reactive toward the oxidation than MTO, consistent with the instantaneous reaction of PTO upon mixing at room temperature.⁴ The higher migratory aptitude of phenyl over methyl is also observed in the organic Baeyer-Villiger,¹⁷ pinacol,¹⁸ and Wagner-Meerwein rearrangements.¹⁹

This trend can be explained by an interaction of the phenyl π -orbitals with an antibonding linear combination of Re- d_{π} and O- p_{π} orbitals which helps stabilize the transition state (**Scheme 3.2**).^{20,21} A similar orbital interaction is also responsible for a facile Ph 1,2-migration across the Re-O bonds of a Re(VII) bis-oxo system.^{1,22} Our calculations also suggest that, similar to MTO, the oxidation of PTO by H₂O₂ is highly exergonic ($\Delta G = -79.9$ kcal/mol) and thus irreversible, consistent with experiments.^{2,4}



Scheme 3.1 Gibbs free energy (kcal/mol) surfaces of PTO and MTO Baeyer-Villiger oxidation with a hydroxide leaving group, including aqueous solvation (BV-OH-pathway).



Scheme 3.2 Phenyl aromatic orbital overlapping the antibonding linear combination of Re-d π and O-p π orbitals.

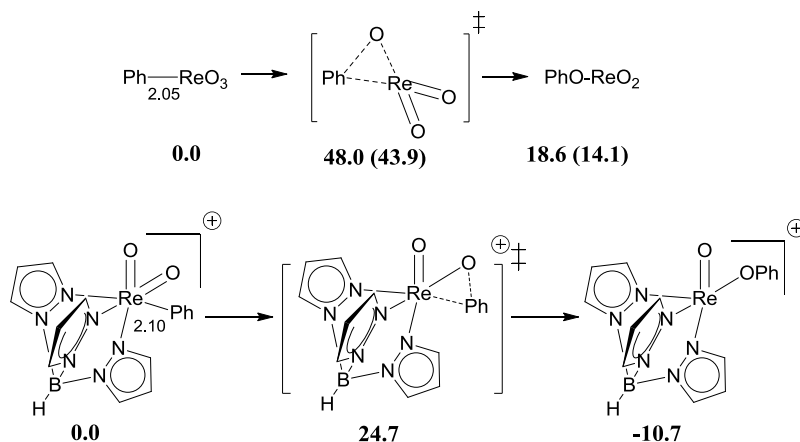
Interestingly, at the transition state (TS), methyl is more distant from the Re moiety

($R_{C-Re} = 2.52 \text{ \AA}$, $R_{C-O} = 2.03 \text{ \AA}$) than phenyl ($R_{C-Re} = 2.28 \text{ \AA}$, $R_{C-O} = 1.72 \text{ \AA}$). This led us to suspect that a significant amount of singlet diradical character may exist in this TS, and that the electronic structure at the TS might not be well described by the usual spin-restricted density functional formalism (R-M06). To test this we carried out a CCSD calculation²³ at the R-M06-optimized TS structure yielding a T1 diagnostic²⁴ of 0.027. This value is slightly higher than the 0.02 threshold suggested for determining whether single determinant methods can be successfully applied.²⁴ The T1 diagnostic is only 0.021 for the PTO TS.

However, full optimization of the MTO TS using CCSD leads to a structure ($R_{C-Re} = 2.58 \text{ \AA}$, $R_{C-O} = 2.07 \text{ \AA}$, and $R_{O-O} = 1.84 \text{ \AA}$) that is almost identical to that from the R-M06 functional. Moreover, CCSD gives a barrier (electronic energy only with LACVP** basis set) of 35.0 kcal/mol, which is also similar to 31.1 kcal/mol from R-M06. Therefore, we conclude although this organometallic BV transition state possesses some singlet diradical character, most of its electronic structure can be captured by R-M06.

In contrast to the facile BV type pathway, we find that the direct 1,2-phenyl migration across a Re-oxo bond poses a barrier of 43.9 kcal/mol (48.0 kcal/mol when only gas phase electronic energies from LACV3P++** basis set are considered, **Scheme 3.3**). Brown and Mayer have reported a similar, but facile, 1,2-phenyl migration in the rhenium(VII) dioxo phenyl complex ($TpReO_2Ph^+$; $Tp = \text{hydridotris(pyrazolyl)borate}$) with a Gibbs free energy barrier of only 20.9 kcal/mol.¹ Comparing the electronic energy of the two migration reactions, we find that the migration barrier of $TpReO_2Ph^+$ is 23.3 kcal/mol lower than that of $Ph-ReO_3$. For $TpReO_2Ph^+$, the migration leads to a stable five-coordinate product (-10.7 kcal/mol downhill compared to the reactant), whereas for

Ph-ReO₃ the migration leads to the formation of an unstable three-coordinate Re complex (18.6 kcal/mol uphill). High coordination stabilizes products and destabilizes the initial Re-C bond through the orthogonalization of covalent and dative bonding orbitals. Also, the Re-oxo moiety of the Tp complex is more electrophilic, as determined either by the core orbital energies (the Re-5s and the O-1s orbitals are 1.0 eV and 1.2 eV deeper in the Tp complex, respectively) or oxo Mulliken charges (-0.55 in the Tp complex and -0.65 in PTO). These suggest that, for d⁰ oxo complexes, the thermodynamics and kinetics of direct migration are promoted by a high coordination number and strong electrophilicity.



Scheme 3.3 Gas phase electronic energy surfaces of direct phenyl migrations across Re=O bonds (kcal/mol, Gibbs free energies including aqueous solvation in parentheses, initial Re-C bond lengths marked in Angstroms).

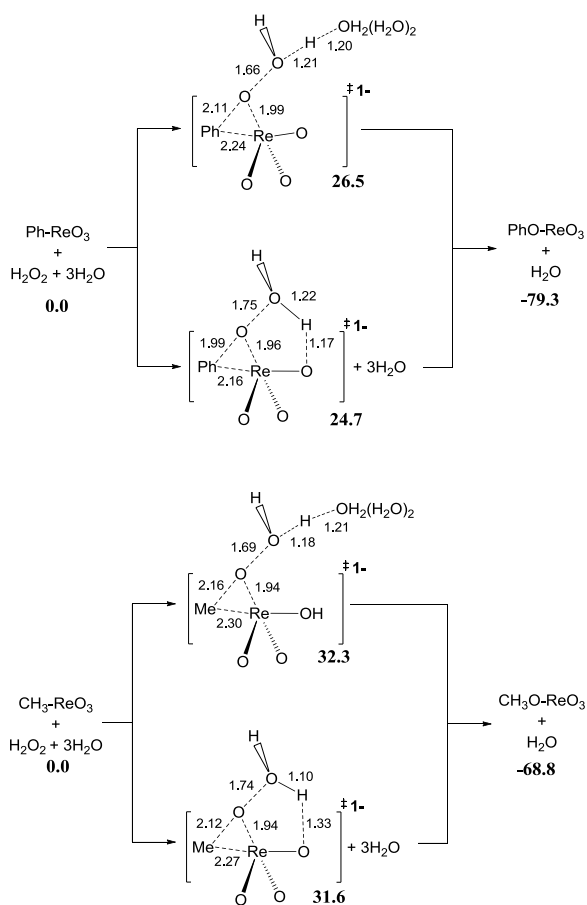
In the BV reaction, OH⁻ is liberated and eventually neutralized by protonation (BV-OH pathway); thus the reaction barrier may be lowered if the leaving group is H₂O

instead of OH^- (BV- H_2O pathway). This new pathway has not been fully investigated before,^{4,9} so we examined this possibility herein. Concurrently, we explored the influence of pH on the two different pathways. We located two types of transition states for the BV- H_2O energy surface (**Scheme 3.4**). In the top example, a proton from solvent (represented by three explicit water molecules in addition to the polarizable continuum solvent) is transferred to the OH^- to form H_2O water during the course of the migration. In the second case, the proton transfer is intramolecular: a proton bound to one of the three oxo groups (presumably provided by H_2O_2 initially) is transferred to OH^- to form H_2O . The Gibbs free energy barriers at $\text{pH} = 7$ are 27.0 and 25.2 kcal/mol for PTO and 32.3 and 31.6 kcal/mol for MTO (taking the peroxide complex as resting state for $\text{R} = \text{Ph}$). Importantly, these barriers are much higher than those with OH^- as a leaving group (11.7 and 23.2 kcal/mol for PTO and MTO, respectively). This suggests that despite having a poorer leaving group, BV-OH is still a more favorable pathway than BV- H_2O at $\text{pH} = 7$.

In the BV-OH pathway one proton is released from hydrogen peroxide upon coordination to R-ReO_3 ($\text{R} = \text{CH}_3, \text{Ph}$). This suggests that the coordination energies and the overall BV barriers are pH-dependent. In contrast, since no proton is liberated in BV- H_2O , its overall barrier is pH independent. Accordingly, a change in solution pH may change which pathway has the lowest-barrier. Since it is well known that trioxorhenium-hydrocarbyl bonds hydrolyze rapidly in basic aqueous solutions, but slowly in acidic media,^{25,26} we will discuss only the low-pH regime here.

Decreasing pH disfavors liberation of a proton, and therefore destabilizes the hydrogen peroxide complex and the BV-OH transition state. The hydrocarbyl migration

barrier remains unaffected, but the overall barrier increases as the pH value decreases. For example, for the PTO system where $\text{pH} = 5$, the coordination energy is uphill by 2.2 kcal/mol and the overall barrier is increased to 13.9 kcal/mol (**Scheme 3.1**). As the environment becomes more acidic, the overall barrier of the pathway BV-OH increases, whereas that of BV-H₂O remains unchanged. Eventually, under strongly acidic conditions, BV-H₂O becomes the most favorable low energy pathway. Our calculations suggest that for PTO, BV-H₂O would be more favorable than BV-OH only below $\text{pH} = -2.8$, and for MTO the crossover takes place at $\text{pH} = 0.9$. Since BV-OH is energetically more favorable than BV-H₂O for $\text{pH} > 1$, only BV-OH is considered in the following Hammett study.



Scheme 3.4 Gibbs free energy surfaces of PTO and MTO Baeyer-Villiger oxidation with H₂O as leaving group including aqueous solvation (BV-H₂O pathway, unit is in kcal/mol).

Analyzing the variation of electron density in PTO during the phenyl migration step using fragment Mulliken charges, we find that significant charge variation takes place only in the hydroxide leaving group and the migrating phenyl group (**Figure 3.1**). Along the intrinsic reaction coordinate (IRC), electron density accumulates on OH as indicated by its Mulliken charge which varies from 0.0 to -0.7 (as hydroxyl transforms to hydroxide). Charge leaves the phenyl group, as indicated by its Mulliken charge changing from -0.2 to 0.4. Thus Ph plays the role of nucleophile. This also suggests that the migration step should be accelerated when the *para*-position of Ph is substituted with a more electron-donating group.

We therefore replaced hydrogen at the *para*-position in PTO by various electron-withdrawing and electron-donating substituents (*p*-X-C₆H₄-ReO₃, X = CF₃, CH₃, OCH₃, OH, and NH₂). Indeed, we find that as X becomes more electron-donating, the migration barriers (the Gibbs free energy difference between hydrogen peroxide complexes and BV transition states) decrease from 14.4 (X = CF₃), 11.7 (H), 10.4 (CH₃), 9.8 (OCH₃), 9.6 (OH), to 8.4 (NH₂) kcal/mol (Table 1). Indeed we find a good correlation ($R^2 = 0.99$) between those barriers and the Hammett parameter of X (the dashed line in **Figure 3.2**). A similar trend is also observed in the analogous organic BV reaction²⁷ and in a recent computational study of BV insertion within Pt(II)-aryl complexes.²⁸

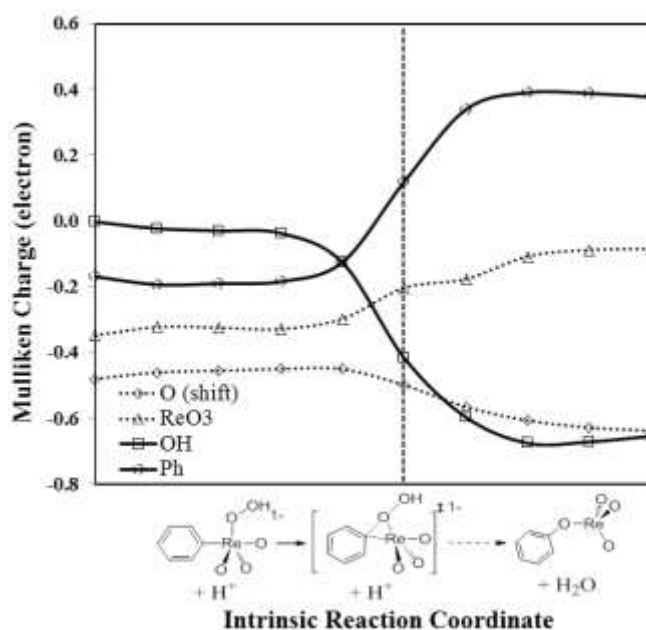


Figure 3.1 Variation of the fragment Mulliken charges along the BV intrinsic reaction coordinate based on M06/LACVP** level with solvent effect (the position of TS is marked by the vertical dashed line).

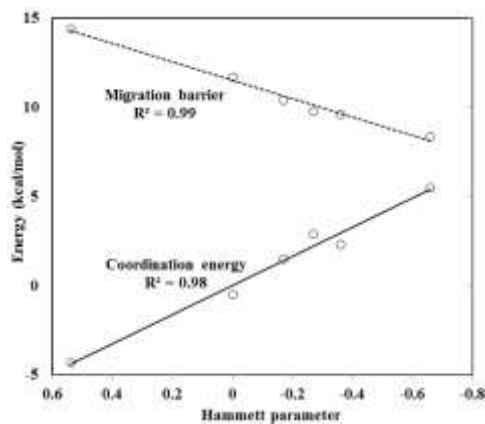


Figure 3.2 Correlations between the coordination energies and phenyl migration barrier to the Hammett's parameter of X, which is 0.54, 0.0, -0.17, -0.27, -0.36, and -0.66 for CF₃, H, CH₃, OCH₃, OH, and NH₂, respectively.

Table 3.1 Gibbs free energy surfaces of the BV oxidation of p - X -C₆H₄-ReO₃ (X = CF₃, CH₃, OCH₃, OH, and NH₂) by H₂O₂ at pH = 7 including aqueous solvation (kcal/mol).

X				
	0.0	-4.3	10.1	-80.6
CF ₃	0.0	-4.3	10.1	-80.6
H	0.0	-0.5	11.2	-79.3
CH ₃	0.0	1.5	11.9	-77.8
OCH ₃	0.0	2.9	12.7	-73.7
OH	0.0	2.3	11.9	-75.3
NH ₂	0.0	5.5	13.9	-73.5

An examination of the coordination energy shows that a more electron-donating X impedes the coordination of HOO⁻ to Re. The effect is large enough that the total BV barrier depends on the substituent in the opposite sense of the migration step alone. The coordination energy increases from -4.3, -0.5, 1.5, 2.9, 2.3, to 5.5 kcal/mol for X = CF₃, H, CH₃, OCH₃, OH, and NH₂, which correlate well ($R^2 = 0.98$) to the Hammett parameter of X (the solid line in **Figure 3.2**). The *para*-substituent also changes the identity of the ground state (at 1M H₂O₂): thus for X = CF₃ and H, the ground state is the hydrogen peroxide intermediate, but for X = CH₃, OCH₃, OH, and NH₂, it is the aryl rhenium trioxide.

The substituent effect leads to variations in the coordination energy (9.8 kcal/mol), which are even larger than for the migration barrier (6.0 kcal/mol). Because of

compensation by two opposing influences and the change of the ground state species, the overall BV reaction barriers (13.9, 11.9, 12.7, 11.9, 11.7, and 14.4 kcal/mol for $X = \text{CF}_3, \text{H}, \text{CH}_3, \text{OCH}_3, \text{OH}, \text{and NH}_2$, respectively) depend erratically on the p -substituent on phenyl with a poor correlation between the reaction rate and the Hammett parameter of X (Figure 3.3, black line).

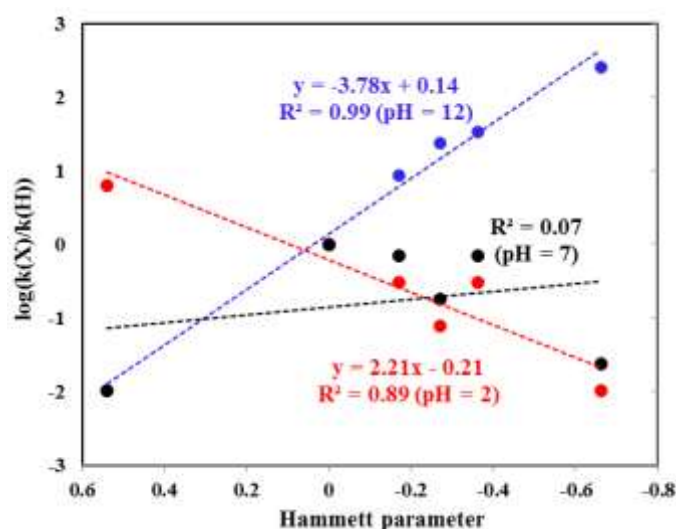
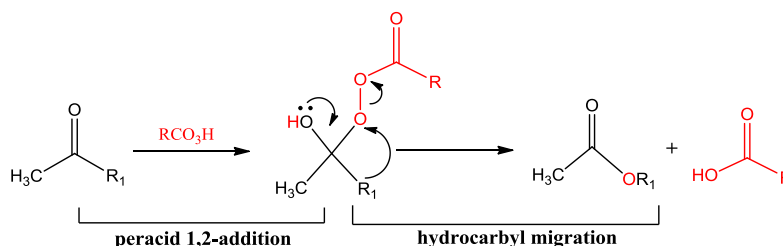


Figure 3.3 Correlations between the reaction rates at different pH to the Hammett's parameter of X .

This is contrary to the results for the analogous organic BV reaction, in which the substituent effect shows a very profound influence on the reaction rate. The BV oxidation of ketones by peracids in aprotic solvents can also be partitioned into two similar steps (**Scheme 3.5**): (1) 1,2-addition of peracid to the ketone forming a tetrahedral intermediate (Criegee intermediate), and (2) the migration of a hydrocarbyl group to oxygen with simultaneous loss of a carboxylic acid. Reyes *et al.* studied the p -substituent

effect on the oxidation of acetophenones by means of DFT.²⁹ They found that X substitution has a similar influence on the migration barrier as in the PTO system. However, for the 1,2-addition step, the substituent effect is insignificant. This is because a more electron-donating X, pushes electron density both to carbon (impeding the addition) and to the ketone oxo (increasing its basicity and therefore facilitating the addition step). The overall barrier depends only on the migration barrier, which is shown to decrease as X becomes more electron-donating.



Scheme 3.5 Organic Baeyer-Villiger reaction of ketone with a peracid.

Since changing acidity can change the coordination energy and the identity of the ground state species, the reaction rate (or overall barrier) can be tuned by solution pH value. At $\text{pH} = 12$ and 1M PTO and H_2O_2 , the hydrogen peroxide complexes are the ground states for all X substitutions with no penalty imposed for coordinating HOO^- to the aryl rhenium trioxide species. Thus, the overall barrier is determined only by the barrier of the migration step (our calculations show that it is more favorable to bind HOO^- than HO^- by 3.9 kcal/mol). As a result, the reaction rates are higher than those in $\text{pH} = 7$, and are inversely proportional to the Hammett parameters ($R^2 = 0.99$, blue line, **Figure 3.3**).

On the other hand, at low pH (pH = 2) or low reactant concentration, the ground state for all **X** groups is the arylrhenium trioxide species, and there is a larger penalty for deprotonating H₂O₂ as compared to that at pH = 7. This leads to a larger penalty for forming the hydroperoxide intermediates. Therefore, the influence of the coordination step outweighs that of migration and dominates the overall Gibbs free energy surface. As a result, the reaction rates are smaller than those at pH = 7 and are proportional to the Hammett parameter of **X**, showing that the reaction is decelerated when **X** becomes more electron-donating (red line, **Figure 3.3**).

3.3 Conclusions

In summary, we studied the BV-type oxidation of phenyl trioxorhenium by H₂O₂ in the aqueous phase. Our coupled-cluster calculations show that although the BV-type transition state contains some singlet diradical character (especially in the MTO case), its electronic structure is still well described by R-M06. We have investigated an alternate BV pathway in which H₂O instead of OH⁻ is the leaving group, and find that in the pH range of interest (pH > 1), the BV pathway with OH⁻ as the leaving group is lower in energy than one featuring simultaneous protonation of hydroxide for both PTO and MTO cases. Based on the fragment Mulliken charges, the organometallic BV oxidation occurs with the migrating phenyl acting as a nucleophile. Accordingly, substituting an electron-donating functional group in the *para*-position of phenyl lowers the migration barrier, similar to the organic analog. However, this substituent effect also pushes electron density to Re, impeding HOO⁻ coordination and slowing down the reaction. This is in contrast to the organic BV oxidation, in which *para*-substitution insignificantly

influences 1,2-addition of peracids. Due to the competition of the two opposite effects and the dependence of the resting state on pH and concentration, the reaction rate of this organometallic BV oxidation is does not correlate linearly on the Hammett parameters of the substituents.

The organometallic Baeyer-Villiger reaction poses a remarkably low barrier to insert oxygen into metal-carbon bonds (e.g., the calculated barrier for oxidizing Ph-ReO₃ to PhO-ReO₃ is only 11.7 kcal/mol). However, the disadvantage of this reaction is that if the substrate “M-R” has nonzero *d*-electrons, the oxidant may oxidize the metal rather than the metal-carbon bond; therefore, this reaction is not suitable for metal complexes with high-energy *d*-electrons. In two classes of M-R complexes this mechanism may play an important role. The first class is early transition metal complexes that have no *d*-electrons. However it is unlikely that species capable of activating C-H bonds can be catalytically regenerated after oxidation of those oxophilic metals. The second class is later transition metal complexes with very stable *d*-electrons. For example, the insertion of oxygen into palladium-aryl and nickel-aryl bonds is already known.³⁰⁻³² This class is more promising for integrating the OM-BV oxy-functionalization with alkane C-H activation, since late transition metals are known for activating alkane C-H bonds in oxidizing conditions.^{11,33,34} Therefore, we will focus on those systems in the future.

3.3 Computational Details

The geometry optimizations and zero-point vibrational energy (ZPVE) were carried out using the M06 functional^{35, 36} with the 6-31G**basis set^{37, 38} for all atoms except Re. For Re the first four shells of core electrons were described by the Los Alamos angular

momentum projected effective core potential (ECP) using the double- ζ contraction of valence functions³⁹ (denoted as LACVP**).

Solvation energies were calculated using the Poisson-Boltzmann self-consistent polarizable continuum method^{40, 41} implemented in Jaguar⁴² to represent water (dielectric constant = 80.37 and effective radius = 1.4 Å). The solvation calculations used the M06/LACVP** level of theory and the gas-phase optimized structures.

Singlet-point energy calculations were performed using the M06 functional with a larger basis set: here Re was described with the triple- ζ contraction of valence functions augmented with two f functions and the core electrons were described by the same ECP;⁴³ the other atoms were described with the 6-311++G** basis set.⁴⁴⁻⁴⁶

Unless otherwise noted, all energies discussed in this work are free energies, calculated as

$$G_{298K} = E_{\text{elec}} + G_{\text{solv}} + \text{ZPVE} + \sum_{\nu} \frac{h\nu}{e^{h\nu/kT} - 1} + \frac{n}{2}kT - T(S_{\text{vib}} + S_{\text{rot}} + S_{\text{trans}}),$$

where $n = 12$ accounts for the potential and kinetic energies of the translational and rotational modes and $T = 298$ K. The values of $(S_{\text{rot}} + S_{\text{trans}})$ for each Re intermediate were assumed to cancel.

The free energy of $\text{H}_2\text{O}_2(\text{aq})$, $\text{HOO}^-(\text{aq})$, and $\text{H}^+(\text{aq})$ at $\text{pH} = 7$ were calculated by adding the computed ideal gas phase Gibbs free energy and the experimentally measured solvation free energy $\Delta G(1\text{atm} \rightarrow 1\text{M})$ ^{47, 48} and correcting for concentration via $G = G^\circ + kT\ln(C/C^\circ)$.

3.5 Notes and references

1. S. N. Brown and J. M. Mayer, *J. Am. Chem. Soc.*, 1996, **118**, 12119-12133.
2. B. L. Conley, S. K. Ganesh, J. M. Gonzales, W. J. Tenn, K. J. H. Young, J. Oxgaard, W. A. Goddard and R. A. Periana, *J. Am. Chem. Soc.*, 2006, **128**, 9018-9019.
3. B. L. Conley, S. K. Ganesh, J. M. Gonzales, D. H. Ess, R. J. Nielsen, V. R. Ziatdinov, J. Oxgaard, W. A. Goddard and R. A. Periana, *Angew. Chem. Int. Edit.*, 2008, **47**, 7849-7852.
4. S. M. Bischof, M. J. Cheng, R. J. Nielsen, T. B. Gunnoe, W. A. Goddard and R. A. Periana, *Organometallics*, 2011, **30**, 2079-2082.
5. W. T. Reichle and W. L. Carrick, *J. Organomet. Chem.*, 1970, **24**, 419.
6. R. A. Periana, G. Bhalla, W. J. Tenn, K. J. H. Young, X. Y. Liu, O. Mironov, C. J. Jones and V. R. Ziatdinov, *J. Mol. Catal. A Chem.*, 2004, **220**, 7-25.
7. M. Lersch and M. Tilset, *Chem. Rev.*, 2005, **105**, 2471-2526.
8. J. F. Hartwig, *Acc. Chem. Res.*, 1998, **31**, 852-860.
9. J. M. Gonzales, R. Distasio, R. A. Periana, W. A. Goddard and J. Oxgaard, *J. Am. Chem. Soc.*, 2007, **129**, 15794-15804.
10. All energies discussed here are Gibbs free energies from M06/LACV3P++**//LACVP** level of theory.
11. R. A. Periana, D. J. Taube, S. Gamble, H. Taube, T. Satoh and H. Fujii, *Science*, 1998, **280**, 560-564.
12. C. J. Jones, D. Taube, V. R. Ziatdinov, R. A. Periana, R. J. Nielsen, J. Oxgaard and W. A. Goddard, *Angew. Chem. Int. Edit.*, 2004, **43**, 4626-4629.
13. B. G. Hashiguchi, K. J. H. Young, M. Yousufuddin, W. A. Goddard and R. A. Periana, *J. Am. Chem. Soc.*, 2010, **132**, 12542-12545.

14. A. Hofmann, D. Jaganyi, O. Q. Munro, G. Liehr and R. van Eldik, *Inorg. Chem.*, 2003, **42**, 1688-1700.
15. M. Ahlquist, R. A. Periana and W. A. Goddard, *Chem. Commun.*, 2009, 2373-2375.
16. C. Hansch, A. Leo and R. W. Taft, *Chem. Rev.*, 1991, **91**, 165-195.
17. M. F. Hawthorne, W. D. Emmons and K. S. Mccallum, *J. Am. Chem. Soc.*, 1958, **80**, 6393-6398.
18. M. Stiles and R. P. Mayer, *J. Am. Chem. Soc.*, 1959, **81**, 1497-1503.
19. H. C. Brown and C. J. Kim, *J. Am. Chem. Soc.*, 1968, **90**, 2082.
20. K. Nakamura and Y. Osamura, *J. Am. Chem. Soc.*, 1993, **115**, 9112-9120.
21. K. Nakamura and Y. Osamura, *Tetrahedron Lett.*, 1990, **31**, 251-254.
22. M. J. Cheng, R. J. Nielsen, M. Ahlquist and W. A. Goddard, *Organometallics*, 2010, **29**, 2026-2033.
23. CCSD/LACVP** calculations are performed by Gamess package.
24. T. J. Lee and P. R. Taylor, *Int. J. Quantum. Chem.*, 1989, 199-207.
25. G. Laurency, F. Lukacs, R. Roulet, W. A. Herrmann and R. W. Fischer, *Organometallics*, 1996, **15**, 848-851.
26. M. M. AbuOmar, P. J. Hansen and J. H. Espenson, *J. Am. Chem. Soc.*, 1996, **118**, 4966-4974.
27. S. L. Friess and A. H. Soloway, *J. Am. Chem. Soc.*, 1951, **73**, 3968-3972.
28. T. M. Figg, T. R. Cundari and T. B. Gunnoe, *Organometallics*, 2011, 3779-3785.
29. L. Reyes, J. R. Alvarez-Idaboy and N. Mora-Diez, *J. Phys. Org. Chem.*, 2009, **22**, 643-649.
30. D. Bandyopadhyay and K. Kamaraj, *Organometallics*, 1999, **18**, 438-446.

31. P. L. Alsters, H. T. Teunissen, J. Boersma, A. L. Spek and G. Vankoten, *Organometallics*, 1993, **12**, 4691-4696.
32. K. M. Koo, G. L. Hillhouse and A. L. Rheingold, *Organometallics*, 1995, **14**, 456-460.
33. A. E. Shilov and G. B. Shul'pin, *Chem. Rev.*, 1997, **97**, 2879-2932.
34. S. S. Stahl, J. A. Labinger and J. E. Bercaw, *Angew. Chem. Int. Edit.*, 1998, **37**, 2181-2192.
35. Y. Zhao and D. G. Truhlar, *Acc. Chem. Res.*, 2008, **41**, 157-167.
36. Y. Zhao and D. G. Truhlar, *Theor. Chem. Acc.*, 2008, **120**, 215-241.
37. W. J. Hehre, Ditchfie.R and J. A. Pople, *J. Chem. Phys.*, 1972, **56**, 2257-2261.
38. M. M. Francl, W. J. Pietro, W. J. Hehre, J. S. Binkley, M. S. Gordon, D. J. Defrees and J. A. Pople, *J. Chem. Phys.*, 1982, **77**, 3654-3665.
39. P. J. Hay and W. R. Wadt, *J. Chem. Phys.*, 1985, **82**, 299-310.
40. D. J. Tannor, B. Marten, R. Murphy, R. A. Friesner, D. Sitkoff, A. Nicholls, M. Ringnalda, W. A. Goddard and B. Honig, *J. Am. Chem. Soc.*, 1994, **116**, 11875-11882.
41. B. Marten, K. Kim, C. Cortis, R. A. Friesner, R. B. Murphy, M. N. Ringnalda, D. Sitkoff and B. Honig, *J. Phys. Chem.*, 1996, **100**, 11775-11788.
42. I. P. *Jaguar 7.6*; Schrodinger, OR, 2009.
43. J. M. L. Martin and A. Sundermann, *J. Chem. Phys.*, 2001, **114**, 3408-3420.
44. A. D. Mclean and G. S. Chandler, *J. Chem. Phys.*, 1980, **72**, 5639-5648.
45. T. Clark, J. Chandrasekhar, G. W. Spitznagel and P. V. Schleyer, *J. Comput. Chem.*, 1983, **4**, 294-301.
46. M. J. Frisch, J. A. Pople and J. S. Binkley, *J. Chem. Phys.*, 1984, **80**, 3265-3269.

47. M. D. Tissandier, K. A. Cowen, W. Y. Feng, E. Gundlach, M. H. Cohen, A. D. Earhart, T. R. Tuttle and J. V. Coe, *J. Phys. Chem. A*, 1998, **102**, 9308-9308.
48. D. D. Wagman, W. H. Evans, V. B. Parker, R. H. Schumm, I. Halow, S. M. Bailey, K. L. Churney and R. L. Nuttall, *J. Phys. Chem. Ref. Data*, 1982, **11**, 1-392.

CARBON-OXYGEN BOND-FORMING MECHANISMS IN RHENIUM OXO-ALKYL COMPLEXES

4.1 Introduction

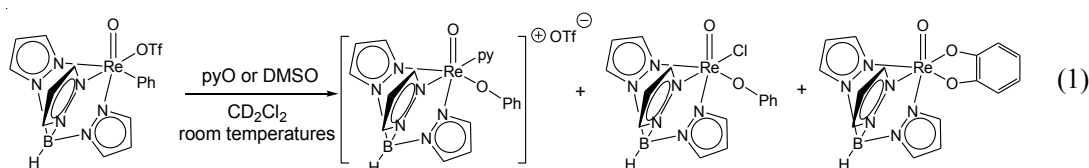
Our interest in the functionalization of alkyl groups generated through activation of alkanes by less electronegative metals led us to study the free energy surfaces of the carbon-heteroatom bond-forming mechanisms observed by Mayer *et al.*^{1,2} Other than reductive elimination and nucleophilic attack (typical of later, electrophilic transition metals), there are few known radical-free, highly selective mechanisms for the conversion of metal alkyls M-R to metal alkoxides M-OR^{1,3-5} Four mechanisms for C-X bond formation were observed by Mayer *et al.* in the oxidations of (HBpz₃)ReO(R)(OTf) [HBpz₃ = hydrotris(1-pyrazolyl)borate; R = Ph, Et; OTf = OSO₂CF₃]:

- aryl 1,2-migration across a metal-oxo bond (X = O)¹
- nucleophilic attack on an alkylidene carbon (X = N or S)²
- oxidation of an alkylidene carbon (X = O)²
- alkylidene coupling to form olefins (X = C)²

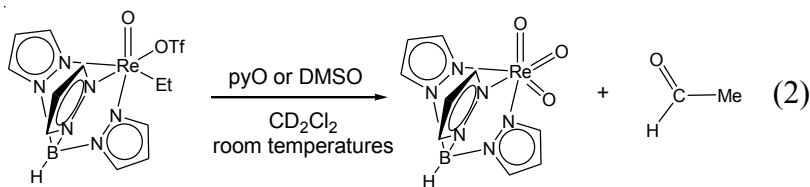
The first three are considered in this work.

The first thermal aryl 1,2-migration across a metal-oxo bond was reported by Brown and Mayer in the oxidation of (HBpz₃)ReO(Ph)(OTf) by oxygen atom donors dimethyl sulfoxide (DMSO) or pyridine *N*-oxide (pyO) (eq 1).¹ Mechanistic studies showed that the rhenium(V) species (HBpz₃)ReO(Ph)(OTf) is first oxidized to a more reactive

rhenium(VII) dioxo intermediate, $[(\text{HBpz}_3)\text{ReO}_2(\text{Ph})]\text{OTf}$, which is then converted to phenoxide complexes $[(\text{HBpz}_3)\text{ReO}(\text{OPh})(\text{py})]\text{OTf}$, $(\text{HBpz}_3)\text{ReO}(\text{OPh})(\text{Cl})$, and $(\text{HBpz}_3)\text{ReO}(\text{O}_2\text{C}_6\text{H}_4)$, through a 1,2-migration of the phenyl group. This migration suggests a new avenue for functionalizing alkyls to alkoxides.



However, when phenyl is replaced by an ethyl group, the oxidation leads to more complicated reaction mechanisms forming acetaldehyde and $(\text{HBpz}_3)\text{ReO}_3$ (eq 2).² Experiments show that $(\text{HBpz}_3)\text{ReO}(\text{Et})(\text{OTf})$ is first oxidized to $[(\text{HBpz}_3)\text{ReO}_2(\text{Et})]\text{OTf}$, similar to the phenyl case.² Instead of an ethyl 1,2-migration, it was suggested that the next step is α -hydrogen abstraction by the oxo group, yielding the ethylidene complex $[(\text{HBpz}_3)\text{ReO}(\text{OH})(\text{CHCH}_3)]\text{OTf}$.² The dimethyl sulfide (DMS) or pyridine (py) adduct of this intermediate has been observed by NMR. Further oxidation of the ethylidene species gives acetaldehyde.



We studied the free energy surfaces of $(\text{HBpz}_3)\text{ReO}(\text{R})(\text{OTf})$ ($\text{R}=\text{Me}$, Et , and $i\text{Pr}$) oxidations by DMSO using DFT and the PBF polarizable continuum solvation model.

We consider the selectivity between alkyl migration and alkylidene forming mechanisms as a function of hydrocarbyl group. We also investigate a mechanism not yet observed experimentally: nucleophilic attack on an alkylidene by water or ammonia followed by protonolysis to generate an alcohol or amine.

4.2 Computational Details

The geometry optimizations and zero-point vibrational energy (ZPVE) were carried out using the B3LYP functional⁶⁻⁸ with the 6-31G**basis set^{9,10} for all atoms except Re. For Re the first four shells of core electrons were described by the Los Alamos angular momentum projected effective core potential (ECP) using the double- ζ contraction of valence functions¹¹ (denoted as LACVP**).

Solvation energies were calculated using the Poisson-Boltzmann self-consistent polarizable continuum method^{12,13} implemented in Jaguar¹⁴ to represent dichloromethane (dielectric constant = 8.93 and effective radius = 2.33 Å). The solvation calculations used the B3LYP/LACVP** level of theory and the gas-phase optimized structures.

Recent calculations¹⁵ have established that M06 leads to activation energies a few kcal/mol more accurate than B3LYP. As a result, singlet-point energy calculations were performed using the M06 functional^{15,16} with a larger basis set: here Re was described with the triple- ζ contraction of valence functions augmented with two f functions¹⁷ and the core electrons were described by the same ECP; S was described using the 6-311++G(3df-3pd) basis;¹⁸⁻²⁰ the other atoms were described with the 6-311++G** basis set.^{19,21}

Unless otherwise noted, all energies discussed in this work are free energies, calculated

as

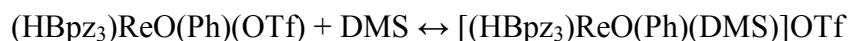
$$G_{298K} = E_{\text{elec}} + G_{\text{solv}} + \text{ZPVE} + \sum_{\nu} \frac{h\nu}{e^{h\nu/kT} - 1} + \frac{n}{2}kT - T(S_{\text{vib}} + S_{\text{rot}} + S_{\text{trans}}),$$

where $n = 12$ accounts for the potential and kinetic energies of the translational and rotational modes and $T = 298\text{K}$. The value of $(S_{\text{rot}} + S_{\text{trans}}) = 47.4$ e.u. for DMSO was chosen by fitting our calculated ΔS for the reaction $(\text{HBpz}_3)\text{ReO}(\text{Ph})(\text{OTf}) + \text{DMSO} \rightarrow [(\text{HBpz}_3)\text{ReO}(\text{Ph})(\text{DMSO})]\text{OTf}$ to the value measured by Mayer *et al.* ($\Delta S = -24.8$ kcal/mol).¹ The values of $(S_{\text{rot}} + S_{\text{trans}})$ for each Re intermediate were assumed to cancel.

4.3 Results and Discussion

We chose $[(\text{HBpz}_3)\text{ReO}_2(\text{R})]\text{OTf}$ as the reference point for the free energy surfaces, since these Re(VII) dioxo complexes are the common intermediates for both $(\text{HBpz}_3)\text{ReO}(\text{Et})(\text{OTf})$ and $(\text{HBpz}_3)\text{ReO}(\text{Ph})(\text{OTf})$ oxidation reactions.^{1,2} In particular, for $\text{R} = \text{Ph}$ NMR experiments showed that $[(\text{HBpz}_3)\text{ReO}_2(\text{Ph})]\text{OTf}$ (deep orange color) is the resting state, as $(\text{HBpz}_3)\text{ReO}(\text{Ph})(\text{OTf})$ reacts with pyO at -78 °C.¹

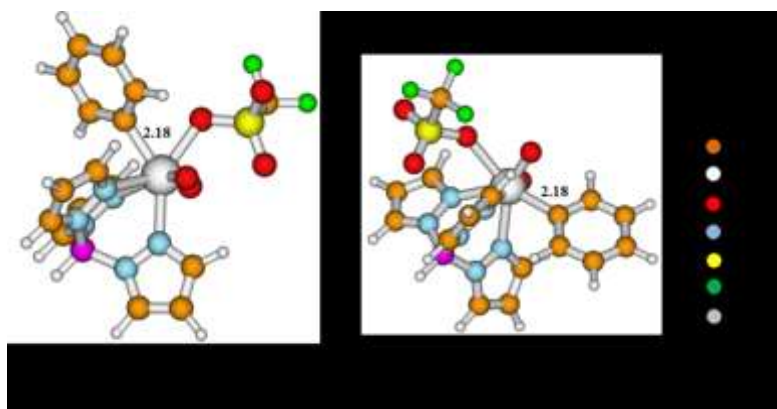
The measured equilibrium constant of



in the presence of 10-fold excess DMS depends linearly on the concentration of $(\text{HBpz}_3)\text{ReO}(\text{Ph})(\text{OTf})$,¹ indicating that dissociation of the ion-pair is unlikely. Therefore we consider that the triflate counterion remains associated in the second coordination sphere of rhenium throughout the reactions.

Our DFT calculations show that seven-coordinate $(\text{HBpz}_3)\text{ReO}_2(\text{Ph})(\text{OTf})$

intermediates formed from the $[(\text{HBpz}_3)\text{ReO}_2(\text{Ph})]\text{OTf}$ ion-pair are unstable, and therefore not involved in the reaction mechanism. Two isomers were located for this type of intermediate. The first one (A, **Scheme 4.1**) has triflate *cis* to the phenyl group, while in the other (B) the two ligands are in *trans* positions. These isomers, however, are higher in free energy than the ion-pair complex by 15.9 and 6.0 kcal/mol, respectively.



Scheme 4.1

Phenyl 1,2-Migration We first studied the phenyl 1,2-migration of $[(\text{HBpz}_3)\text{ReO}_2(\text{Ph})]\text{OTf}$ (**1-Ph**, **Figure 4.1**) to benchmark the DFT performance in these Re systems, since the potential energy surface is well established experimentally.¹ M06 predicts the barrier to be $\Delta G^\ddagger = 17.9$, in good agreement with the value determined by the Eyring plot in experiments ($\Delta G^\ddagger = 20.9$ kcal/mol).¹

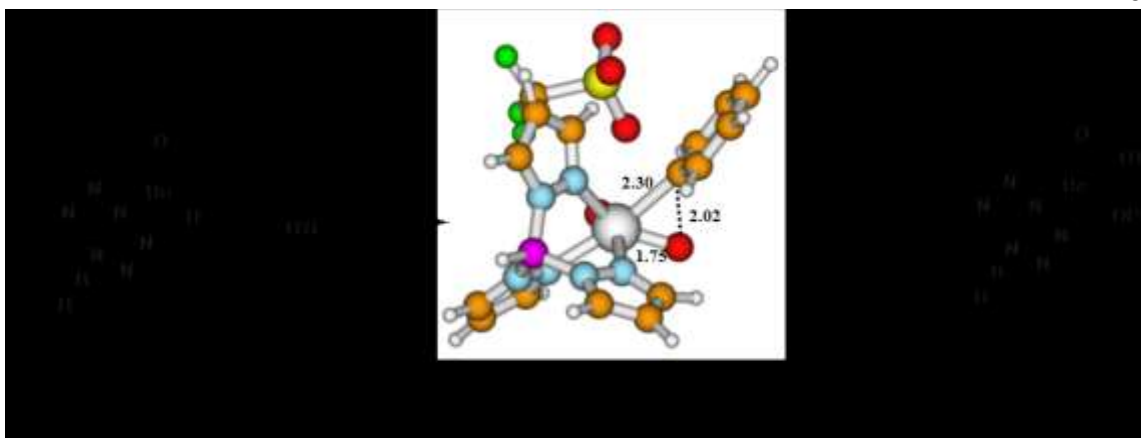


Figure 4.1 Free energy surface of Ph 1,2-migration (kcal/mol) at 298K.

The migration product **2-Ph**, is 38.0 kcal/mol more stable than the dioxo species, indicating an irreversible process, consistent with experiments.¹ For the reaction $\text{DMS}_{(\text{g})} (1 \text{ atm}) + 0.5 \text{ O}_{2(\text{g})} (1 \text{ atm}) \rightarrow \text{DMSO}_{(\text{g})} (1 \text{ atm})$, our M06 calculations predict ΔH to be -27.8 kcal/mol, in good agreement with the experimental data $\Delta H = -27.0$ kcal/mol.²² These results suggest that the current functional and basis set combination are able to capture the correct free energy surfaces in this system.

Ethyl Activation in the Reaction of $[(\text{HBpz}_3)\text{ReO}_2(\text{C}_2\text{H}_5)]\text{OTf} + \text{DMSO}$

Ethyl 1,2-Migration We considered several possible pathways for activating the ethyl ligand: (1) Ethyl 1,2-migration, (2) α - and β -hydrogen abstraction by oxo, and (3) α - and β -hydrogen abstraction by external base.

The ethyl 1,2-migration was ruled out experimentally through the direct synthesis of $(\text{HBpz}_3)\text{ReO}(\text{OEt})\text{OTf}$ (the expected product of the ethyl 1,2-migration of $(\text{HBpz}_3)\text{ReO}(\text{Et})\text{OTf}$) and its reaction with pyO.² DuMez and Mayer found that this

oxidation reaction produced both acetaldehyde and ethanol, in contrast to the (HBpz₃)ReO(Et)OTf oxidation, which generates only acetaldehyde.²

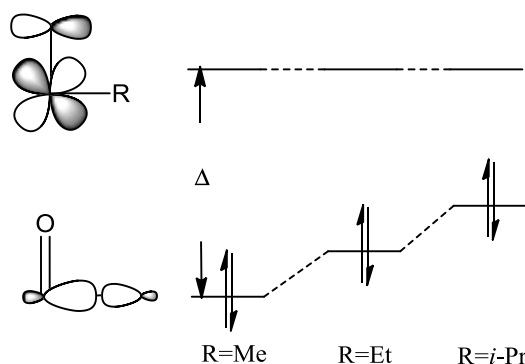
Surprisingly the calculated reaction barrier of this migration is 22.1 kcal/mol (**Table 4.1**), only slightly higher (by 4.2 kcal/mol) than that of the phenyl case. This suggests that the reason the ethyl case does not lead to ethoxide is because a more facile pathway exists, rather than because the 1,2-migration is energetically unfavorable.

Table 4.1 The reaction barrier and energy for alkyl 1,2-migration at 298K (unit: kcal/mol).

Alkyl			
Me	0.0 (0.0)	29.1 (31.8)	-26.1 (-4.4)
Et	0.0 (0.0)	22.1 (27.0)	-25.0 (-8.6)
<i>i</i> Pr	0.0 (0.0)	11.8 (15.2)	-28.4 (-11.9)

From a molecular orbital point of view, this migration is dominated by the interaction between two molecular orbitals in the Re dioxo species, the occupied Re-C σ orbital and unoccupied Re-O π^* orbital (**Scheme 4.2**). The larger the energy difference (Δ) between the two orbitals, the larger will be the migration barrier, and *vice versa*. Δ can be manipulated by substituting different alkyl ligands to vary the Re-C σ orbital energy, since the Re-O π^* orbital is unaffected by this substitution. We calculate Δ to be 5.67 (Me), 4.35 (Et), and 4.23 eV (*i*Pr), suggesting that the migration barrier for the three alkyl groups would be Me > Et > *i*Pr. Indeed, our calculations show that replacing ethyl by an electron-poorer ligand Me increases the barrier from 22.1 to 29.1 kcal/mol; while substituting by an electron-rich ligand *i*Pr lowers the barrier to only 11.8 kcal/mol. This tendency holds when the triflate anion is not included in calculations (barriers of 31.8,

27.0, and 15.2 kcal/mol for Me, Et, and *i*Pr respectively, see the numbers in parentheses in **Table 4.1**), indicating that it is the nature of the alkyl group and not an interaction with triflate that controls the alkyl 1,2-migration barrier.



Scheme 4.2

It is clear the oxo is electrophilic during the migration since the more nucleophilic alkyls yield lower reaction barriers. This result is consistent with experiments by Mayer and coworkers, showing that the Re dioxo species oxidizes electron-rich Me₂S much faster than Me₂SO.¹

α- and β-Hydrogen Abstraction by Oxo DuMez *et al.* proposed that instead of an ethyl 1,2-migration, the ethyl is activated through α-hydrogen abstraction by the oxo ligand to form an ethylidene species, which is then trapped by DMS and observed by NMR at -70 °C.² However, we calculate the barrier of this reaction to be 44.9 kcal/mol, far too high for a thermal reaction (**Figure 4.2 (a)**). Including a tunneling contribution estimated with Skodje and Truhlar's approximation²³ for a thermally averaged

transmission coefficient through a 1-D parabolic barrier, transition state theory predicts a flux through this barrier orders of magnitude slower than the observed rate.

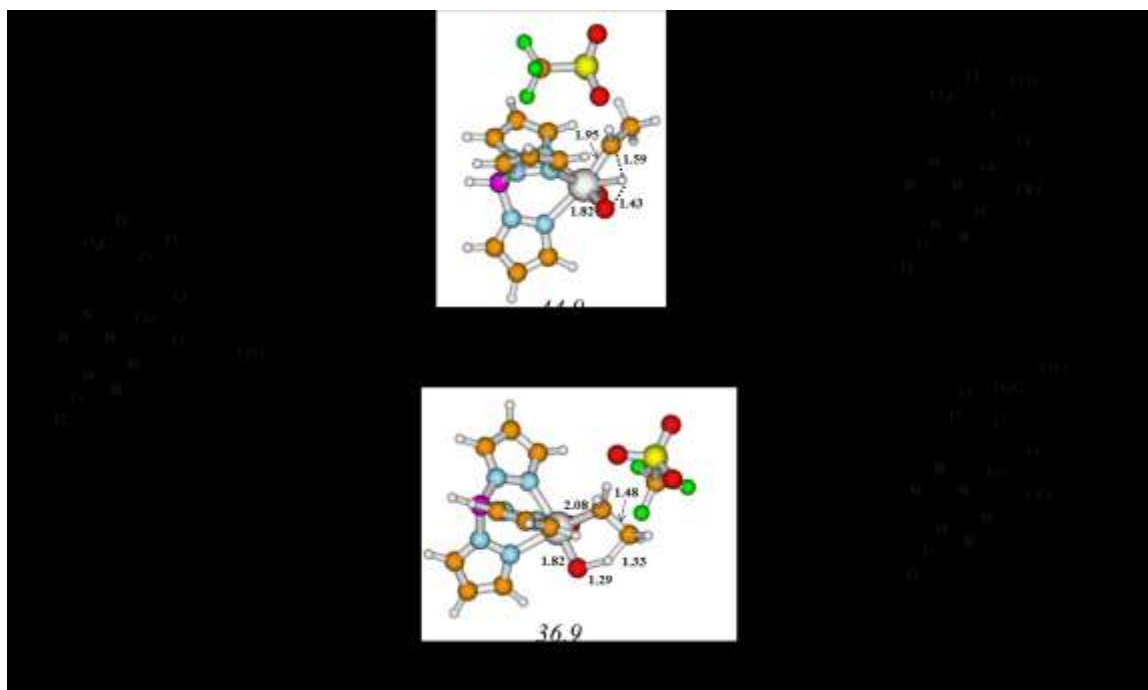
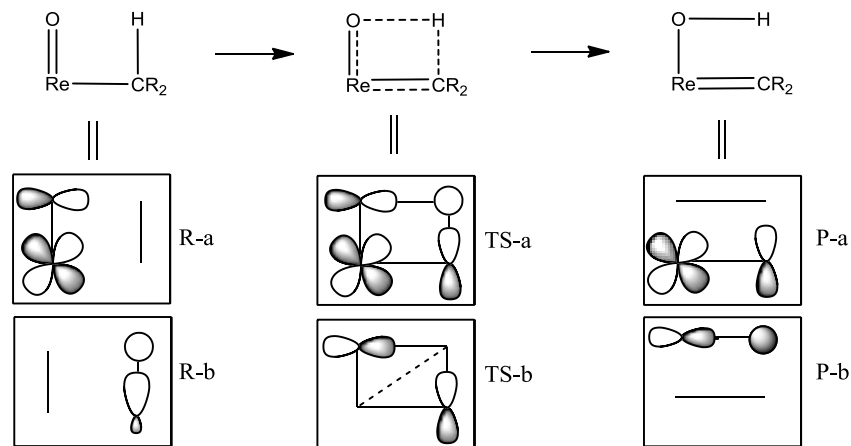


Figure 4.2 Free energy surface of α - and β -hydrogen abstraction by oxo (kcal/mol) at 298K.

This high barrier may be interpreted through molecular orbitals. During the reaction, one Re-O π (R-a) and one C-H σ (R-b) bond are converted to one Re-C π (P-a) and O-H σ (P-b) bonds (**Scheme 4.3**). In order to have a low reaction barrier, the two molecular orbitals must remain bonding and orthogonal in the transition state. No two such linear combinations can be formed from the four relevant atomic orbitals, so significant ionic character is imposed on the wavefunction. Since one pair of electrons must pass through

a node (TS-b) in the transition state, the reaction is “2+2 forbidden” with a high barrier.²⁴



Scheme 4.3

We also considered β -hydrogen abstraction by the oxo ligand to form ethylene (**Figure 4.2 (b)**). The calculated barrier is 36.9 kcal/mol, more favorable than that of the α -hydrogen abstraction by 8.0 kcal/mol but much higher than the 22.1 kcal/mol for ethyl 1,2-migration. Certainly, such an activation barrier precludes this reaction at room temperatures.

Hydrogen Abstraction by OTf Since the ethyl 1,2-migration pathway has been ruled out experimentally² and the hydrogen abstractions by oxo has been ruled out theoretically, there must be another lower barrier pathway. Several bases in the solution might be capable of abstracting protons from ethyl, including OTf, DMS, or pyridine, by-products of the initial oxidation.

Our calculations show that the α -hydrogen abstraction by OTf has a barrier of only 12.0 kcal/mol (**Figure 4.3 (a)**), representing the lowest pathway for activating the ethyl

group. This low barrier may be attributed to the high oxidation state of $[(\text{HBpz}_3)\text{ReO}_2(\text{Et})]\text{OTf}$, in which the formally empty $5d$ orbitals are capable of accommodating the new π -bonding electrons after proton transfer without raising the Coulomb repulsion.

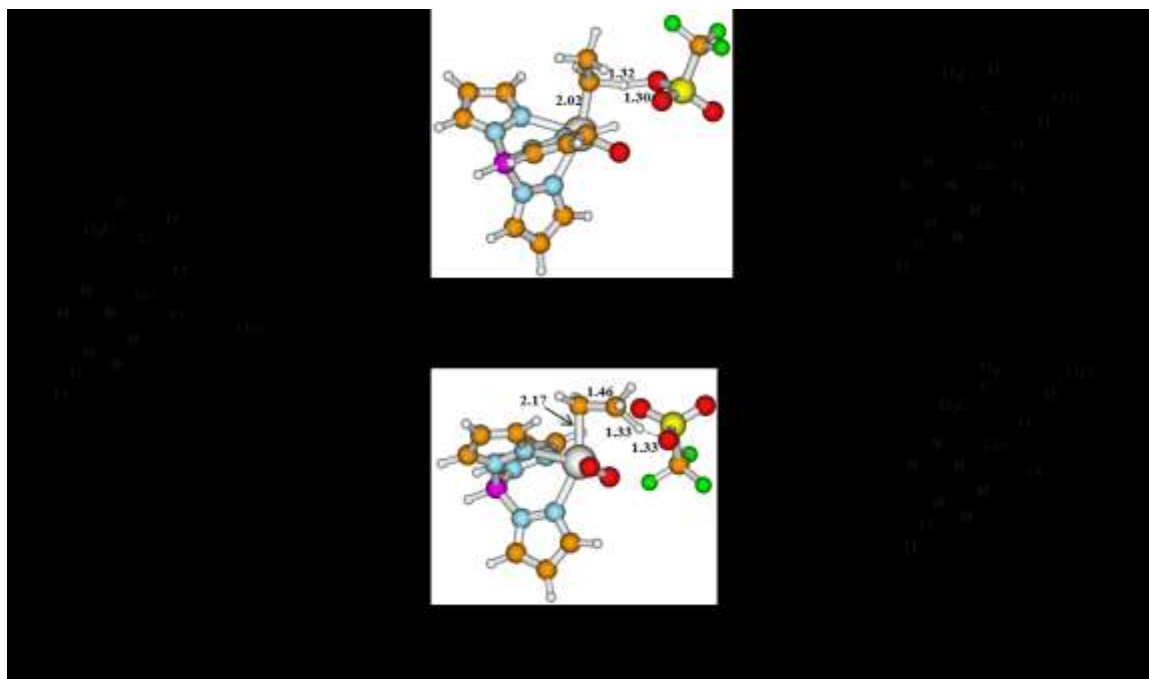


Figure 4.3 Free energy surface of α - and β -hydrogen abstraction by external base, OTf (kcal/mol) at 298K.

The product of this abstraction, $[(\text{HBpz}_3)\text{ReO}_2(\text{CHCH}_3)]\text{HOTf}$ (**5**), is only a local minimum on the potential energy surface. Taking ZPVE and thermal corrections into account, there is no barrier to the subsequent exothermic transfer of the proton to an oxo group, forming $[(\text{HBpz}_3)\text{ReO}(\text{OH})(\text{CHCH}_3)]\text{OTf}$ (**6**). The catalytic effect of a base, even as weak as triflate, allows the stepwise transfer of the proton to proceed essentially

through the forbidden 2+2 pathway by stabilizing the ionized proton during transit.

Transfer of the proton from OTf to oxo is essential for the formation of the DMS adducts observed experimentally by NMR spectroscopy.² Our calculations show that without this proton transfer, the DMS adduct, $(\text{HBpz}_3)\text{ReO}_2(\text{CH}(\text{DMS})\text{CH}_3)$, is 19.0 kcal/mol uphill compared with $\text{DMS} + (\text{HBpz}_3)\text{ReO}_2(\text{CHCH}_3)$. On the other hand, the DMS adduct, $(\text{HBpz}_3)\text{ReO}(\text{OH})(\text{CH}(\text{DMS})\text{CH}_3)^{+1}$, is 7.2 kcal/mol more stable than $\text{DMS} + (\text{HBpz}_3)\text{ReO}(\text{OH})(\text{CHCH}_3)^{+1}$ after the proton transfer. This result is not surprising, since the rhenium atom becomes more electron-deficient after proton transfer to oxo and therefore is more capable of accommodating the lone pair electrons formed after the attack of DMS on the methyne carbon.

Variations in the alkyl ligand are expected to have an insignificant influence on this barrier, since the acidity of the α -hydrogen is primarily dependent on whether the $5d$ orbital is empty. Thus, our calculations show that replacing Et by Me and *i*Pr groups gives barriers of 12.0 and 13.5 kcal/mol, respectively.

If a $[(\text{HBpz}_3)\text{ReO}_2(\text{Et})]^+\text{X}^-$ analogue could be synthesized with a noncoordinating anion that is less basic than triflate (e.g., $[\text{BAr}^{\text{F}}_4]^-$), the ethyl migration pathway may become dominant. However, pyridine or DMS released during the oxidation by pyO or DMSO would catalyze the proton transfer reaction at a rate proportional to its concentration.

Abstracting the β -hydrogen to form an ethylene-coordinated Re compound (**7**) leads to a barrier of 25.5 kcal/mol, suggesting that the β -hydrogen is less reactive than α -hydrogen (**Figure 4.3** (b)).

Dependence of Activation Pathway on Alkyl Our calculations suggest that replacement of the Et group by *i*Pr may change the reaction mechanism significantly. The barrier of the alkyl 1,2-migration is decreased from 22.1 kcal/mol to 11.8 kcal/mol due to the increased nucleophilicity, while the barrier for the α -hydrogen abstraction by triflate is 13.5 kcal/mol, almost the same as for the Et case (12.0 kcal/mol). Additionally, the product of the migration is at -28.4 kcal/mol, more stable than that of the triflate abstraction pathway by 13.1 kcal/mol. Both kinetics and thermodynamics favor the migration over the abstraction pathway.

In contrast, replacement of Et by Me would make the abstraction pathway even more favorable by suppressing the alkyl 1,2-migration pathway, since the barrier of migration is increased to 29.1 kcal/mol due to lesser nucleophilicity of Me. This indicates that in the presence of any base, the 1,2-migration pathway will not be an option for the selective functionalization of the methyl group to methoxide.

Acetaldehyde Formation in the Reaction of [(HBpz₃)ReO₂(C₂H₅)]OTf + DMSO

Acetaldehyde Formation through Oxo-Ethylidene Coupling In the next step, the ethylidene is oxidized to form acetaldehyde. This can be achieved through the coupling of ethylidene and oxo ligands or through oxygen atom transfer from the oxidant, DMSO to the methyne carbon. The calculated barrier of the ethylidene-oxo coupling is 46.0 kcal/mol (**Figure 4.4**). It is noteworthy that the proton is transferred back to triflate at the product **8**. This product has a C-O distance of 1.37 Å, comparable to a single bond (1.42) and much longer than the usual double bond (1.21 Å),²⁵ indicating that the newly formed

acetaldehyde is a covalently bound metallacycle and the oxidation state of rhenium is +5.

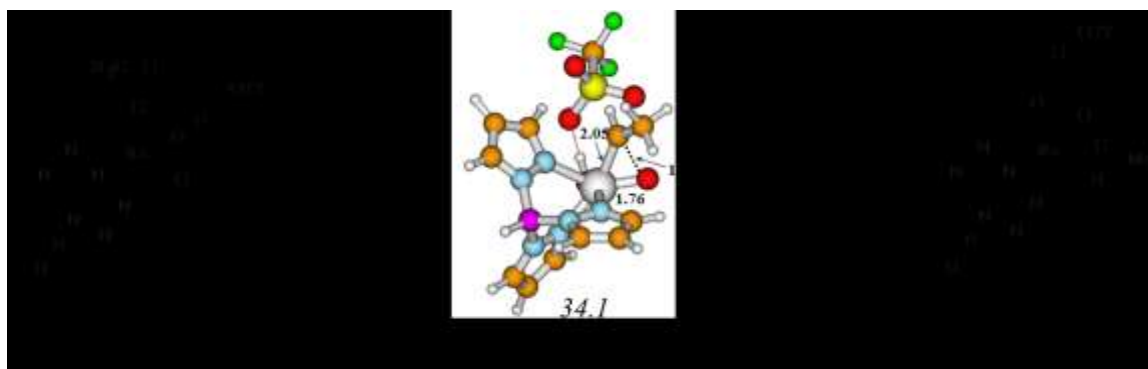


Figure 4.4 Free energy surface of the acetaldehyde formation through the oxo-ethylidene coupling pathway (kcal/mol) at 298K.

Acetaldehyde Formation through Oxygen Transfer from DMSO We find that the most energetically favorable pathway to form acetaldehyde is through the oxygen transfer from DMSO to the methyne carbon (**Figure 4.5**). After passing a barrier of 8.0 kcal/mol, DMSO is bound to the methyne carbon to form the adduct **9**, which is slightly exergonic (0.4 kcal/mol) relative to **6**. Finally the acetaldehyde is formed through the cleavage of the S-O bond with a barrier of 15.3 kcal/mol. The product of this dissociation, **10**, has a C-O bond distance of 1.26 Å (in the range of a normal C-O double bond) and the **Re-OCHCH₃** bond distance is 2.13 Å, suggesting that acetaldehyde is bound to Re through a weak dative interaction. The formal oxidation state of this Re is (V). Further oxidation will lead to (HBpz₃)ReO₃, the observed Re(VII) product.

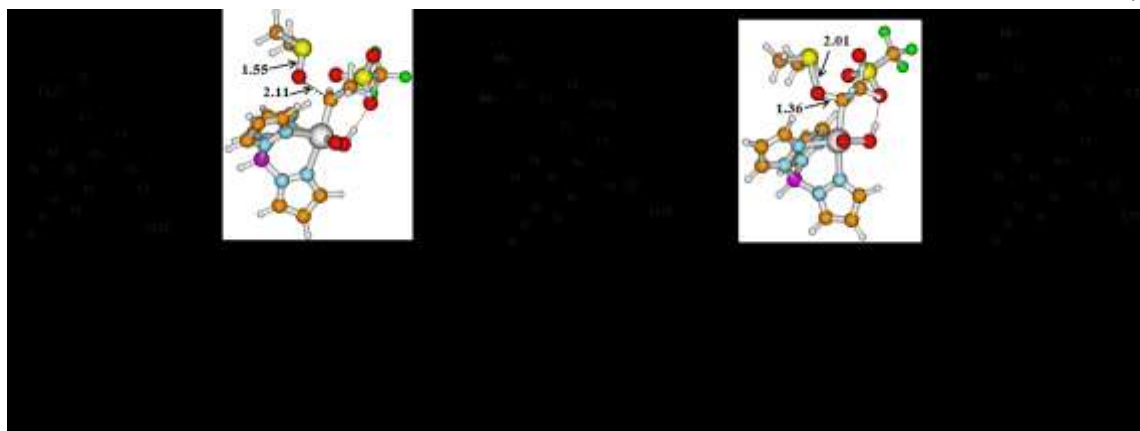


Figure 4.5 Free energy surfaces of the acetaldehyde formation through direct oxygen transfer from DMSO (kcal/mol) at 298K

Overall Free Energy Surface The overall free energy surface is shown in **Figure 4.6**. The ethyl ligand of **1** is activated through a α -hydrogen abstraction by triflate leading to **5** with a barrier of 12.0 kcal/mol. This barrier is 5.9 kcal/mol lower than the Ph 1,2-migration of (HBpz₃)ReO(Ph)(OTf) (17.9 kcal/mol), which may explain why no dioxo intermediate is observed following (HBpz₃)ReO(Et)(OTf).^{1,2} This is followed by a barrierless proton transfer leading to the formation of **6**. In next step, the adduct **9**, the most stable intermediate along the mechanism, is formed through the attack of DMSO on the methyne carbon with a barrier of 8.0 kcal/mol. Finally acetaldehyde is formed through the dissociation of DMS with a barrier of 15.3 kcal/mol. The rate-determining step is the dissociation of DMS (**9** \rightarrow **9,10-Ts**) with an overall barrier of 15.3 kcal/mol (compared with **9**) and the overall reaction energy is -37.2 kcal/mol. This potential energy surface is consistent with experimental results showing it is a low-temperature (-34 °C) and irreversible reaction.²

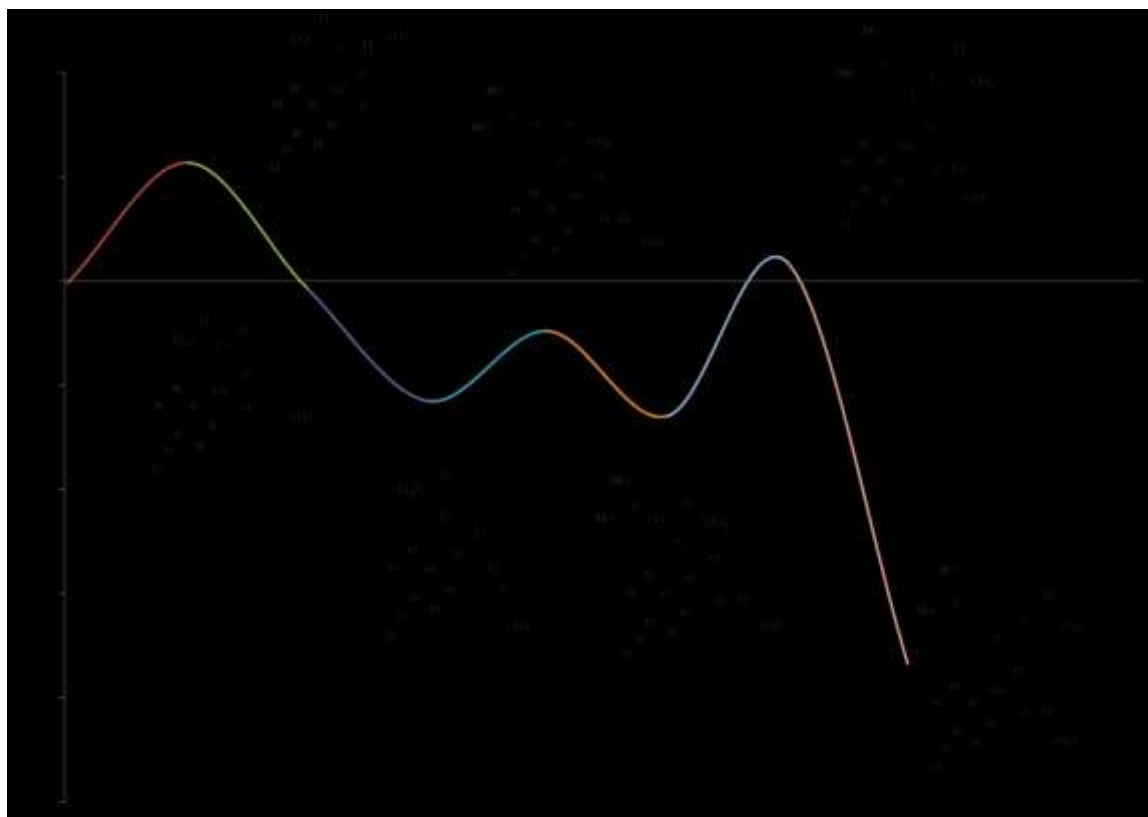


Figure 4.6 Overall free energy surface of the oxidation of (HBpz₃)ReO(Et)(OTf) by DMSO (kcal/mol) at 298K.

Alkylidene Nucleophilic attack and protonolysis Our calculations of free energy surfaces for methane activation by Group 7, 8 and 9 metals led us to consider that methylidene formation may be favored over oxidation mechanisms that leave a metal-bound methyl group intact. This possibility threatens to preclude selective 2-electron oxidations. However, a sequential nucleophilic attack at the sp^2 carbon of an alkylidene intermediate followed by protonolysis of the M-C bond may offer a new means of generating an alcohol (or other functionalized alkyl). The rhenium ethylidene in this

work was reversibly trapped by pyridine and dimethylsulfide forming C-N and C-S bonds,² and precedents for related alkylidene formation,²⁶ nucleophilic attack²⁷ and protonolysis²⁸ steps have been observed or suggested. Therefore, we used $(\text{HBpz}_3)\text{ReO}(\text{OH})(\text{CHCH}_3)^{+1}$ (**11**, **Figure 4.7**) as a representative of a Group 7 alkylidene and employed water and ammonia as simple protic nucleophiles to investigate the feasibility of this mechanism. In calculating thermodynamic properties, aqueous H_2O and NH_3 (1M) were taken as reference states.

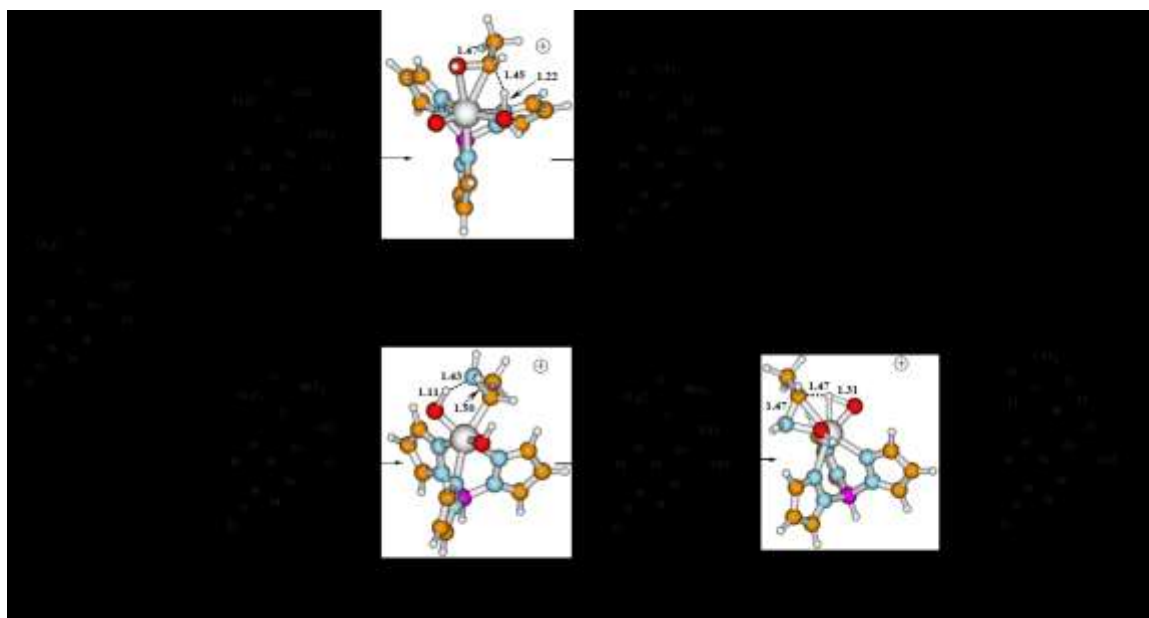


Figure 4.7 Free energy surface of the H_2O and NH_3 nucleophilic attack on $(\text{HBpz}_3)\text{ReO}(\text{OH})(\text{CHCH}_3)^{+1}$ (kcal/mol) at 298K.

We found that nucleophilic attack of H_2O on the α -carbon is barrierless and accompanied by proton transfer from H_2O to the hydroxide oxygen (**Figure 4.7 (a)**). The product **12** is 3.9 kcal/mol more stable than **11**. In the next step, a proton is transferred

from the rhenium-bound H₂O to the α -carbon atom, which yields the ethanol adduct

13. The barrier for this step is 36.9 kcal/mol, which is high even for alkane activation chemistry.

The nucleophilic attack by NH₃ resulted in the formation of (HBpz₃)ReO(OH)(C(NH₃)HCH₃)⁺¹ (**14**), which is more stable than **11** by 21.8 kcal/mol (Figure 7 (b)). In the sequent step, a proton migrates from the ammonium group to the oxo oxygen with a barrier of 36.8 kcal/mol to form **15** (2 kcal/mol uphill compared to **14**). Finally a bound ethylamine (**16**) is formed via protonolysis of the Re-C with a barrier of 42.4 kcal/mol. The overall reaction barrier is 44.4 kcal/mol, even higher than in the case of H₂O.

We conclude that for the current Re ethylidene complex, it is not kinetically possible to produce alcohol or amines through nucleophilic attack by H₂O or NH₃. Also, our free energy surface does not address additional concerns such as selectivity against further oxidations or solubility. We do note that each step from the ethyl complex **1** to the alcohol complex **13** is exothermic and without a thermodynamic sink, which is ideal for a catalyzed mechanism. The protonolysis reaction **12**→**13** is essentially the reverse of an alkane activation by Re(V). Known alkane activations catalyzed by late metals more commonly occur, in contrast, on low oxidation states with filled $d\pi$ orbitals. Such activation reactions have been computed to be endergonic by amounts similar to **13**→**12**.^{29,30} In this light one may expect the protonolysis barrier to be accessible on catalysts capable of alkane activation, and we will report on such cases separately.

4.4 Conclusions

The oxidation of $(\text{HBpz}_3)\text{ReO}(\text{Et})(\text{OTf})$ by DMSO to form acetaldehyde was studied using density functional theory. We find that the reaction begins via a facile α -hydrogen abstraction by external base with a reaction barrier of only 12.0 kcal/mol. This explains why the 1,2-migration to form an alkoxide is not observed as in $(\text{HBpz}_3)\text{ReO}(\text{Ph})(\text{OTf})$. On the other hand we find that the previously proposed ethyl activation step (α -hydrogen abstraction by oxo^2) is a 2+2 forbidden reaction with a barrier of 44.9 kcal/mol. The final step of forming acetaldehyde is an oxygen transfer from DMSO with a barrier of 15.3 kcal/mol, 31.1 kcal/mol lower than that of the oxo-carbene coupling. We find this to be the rate-determining step of the reaction mechanism.

We find that replacement of the alkyl group can alter the reaction pathway. Thus $\text{R} = i\text{Pr}$ makes the alkyl 1,2-migration kinetically more favorable (by 1.7 kcal/mol) than the α -hydrogen abstraction pathway, but only in the absence of bases. On the other hand, $\text{R} = \text{Me}$ makes the α -hydrogen abstraction (leading eventually to formaldehyde) more favorable by 17.1 kcal/mol, eliminating the migration mechanism as a means of generating methoxide.

In addition, we investigated the possibility of nucleophilic attack by H_2O or NH_3 on the ethylidene complex $((\text{HBpz}_3)\text{ReO}(\text{OH})(\text{CHCH}_3)^+)$ followed by protonolysis as a new means of converting a metal alkyl to an alcohol or amine. The barrier for the protonolysis step in both mechanisms is over 35 kcal/mol.

4.5 References

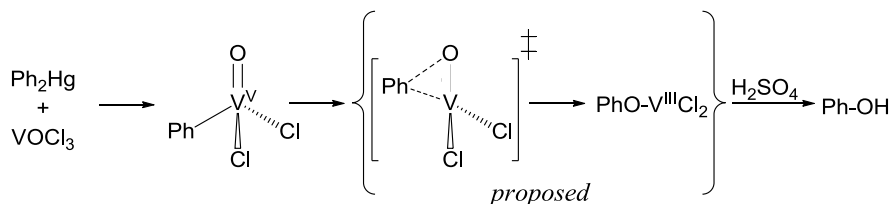
1. Brown, S. N.; Mayer, J. M. *J. Am. Chem. Soc.* **1996**, *118*, 12119.
2. DuMez, D. D.; Mayer, J. M. *J. Am. Chem. Soc.* **1996**, *118*, 12416.
3. Conley, B. L.; Ganesh, S. K.; Gonzales, J. M.; Ess, D. H.; Nielsen, R. J.; Ziatdinov, V. R.; Oxgaard, J.; Goddard, W. A.; Periana, R. A. *Angew. Chem. Int. Ed.* **2008**, *47*, 7849.
4. Conley, B. L.; Ganesh, S. K.; Gonzales, J. M.; Tenn, W. J.; Young, K. J. H.; Oxgaard, J.; Goddard, W. A.; Periana, R. A. *J. Am. Chem. Soc.* **2006**, *128*, 9018.
5. Tenn, W. J.; Conley, B. L.; Hovelmann, C. H.; Ahlquist, M.; Nielsen, R. J.; Ess, D. H.; Oxgaard, J.; Bischof, S. M.; Goddard, W. A.; Periana, R. A. *J. Am. Chem. Soc.* **2009**, *131*, 2466.
6. Becke, A. D. *Phys Rev A* **1988**, *38*, 3098.
7. Becke, A. D. *J Chem Phys* **1993**, *98*, 5648.
8. Lee, C. T.; Yang, W. T.; Parr, R. G. *Phys Rev B* **1988**, *37*, 785.
9. Hehre, W. J.; Ditchfie.R; Pople, J. A. *J. Chem. Phys.* **1972**, *56*, 2257.
10. Francl, M. M.; Pietro, W. J.; Hehre, W. J.; Binkley, J. S.; Gordon, M. S.; Defrees, D. J.; Pople, J. A. *J. Chem. Phys.* **1982**, *77*, 3654.
11. Hay, P. J.; Wadt, W. R. *J. Chem. Phys.* **1985**, *82*, 299.
12. Tannor, D. J.; Marten, B.; Murphy, R.; Friesner, R. A.; Sitkoff, D.; Nicholls, A.; Ringnalda, M.; Goddard, W. A.; Honig, B. *J. Am. Chem. Soc.* **1994**, *116*, 11875.
13. Marten, B.; Kim, K.; Cortis, C.; Friesner, R. A.; Murphy, R. B.; Ringnalda, M. N.; Sitkoff, D.; Honig, B. *J. Phys. Chem.* **1996**, *100*, 11775.
14. *Jaguar 7.0*; Schrodinger, I. P., OR, 2007.
15. Zhao, Y.; Truhlar, D. G. *Theor. Chem. Acc.* **2008**, *120*, 215.

16. Zhao, Y.; Truhlar, D. G. *Acc. Chem. Res.* **2008**, *41*, 157.
17. Martin, J. M. L.; Sundermann, A. *J. Chem. Phys.* **2001**, *114*, 3408.
18. Mclean, A. D.; Chandler, G. S. *J. Chem. Phys.* **1980**, *72*, 5639.
19. Clark, T.; Chandrasekhar, J.; Spitznagel, G. W.; Schleyer, P. V. *J. Comput. Chem.* **1983**, *4*, 294.
20. Frisch, M. J.; Pople, J. A.; Binkley, J. S. *J. Chem. Phys.* **1984**, *80*, 3265.
21. Krishnan, R.; Binkley, J. S.; Seeger, R.; Pople, J. A. *J. Chem. Phys.* **1980**, *72*, 650.
22. NIST Chemistry WebBook. <http://webbook.nist.gov/chemistry/> (accessed June 2.
23. Skodje, R. T.; Truhlar, D. G. *J. Phys. Chem.* **1981**, *85*, 624.
24. Goddard, W. A. *J. Am. Chem. Soc.* **1972**, *94*, 793.
25. Lide, D. R. *CRC Handbook of Chemistry and Physics*, 87 ed.; CRC Press/Taylor and Francis: Boca Raton, FL.
26. (a) Gusev, D. G.; Lough, A. J. *Organometallics* **2002**, *21*, 2601. (b) Castarlenas, R.; Esteruelas, M. A.; Oñate, E. *Organometallics* **2007**, *26*, 3082.
27. Gunnoe, T. B.; White, P. S.; Templeton, J. L.; Casarrubios, L. *J. Am. Chem. Soc.* **1997**, *119*, 3171.
28. Rudler, H.; Durand-Reville, T. *J. Organomet. Chem.* **2001**, *617*, 571.
29. Young, K. J. H.; Oxgaard, J.; Ess, D. H.; Meier, S. K.; Stewart, T.; Goddard, W. A.; Periana, R. A. *Chem. Commun.* **2009**, 3270.
30. Ahlquist, M.; Periana, R. A.; Goddard, W. A. *Chem. Commun.* **2009**, 2373.

**A HOMOLYTIC OXY-FUNCTIONALIZATION MECHANISM:
INTERMOLECULAR HYDROCARBYL MIGRATION FROM M-R TO
VANADYL OXO**

5.1 Introduction

The formation of carbon-oxygen bonds from metal-hydrocarbyl species is a central challenge to developing radical-free catalytic cycles for alkane functionalization. The intramolecular migration of hydrocarbyl groups (R) across metal-oxo (M=O) bonds is one means of oxy-functionalizing hydrocarbyl groups on electropositive metals, M-R to M-OR.¹⁻³ In a few experiments, direct evidence of such migrations (labeled as **Intra-M^{2e}** to indicate intramolecular migration resulting in a two-electron reduction) has been shown.¹⁻⁴ **Intra-M^{2e}** was also proposed to be responsible for C-O bond formation in the generation of phenol from OVCl_3 and HgPh_2 in cyclohexane (**Scheme 5.1**).⁵



Scheme 5.1 Mechanism for the formation of phenol by the reaction of Ph_2Hg and VOCl_3 proposed by Reichle *et al.*

We studied this reaction with quantum mechanics (density functional theory, M06//B3LYP^{6,7} see Supporting Information) including Poisson-Boltzmann implicit solvation.⁸ Surprisingly, we find that the oxidation of V-Ph to V-OPh is not through **Intra-M^{2e}** but rather is through an intermolecular phenyl migration to a separate metal-oxo. This is a new oxidation mechanism, **Inter-M^{1e}**, since, in contrast to previous (intra- and intermolecular) mechanisms that result in a two-electron reduction of either the M-R complex or oxidants,^{1-4,9-11} **Inter-M^{1e}** leads to a one-electron reduction of each reactant.

5.2 Results and discussion

First we studied **Intra-M^{2e}** of O=VCl₂Ph (**1**), a known intermediate generated by aryl transfer from HgPh₂ to O=VCl₃, and compared the free energy surface to those of [(HBpz₃)ReO₂(Ph)]OTf (**2**) and (HBpz₃)ReOPhCl (**3**) (HBpz₃ = hydrotris(1-pyrazolyl)borate, OTf = triflate). **Intra-M^{2e}** from Re⁺⁷ (**2**) is thermally accessible,³ whereas that from Re⁺⁵ (**3**) is known to be a photochemical reaction.^{1,2} Indeed, we find that **Intra-M^{2e}** of **2** poses a much lower barrier (19.1 kcal/mol, **Figure 5.1**) than that of **3** (54.9 kcal/mol), consistent with the experiments.¹⁻³ However, the barrier for **1** is calculated to be 40.7 kcal/mol, indicating that this reaction is not thermally accessible. This suggests that **Intra-M^{2e}** is not the pathway responsible for the oxidation of V-Ph to V-OPh. Indeed, Thiele *et al.* have synthesized and isolated **1**, and found no formation of phenoxides when **1** decomposes.¹²

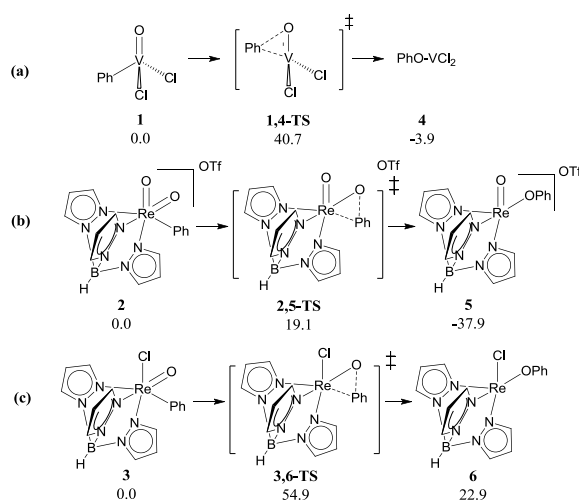


Figure 5.1 The comparison of three intramolecular phenyl metal-to-oxo migrations (**Intra-M^{2e}**, free energies in kcal/mol). The ground states of **1,4-TS**, **4**, and **6** are triplets.

Since **Intra-M^{2e}** is not responsible for the oxidation of the V-Ph bond and since V-OPh is formed, there must be another undiscovered mechanism that is responsible for the oxidation. In the experiments phenol was detected only when an excess of OVCl_3 is added to react with HgPh_2 ($\text{OVCl}_3/\text{HgPh}_2 > 2$).⁵ Therefore, we considered it possible that the unreacted OVCl_3 might serve as an oxidant and that V-Ph bonds are oxidized to V-OPh by transferring Ph intermolecularly from **1** to OVCl_3 , similar to the oxidation of CH_3ReO_3 by OsO_4 .¹⁰

We investigated this possibility and located a transition state in which phenyl migrates intermolecularly from OVCl_2Ph to the oxo of $\text{O}=\text{VCl}_3$ (**Figure 5.2** (a)). To our surprise, this reaction pathway poses a Gibbs free energy barrier of only 18.3 kcal/mol, consistent with the experiments, which show this to be a room-temperature reaction and absent of free radicals.⁵ In the transition state **1,7-TS**, the phenyl carbon is 2.12 Å away from V and

1.93 Å away from O*, while V*=O* is elongated from 1.56 to 1.71 Å, and O* is loosely coordinated to V with a bond distance of 1.96 Å, longer than the normal V-O single bond length (1.76 Å). Importantly, this transition state is described by an open-shell singlet (OSS) wavefunction with two unpaired, antiferromagnetically coupled electrons. One localizes at the V* of the oxidant, while the other is delocalized among V, O*, and the phenyl carbon (**Figure 5.2**). The product **7** has R(V--O*) = 2.00, R(C-O) = 1.41, and R(V*-O*) = 1.88 Å. The tetrahedral coordination of both metals is maintained in the product. The wavefunction of the product is also described as an OSS state with two unpaired electrons localized at two V⁺⁴. The triplet state of **7** is 0.1 kcal/mol uphill, suggesting there is slight superexchange interaction between the two metallic centers.

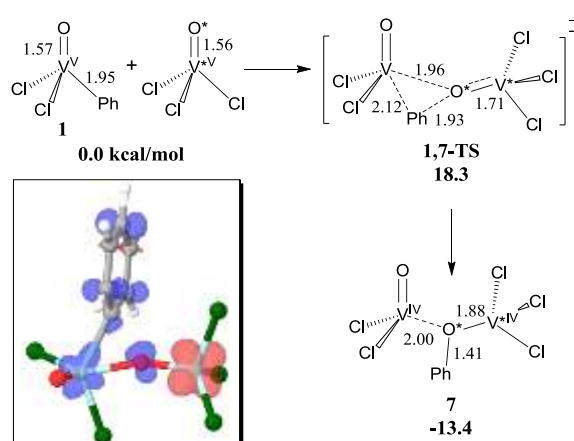


Figure 5.2 The free energy surface of the phenyl intermolecular migration from OVPhCl₂ to the oxo of O=VCl₃ (kcal/mol). The polarized spin density in the transition state (red and blue showing up and down spin) is shown in the inset.

Significantly, comparing to **Intra-M^{2e}**, we find that the barrier of the **Inter-M^{1e}** (where “1e” denotes the one-electron change in oxidation states) is 22.4 kcal/mol lower. This can be rationalized by the relative stability of V⁺⁴ with respect to V⁺⁵ and V⁺³ evident in the Pourbaix diagrams of vanadium.¹³ For illustration, the redox potentials of V⁺⁴/V⁺⁵ and V⁺³/V⁺⁴ ions in aqueous solution at pH = 0 (1.0 and 0.36 V vs NHE, respectively)¹⁴ show the comproportionation reaction V⁺⁵ + V⁺³ → 2 V⁺⁴ is exergonic by 15 kcal/mol. Previous studies have also found that a two-electron reduction of a V⁺⁵ oxo in the surface of V₂O₅ can lead to two V⁺⁴ centers via spontaneous comproportionation with an adjacent V⁺⁵ center.¹⁵

This reaction mechanism is unique compared to previous oxidation mechanisms (**Figure 5.3**). M-C bonds have been oxy-functionalized

- a. by nucleophilic attack (or reductive elimination),^{16,17} in which the metal in the M-R complex is formally reduced by two electrons;
- b. by organometallic Baeyer-Villiger oxidations,⁹ in which the oxidation state of the metal in the M-R complex remains unchanged;
- c. by electrophilic attack on carbon,^{10,18} in which the oxidation state of the metal in the M-R complex remains unchanged, while the oxidant is reduced by two electrons; or
- d. by **Intra-M^{2e}**,¹⁻³ in which the metal of the M-R complex is reduced by two electrons.

For the current system we find **Inter-M^{1e}** (**Figure 5.2**), in which both metals in the M-R complex and oxidant are formally reduced by one electron. This may offer a kinetic advantage to a process in which the oxidant is to be regenerated by triplet dioxygen.

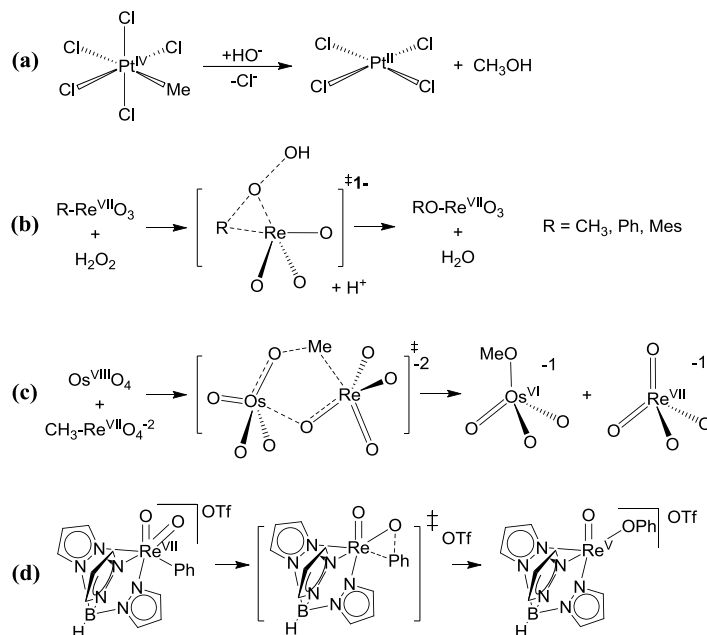


Figure 5.3 The comparison of the new oxy-functionalization to previous proposed mechanisms.

To expand the scope of this **Inter-M^{1e}** oxidation, we investigated the reaction of **1-Me** with OVCl_3 (**Figure 5.4**). In contrast to **1**, two transition states (TS) were located: the first TS (**1,7-TS-Me**) has a triangular V-C-O motif resembling **1,7-TS**, and the second TS (**1,7-TS'-Me**) has a linear V-C-O motif (including inversion of the methyl group) similar to the transition state for methyl transfer from $(\text{CO})_5\text{ReMe}$ to H_2SeO_3 .¹⁸ The most energetically favorable pathway is through **1,7-TS-Me** with a barrier of 26.5 kcal/mol, which is still 8.2 kcal/mol higher than that of **1**. This lower migratory aptitude of methyl is also observed in several other systems.¹⁹ The reaction through **1,7-TS'-Me** poses a

much higher barrier of 37.9 kcal/mol. This is presumably the result of forming the undercoordinated vanadium product OVCl_2 .¹⁵

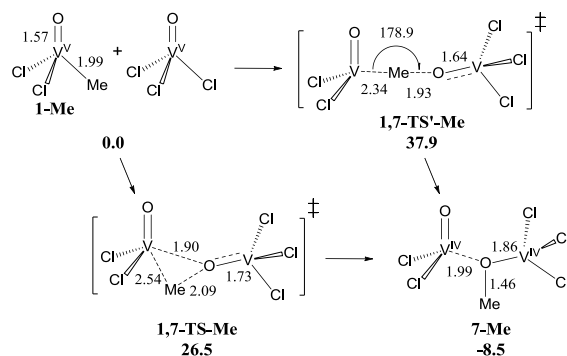


Figure 5.4 The free energy surface of the methyl intermolecular migration from VOMeCl_2 to the oxo of VOCl_3 (kcal/mol).

The **Inter-M^{1e}** mechanism will prove useful when integrated as the C-O formation step in a complete catalytic cycle for hydrocarbon oxidation. Characteristics of M-R intermediates with which **Inter-M^{1e}** should be compatible include

- consecutive oxidation states coupled by a high reduction potential (potentially $\text{Ru}^{\text{II/III/IV}}$, $\text{Ir}^{\text{III/IV}}$, $\text{Rh}^{\text{I/II/III}}$);
- a weak M-C bond (generally favoring 1st over 2nd over 3rd row metals);
- an ability of “M” to activate C-H bonds in its inorganic form “M-X” (later 2nd and 3rd row transition metals).

Possible catalytic cycles incorporating M=O oxidants prone to reduction by one-electron are outlined in **Figure 5.5** using methane as a hydrocarbon substrate. Following CH activation, **Path A** involves methyl transfer from the $\text{M}^{\text{n}}\text{-CH}_3$ intermediate followed

by one electron oxidation to regenerate the CH activating complex. The opposite sequence (oxidation then methyl transfer, **Path B**) is also feasible and may be favored by M^n-CH_3 with an oxidation potential lower than that of $M=O$. For species $M^{n+1}-CHR_2$ for which $M^{n+2}=CR_2$ is stable, $M=O$ oxidants may also prove useful by abstracting a hydrogen atom from an alkyl group (**Path C**). Formation of a metal-carbon π -bond makes hydrogen atom transfer accessible to oxo's with driving force lower than that required to activate alkanes directly. In acidic conditions, nucleophilic attack and protonolysis of the $M-CXR_2$ bond may lead to two-electron-oxidation products, or further oxidation may proceed.^{11,20}

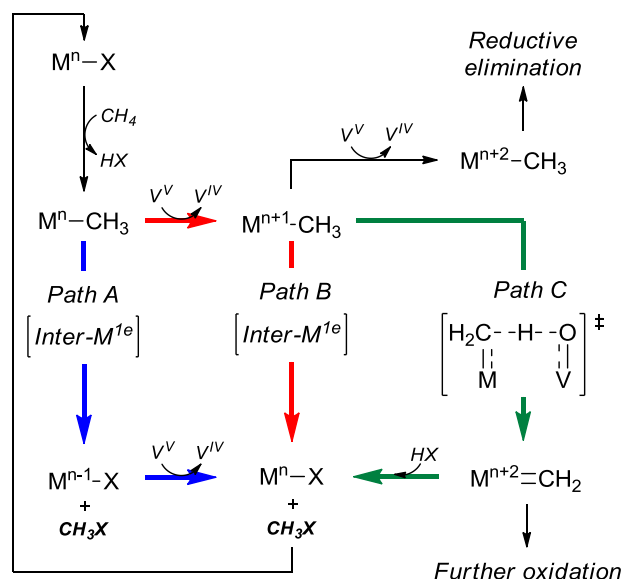


Figure 5.5 Possible mechanisms involving a vanadyl oxidant in a hydrocarbon oxidation cycle using CH_4 as the substrate.

As proof of concept that these mechanisms can be placed in the context of complete catalytic cycles without insurmountable increases in free energy, we calculated the Gibbs free energy surfaces for methane oxidation by rhodium and iridium complexes in aqueous solution using OVCl_3 as a model oxidant (**Figure 5.6**). 2,6-bis-(dimethylphosphinomethyl)pyridine was taken as a representative of thermally, protically stable pincer ligands known to support CH activation reactions.²¹ Energies are reported at pH = 0 (at which the oxidation potential of bare vanadates reaches 1.0V vs SHE¹³) for the Rh cycle and pH = 4 for Ir. In the case of the Rh^{III} hydroxo complex **A**, we found that the C-H activation product **B** lies 7.5 kcal/mol downhill following a barrier of 34.7 kcal/mol. Importantly, the **Inter-M^{1e}** mechanism poses an overall barrier of only 29.3 kcal/mol. The Rh^{II} aquo complex in **C** is then oxidized by a second OVCl_3 (exergonic 9.1 kcal/mol) to regenerate the Rh^{III} C-H activation catalyst (**D**) and hydrolysis of $\text{CH}_3\text{OV}^{+4}\text{Cl}_3$ (**D** to **E**) generates methanol irreversibly. Finally, reoxidation of two $\text{O}=\text{V}^{+4}\text{Cl}_3^-$ ions by $\text{O}_2(\text{g})$ to regenerate the oxidant (**E** to **F**) is exergonic 10.2 kcal/mol, suggesting vanadyl reagents with slightly higher oxidation potentials might expand the scope of this functionalization mechanism while maintaining air-regenerability.

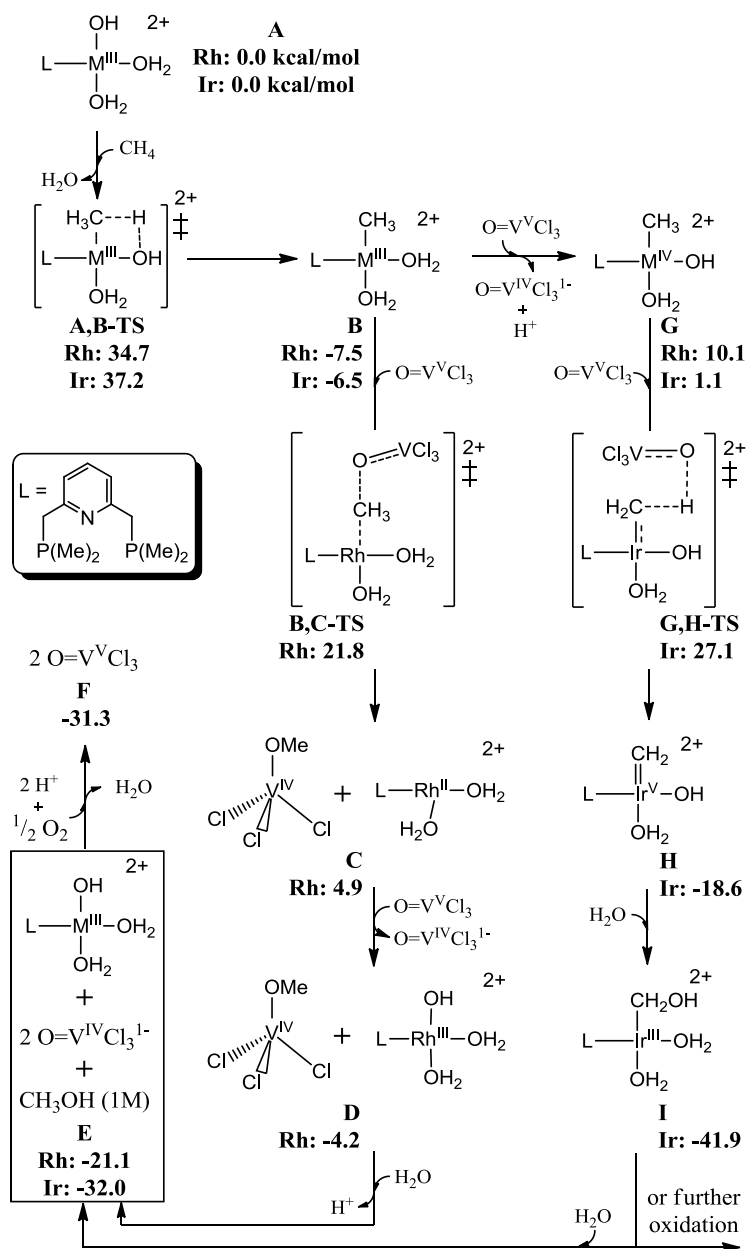


Figure 5.6 Gibbs free energy surface (kcal/mol) for methane functionalization by Rh and Ir pincer complexes and OVCl_3 at 298K in aqueous solution at $\text{pH} = 0$ (Rh) or $\text{pH} = 4$ (Ir).

Expecting the iridium analogue to access higher oxidation states, we investigated **Path C**, in which the Ir^{III} methyl complex is first oxidized to Ir^{IV} (**B** to **G**). Cyclic voltammetry has placed Ir^{III/IV} couples²² at potentials lower than the reduction potentials implied by the free energies for both **G** and OVCl₃ (1.31V and 0.97V vs SHE, respectively.) Subsequent hydrogen atom transfer to a second vanadyl poses a barrier of 26.0 kcal/mol (or a global barrier of 33.6 kcal/mol from the Ir^{III} methyl intermediate **B**.) Nucleophilic attack by water and protonolysis of the metal-carbon bond are a net 13.4 kcal/mol exergonic. The free energy surfaces suggest it is possible to integrate these one-electron oxidation mechanisms with a known C-H activation mechanism to yield complete cycles with thermally accessible barriers.

The rhodium catalyst in **Figure 5.6** is not an arbitrary choice. CH activation catalysts with lower oxidation potentials, such as Os(II) or Ru(II) hydroxides²³ or the Rh(II) porphyrins²⁴ known to cleave methane, can be deactivated via oxidation to inert oxidation states. The hard aquo ligands can participate in CH activation when deprotonated and stabilize the unpaired electron left by homolytic cleavage. Generally stronger covalent bonds of carbon to third row metals²⁵ suggest the rate of this functionalization will be higher among 1st and 2nd-row metals. Addressing the scope of this reactivity is underway.

5.3 Conclusions

In conclusion, we have studied the oxy-functionalization of VOPhCl₂ by means of density functional theory. We find that, instead of the expected intramolecular phenyl metal-to-oxo migration⁵, the oxidation is through an intermolecular phenyl migration to the oxo of a separate VOCl₃. The Gibbs free energy barrier is calculated to be only 18.3

kcal/mol, consistent with experiment (room temperature reaction completed in an hour). Importantly, we find the two electrons in the initial V-C bond are uncoupled during the reaction, leading to two vanadium centers which have been formally reduced to the stable +4 oxidation state. Therefore, we categorize this as a new oxy-functionalization mechanism involving two one-electron reductions, **Inter-M**^{1e}. This new mechanism can be verified experimentally by the reaction of isotopically labeled O¹⁸VCl₃ with OVCl₂Ph, for which the synthesis is well established.¹⁴

Moreover, we found that when phenyl is replaced by methyl, the migration barrier is 26.5 kcal/mol, thermally accessible at temperatures required for nonradical alkane activation. This suggests the possibility of integrating this functionalization mechanism into an alkane oxidation catalytic cycle. This idea is further supported by predicted barriers for the oxidation of model Rh and Ir intermediates by OVCl₃.

5.4 Computational details

The geometry optimizations and zero-point vibrational energy (ZPVE) were carried out with the B3LYP functional with the 6-31G** basis set for all atoms except V. For V the first two shells of core electrons were described by the Los Alamos angular momentum projected effective core potential (ECP) using the double- ζ contraction of valence functions.

Solvation energies were calculated using the Poisson-Boltzmann self-consistent polarizable continuum method implemented in Jaguar to represent cyclohexane (dielectric constant = 2.02 and effective radius = 2.78 Å). The solvation calculations used the B3LYP/LACVP** level of theory and the gas-phase optimized structures. For the

most accurate energetics, singlet-point energy calculations were performed using the M06 functional with a larger basis set: V was described with the triple- ζ contraction of valence functions augmented with two f -functions (exponents of 1.788 and 0.425, from Martin, J. M. L.; Sundermann, A. *J. Chem. Phys.* 2001, 114, 3408.) and the core electrons were described by the same ECP. The other atoms were described with the 6-311++G** basis set.

Unless otherwise noted, all energies discussed are free energies, calculated as

$$G_{298K} = E_{\text{elec}} + G_{\text{solv}} + \text{ZPVE} + \sum_{\nu} \frac{h\nu}{e^{h\nu/kT} - 1} + \frac{n}{2}kT - T(S_{\text{vib}} + 0.5 \times S_{\text{rot}} + 0.5 \times S_{\text{trans}}),$$

where $n = 12$ accounts for the potential and kinetic energies of the translational and rotational modes. Here we use only half magnitude of S_{trans} and S_{rot} to account the slowdown of solute translational and rotational motions causing by surrounding solvent molecules.

5.5 References

1. Brown, S. N.; Mayer, J. M. *J. Am. Chem. Soc.* **1994**, *116*, 2219.
2. Brown, S. N.; Mayer, J. M. *Organometallics* **1995**, *14*, 2951.
3. Brown, S. N.; Mayer, J. M. *J. Am. Chem. Soc.* **1996**, *118*, 12119.
4. Smeltz, J. L.; Boyle, P. D.; Ison, E. A. *J. Am. Chem. Soc.* **2011**, *133*, 13288.
5. Reichle, W. T.; Carrick, W. L. J. *Organomet. Chem.* **1970**, *24*, 419.
6. (a) Zhao, Y.; Truhlar, D. G. *Acc. Chem. Res.* **2008**, *41*, 157. (b) Zhao, Y.; Truhlar, D. G. *Theor. Chem. Acc.* **2008**, *120*, 215.

7. (a) Becke, A. D. *J. Chem. Phys.* **1993**, *98*, 5648. (b) Lee, C. T.; Yang, W. T.; Parr, R. G. *Phys. Rev. B* **1988**, *37*, 785.
8. (a) Marten, B.; Kim, K.; Cortis, C.; Friesner, R. A.; Murphy, R. B.; Ringnalda, M. N.; Sitkoff, D.; Honig, B. *J. Phys. Chem.* **1996**, *100*, 11775. (b) Tannor, D. J.; Marten, B.; Murphy, R.; Friesner, R. A.; Sitkoff, D.; Nicholls, A.; Ringnalda, M.; Goddard, W. A.; Honig, B. *J. Am. Chem. Soc.* **1994**, *116*, 11875.
9. (a) Conley, B. L.; Ganesh, S. K.; Gonzales, J. M.; Tenn, W. J.; Young, K. J. H.; Oxgaard, J.; Goddard, W. A.; Periana, R. A. *J. Am. Chem. Soc.* **2006**, *128*, 9018. (b) Bischof, S. M.; Cheng, M. J.; Nielsen, R. J.; Gunnoe, T. B.; Goddard, W. A.; Periana, R. A. *Organometallics* **2011**, *30*, 2079.
10. Conley, B. L.; Ganesh, S. K.; Gonzales, J. M.; Ess, D. H.; Nielsen, R. J.; Ziatdinov, V. R.; Oxgaard, J.; Goddard, W. A.; Periana, R. A. *Angew. Chem. Int. Ed.* **2008**, *47*, 7849.
11. Cheng, M. J.; Nielsen, R. J.; Ahlquist, M.; Goddard, W. A. *Organometallics* **2010**, *29*, 2026.
12. Thiele, K. H.; Schumann, W.; Wagner, S.; Bruser, W. *Z. Anorg. Allg. Chem.* **1972**, *390*, 280.
13. Pourbaix, M. *Atlas of Electrochemical Equilibria in Aqueous Solutions*; Pergamon Press: Oxford, New York, 1966.
14. Inzelt, G. In *Inorganic Electrochemistry*; Bard, A. J., Stratmann, M., Eds.; Wiley-VCH: 2006; Vol. 7a.
15. Sauer, J.; Dobler, J. *Dalton Trans.* **2004**, 3116.
16. Tilset, M.; Lersch, M. *Chem. Rev.* **2005**, *105*, 2471.

17. Vigalok, A. *Chem. Eur. J.* **2008**, *14*, 5102.
18. Tenn, W. J.; Conley, B. L.; Hovelmann, C. H.; Ahlquist, M.; Nielsen, R. J.; Ess, D. H.; Oxgaard, J.; Bischof, S. M.; Goddard, W. A.; Periana, R. A. *J. Am. Chem. Soc.* **2009**, *131*, 2466.
19. (a) Hawthorne, M. F.; Emmons, W. D.; Mccallum, K. S. *J. Am. Chem. Soc.* **1958**, *80*, 6393. (b) Stiles, M.; Mayer, R. P. *J. Am. Chem. Soc.* **1959**, *81*, 1497. (c) Brown, H. C.; Kim, C. J. *J. Am. Chem. Soc.* **1968**, *90*, 2082.
20. DuMez, D. D.; Mayer, J. M. *J. Am. Chem. Soc.* **1996**, *118*, 12416.
21. (a) Ben-Ari, E.; Leitun, G.; Shimon, L. J. W.; Milstein, D. *J. Am. Chem. Soc.* **2006**, *128*, 15390. (b) Young, K. J. H.; Lokare, K. S.; Leung, C. H.; Cheng, M. J.; Nielsen, R. J.; Petasis, N. A.; Goddard, W. A.; Periana, R. A. *J. Mol. Catal. A: Chem.* **2011**, *339*, 17. (c) Hashiguchi, B. G.; Young, K. J. H.; Yousufuddin, M.; Goddard, W. A.; Periana, R. A. *J. Am. Chem. Soc.* **2010**, *132*, 12542.
22. (a) Brewster, T. P.; Blakemore, J. D.; Schley, N. D.; Incarvito, C. D.; Hazari, N.; Brudvig, G. W.; Crabtree, R. H. *Organometallics* **2011**, *30*, 965. (b) Weinberg, D. R.; Hazari, N.; Labinger, J. A.; Bercaw, J. E. *Organometallics* **2010**, *29*, 89.
23. (a) Dobson, J. C.; Meyer, T. J. *Inorg. Chem.* **1988**, *27*, 3283. (b) Dobson, J. C.; Takeuchi, K. J.; Pipes, D. W.; Geselowitz, D. A.; Meyer, T. J. *Inorg. Chem.* **1986**, *25*, 2357.
24. (a) Sherry, A. E.; Wayland, B. B. *J. Am. Chem. Soc.* **1990**, *112*, 1259. (b) Sun, H.; Xue, F.; Nelson, A. P.; Redepenning, J.; DiMagno, S. G. *Inorg. Chem.* **2003**, *42*, 4507.
25. Simoes, J. A. M.; Beauchamp, J. L. *Chem. Rev.* **1990**, *90*, 629.

**EXPLANATION OF THE DRAMATIC DIFFERENCE BETWEEN THE
MECHANISM OF ACTIVATION AND FUNCTIONALIZATION OF
METHANE BY RU(II) AND OSII/RE: GUIDELINES FOR IMPROVED
CATALYSTS**

A.1 Introduction

Known homogeneous catalysts for the selective oxidation of methane are based on late transition metal ions stabilized in acidic, oxidizing media. Oxidations catalyzed by bare Pt,¹ Hg,² Au,³ and Pd^{4,5} cations dissolved in H₂SO₄ show selectivity for methyl bisulfate. Ligand-stabilized complexes of platinum in H₂SO₄ and palladium in trifluoroacetic acid also catalyze the formation of methyl esters, while PtCl₄²⁻ in aqueous HCl(HOAc) generates CH₃Cl (CH₃OAc). The electrophilicity of these metal centers fosters a high rate of H₃C-H bond cleavage by providing a driving force for the release of weakly basic anions in exchange for the electrons in the substrate, generating intermediates M(H)(CH₃) via insertion or M(CH₃) + HX via substitution. However, the required displacement of even weak bases from these metals by methane poses a high activation barrier, and reactivity can be quenched if the chemical potential of protons is too low to labilize the departing anion. Also, oxidants required to access the higher oxidation state in some of these catalytic cycles are either expensive or stronger than the desired terminal oxidant O₂ (e.g., Pt(IV) salts, H₂SeO₄ or K₂S₂O₈). Thus the electronegativity of the late transition metals undermines their industrial application.

To aid in the design of selective alkane oxidation catalysts based on less electrophilic metals, we have studied the free energy surface of Ru^{II}, Os^{II}, and Re^I complexes reacting with methane. Thermochemistry and wavefunctions are derived from density functional theory and a polarizable continuum solvent model, augmented in some cases by explicit solvation. For simplicity we limit ourselves to bis-bipyridine metal hydroxide complexes, which are synthetically realistic, amenable to derivatization and whose electrochemistry has been studied. The protonation and dissociation of hydroxide ligands is used to establish resting states and vacancy formation energies as functions of pH. Two mechanisms for C-H activation are compared: insertion (also called oxidative addition) and internal substitution (the 1,2-addition of a C-H bond across an M-OH bond).

Methyl groups on these Group 7 and 8 metals are more electron-rich than those of Group 9-12 metals (*vide infra*), and are expected to be susceptible to electrophilic functionalization mechanisms⁶⁻⁸ rather than reductive elimination or nucleophilic attack. To measure the reactivity of the M-CH₃ intermediates toward electrophilic C-O bond formation, we also calculated barriers for the S_E2 attack by a model metal-oxo species ((acac)₂Os^{VI}(O)₂).

We reasoned that electron-donating substituents on the pyridyl rings would provide a practicable means of tuning the quasi-*t*_{2g} orbital energies independently of the metal's identity. Also, through the deprotonation of such substituents, the pH of the medium may alter the electronic characteristics of the metal center and increase solubility. Activation barriers were therefore computed using a series of 4,4'-substituted bipyridine ligands. This provided relationships between molecular orbital energies and kinetics, and

identified complexes capable of thermally generating both M-CH₃ intermediates from methane and carbon-heteroatom bonds through reaction with a weak oxidant.

The identity of the coordinating anion involved in internal substitution reactions has been identified as an important parameter. The pK_a of the coordinated anion determines whether the anion is protonated or available for reaction, and therefore the observed activation barriers, as a function of pH. Simultaneously, the formation of vacant sites at which methane can react is related to the concentration of free anions, and thus also to pH. Finally, proton transfer to and from organic ligands (such as bipyrimidine) or spectator coordinated anions (such as hydroxide and amide) provides a fast and potent means of modifying the electronic properties of the metal center. Thus predictive modeling requires an accurate accounting of pK_a's.

The computational algorithm is defined and evaluated against organometallic pK_a's and M(CH₃)(D)↔M(CH₂D)(H) scrambling barriers in the following section. The Results and Discussion contains the quantitative presentation of free energy surfaces, orbital energies and structural parameters, followed by a broader discussion of the interplay of metal orbitals, ligands, pH and kinetics, and implications for the design of complete catalytic cycles.

A.2 Computational Details and Evaluation

Computation Details Geometries were optimized using the B3LYP⁹⁻¹¹ functional, the 6-31G**^{12,13} basis for light atoms, and a double- ζ contraction of the Los Alamos valence functions and pseudopotentials¹⁴ for metals. Hessians at these geometries

provided the zero point energy and vibrational enthalpy and entropy. Solvation free energies G_{solv} were computed using the Poisson-Boltzmann polarizable continuum model with a dielectric constant of 80 and solvent radius of 1.4 Å. The electronic energy E_{elec} was evaluated with the M06¹⁴⁻¹⁶ functional and the 6-311G**++^{17,18} basis and a triple- ζ contraction of the Los Alamos valence functions augmented with diffuse s and p functions and two f -functions.¹⁹

Gibbs free energies of organometallic species at 1M and 298K were computed according to

$$G = E_{\text{elec}} + G_{\text{solv}} + \text{ZPE} + H_{\text{vib}} + 6kT - TS_{\text{vib}},$$

where $6kT$ accounts for the kinetic and potential energy of translation and rotation contribution. Rotational and translational entropy for each organometallic species were assumed to cancel. Free energies of methane, water, and hydroxide ion at 1 atm were calculated using ideal gas statistical mechanics and the above prescription for electronic energies. We then added ΔG (1 atm \rightarrow liquid, H₂O) = -2.05 kcal/mol and ΔG (1 atm \rightarrow 1 M, OH¹⁻) = -103.0 kcal/mol to determine the respective free energies of water and hydroxide appropriate for an aqueous solution of pH = 14.

Thermochemistry Evaluations We chose two types of chemical reactions, where reliable experimental data exist, for validating the free energies used in this work: (1) alkyl/hydride site exchange in $[(C_5Me_5)Os(dmpm)(CH_3)(H)]^{1+}$ (dmpm = bis(dimethylphosphino)methane, solvent = CDFCl₂)²⁰ and $[(C_5H_5)_2Re(CH_3)(H)]^{+1}$ (solvent = CD₂Cl₂),²¹ during which the oxidation states of Os and Re are reduced by two; (2) deprotonation of *cis*- and *trans*- $[(bpy)_2M(OH_2)_2]^{2+}$,^{22,23} and $[(trpy)Os(OH_2)_3]^{2+}$,²⁴

where M is Os or Ru, and bpy and trpy are 2,2'-bipyridine and 2,2';6'2''-terpyridine, respectively. The first reaction evaluates the performance of the current approach in predicting reaction barriers, and the second evaluates pKa's relevant to this study.

Our calculated Gibbs free energy barrier for exchange of protons between the hydride and methyl sites in $[(C_5Me_5)Os(dmpm)(CH_3)(H)]^{1+}$ at 173 K is 9.1 kcal/mol (**Scheme A.1 (a)**). This value is in good agreement with the experimental measurement of 8.1 kcal/mol, based on temperature-dependent spin saturation transfer.²⁰ The product, $[(C_5Me_5)Os(dmpm)(CH_4)]^{1+}$, is an Os(II) σ -methane complex with a free energy 4.7 kcal/mol higher than the reactant, consistent with experiments, since no stable σ -methane complex is observed.²⁰

For $[(C_5H_5)_2Re(CH_3)(H)]^{+1}$, we calculated the free energy barrier to be 15.0 kcal/mol at 225 K (b), in good agreement with the temperature-dependent NMR measurement of 16.9 kcal/mol.²¹ The corresponding product, $[(C_5H_5)_2Re(CH_4)]^+$ is 12.5 kcal/mol unstable compared to the reactant, consistent with experiments in which no σ -methane complex was observed.²¹

<i>cis</i> -[(bpy) ₂ Ru(OH ₂) ₂] ²⁺	13.0	8.9
<i>cis</i> -[(bpy) ₂ Ru(OH ₂)(OH)] ¹⁺	15.2	> 11.0
<i>trans</i> -[(bpy) ₂ Ru(OH ₂) ₂] ²⁺	11.0	9.2
<i>trans</i> -[(bpy) ₂ Ru(OH ₂)(OH)] ¹⁺	13.9	> 11.5
<i>cis</i> -[(bpy) ₂ Os(OH ₂) ₂] ²⁺	9.1	7.9
<i>cis</i> -[(bpy) ₂ Os(OH ₂)(OH)] ¹⁺	8.8	11.0
<i>trans</i> -[(bpy) ₂ Os(OH ₂) ₂] ²⁺	6.2	8.2
<i>trans</i> -[(bpy) ₂ Os(OH ₂)(OH)] ¹⁺	10.9	10.2
[(trpy)Os(OH ₂) ₃] ²⁺	5.6	6.0
[(trpy)Os(OH ₂) ₂ (OH)] ¹⁺	6.3	8.0
[(trpy)Os(OH ₂)(OH) ₂]	10.9	11.0

A.3 Results and Discussion

C-H Activation by Os^{II}, Ru^{II}, and Re^I with Unsubstituted Bipyridine Ligands We discuss the C-H activation free energy surfaces in two parts: (1) equilibrium of possible resting states, including [(bpy)₂M(OH)(OH₂)]ⁿ⁺¹, [(bpy)₂M(OH)₂]ⁿ, and [(bpy)₂M(OH)]ⁿ⁺¹, and (2) subsequent C-H cleavage by the five-coordinate intermediate. This facilitates distinctions between effects on ground states and pH-independent C-H cleavage barriers. Dihydroxide species [(bpy)₂M(OH)₂]ⁿ with 1 atm methane and 1M hydroxide is taken as the reference point of the free energy surfaces.

The protonation of the dihydroxide **1-Ru-H** to form **2-Ru-H** is downhill by $\Delta G_{1\rightarrow 2} = -1.1$ kcal/mol (**Figure A.1** (a)). However, dissociating one hydroxide from **1-Ru-H** to **3-Ru-H** is uphill by $\Delta G_{1\rightarrow 3} = 5.2$ kcal/mol. This makes **2-Ru-H** the resting state at pH =

14. Interestingly, in **3-Ru-H** the remaining hydroxide ligand relaxes from its octahedral position by shortening the Ru-OH bond by 0.09 Å and bisecting the N-Ru-N angle ($\theta_1 = 152.1^\circ$, $\theta_2 = 121.2^\circ$, see **Scheme A.2**). This indicates a significant $p_\pi \rightarrow d_\sigma$ interaction. This interaction stabilizes the 16-electron intermediate and may be responsible for the absence of stable σ -methane complexes $(\text{bpy})_2\text{M}(\text{CH}_4)(\text{OH})^n$ for each metal.

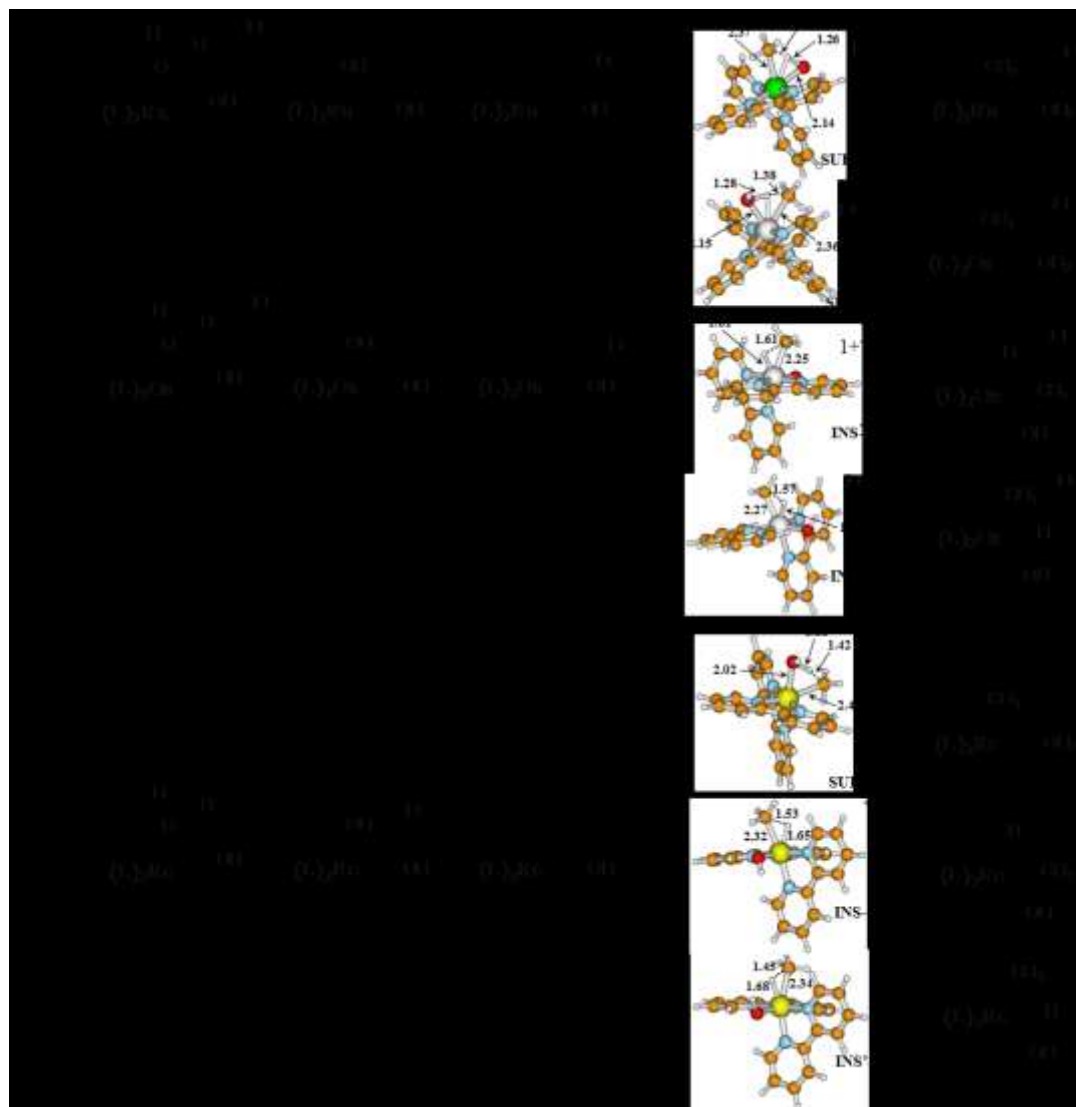
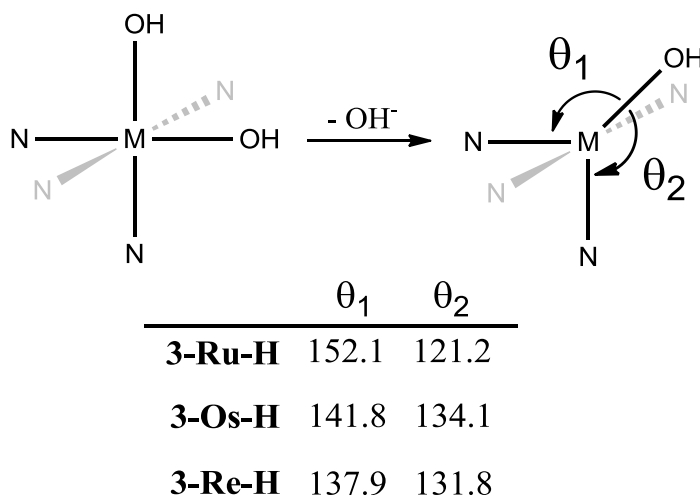


Figure A.1 Gibbs free energy surfaces of methane C-H activation by unsubstituted *bis*-2,2'-bipyridine complexes of Os, Ru, and Re complexes, including aqueous solvation. (Free energy in kcal/mol for energy, and bond lengths in angstrom.)



Scheme A.2

The cleavage of methane C-H bonds by **3-Ru-H** is via a substitution pathway, in which Ru-CH₃ and O-H bonds are formed in a concerted, “2+2” rearrangement. This mechanism is ostensibly responsible for benzene C-H activation by TpRuL(OH)²⁵ and (acac)₂Ir(OMe).²⁶ The transition state, **SUB-TS-Ru-H**, is endergonic relative to **3-Ru-H** ($\Delta G_{3 \rightarrow \text{SUB-TS}} = 25.9$ kcal/mol), and has $R(\text{Ru-C}) = 2.37$ Å, $R(\text{C-H}) = 1.40$ Å, $R(\text{H-O}) = 1.26$ Å, and $R(\text{Ru-O}) = 2.14$ Å. It is noteworthy that the bond distance between Ru and the migrating hydrogen is 1.95 Å, suggesting this is a substitution reaction not an oxidative hydrogen migration, within which a shorter $R(\text{M-H}) \approx 1.6$ Å is expected. The product, **4-Ru-H**, is $\Delta G_{3 \rightarrow 4} = 7.5$ kcal/mol uphill compared to **3-Ru-H**. Taking the

resting state, **2-Ru-H** + CH_{4(g)}, as a reference point, the overall C-H activation barrier ($\Delta G_{\text{SUB}}^{\ddagger}$) is 32.2 kcal/mol, and the overall reaction energy (ΔG_{SUB}) is 13.8 kcal/mol, both of which suggest that this Ru complex is a promising catalyst for activating methane C-H bonds under thermal conditions.

In contrast to **1-Ru-H**, both the protonation of **1-Os-H** to **2-Os-H** and hydroxide dissociation to **3-Os-H** are endergonic by $\Delta G_{1\rightarrow 2} = 7.8$ kcal/mol and $\Delta G_{1\rightarrow 3} = 11.1$ kcal/mol (**Figure A.1** (b)), making **1-Os-H** the resting state at pH = 14. Similar to its Ru counterpart, the five-coordinated species, **3-Os-H**, has a new formed $p_{\pi} \rightarrow d_{\sigma}$ interaction, as indicated by the significant relaxation of the OH ligand significantly deviated from its octahedral position ($\theta_1 = 141.8^{\circ}$, $\theta_2 = 134.1^{\circ}$).

The free energy cost of H₃C-H bond cleavage by pentacoordinate **3-Os-H** through the substitution mechanism is $\Delta G_{3\rightarrow \text{SUB-TS}} = 30.7$ kcal/mol. The transition state, **SUB-TS-Os-H**, has R(Os-C), R(C-H), R(O-H), R(Os-O), and R(Os-H) equal to 2.36, 1.38, 1.28, 2.15, and 1.96 Å, resembling its Ru counterpart. The product **4-Os-H** is $\Delta G_{3\rightarrow 4} = 10.6$ kcal/mol less stable than **3-Os-H**. The overall C-H activation barrier and reaction energy are $\Delta G_{\text{SUB}}^{\ddagger} = 41.8$ and $\Delta G_{\text{SUB}} = 21.7$ kcal/mol, indicating that this is a kinetically inaccessible reaction under thermal conditions.

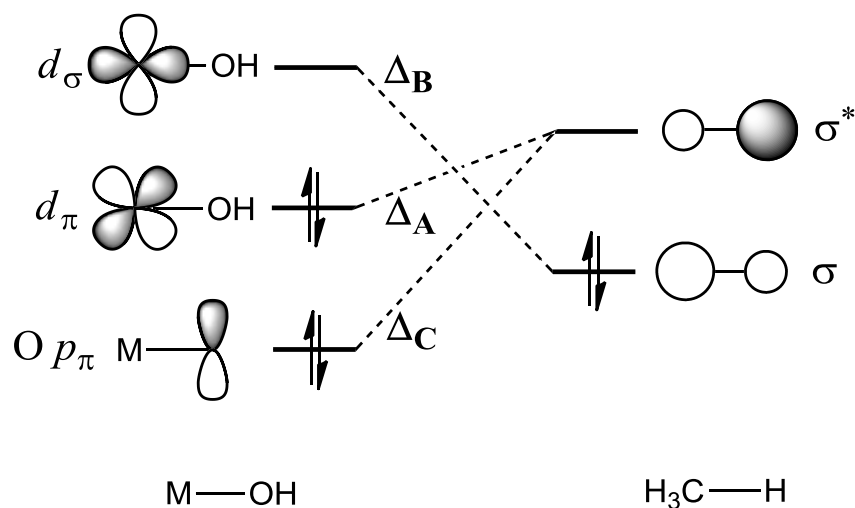
In contrast to the Ru system, two insertion C-H activation pathways are present on the Os free energy surface. In the first insertion pathway, the transition state, **INS-TS-Os-H**, is uphill by $\Delta G_{3\rightarrow \text{INS-TS}} = 20.6$ kcal/mol relative to **3-Os-H**, and has R(Os-C) = 2.25 Å, R(C-H) = 1.61 Å, and R(Os-H) = 1.61 Å. The product, **5-Os-H**, is 19.6 kcal/mol ($\Delta G_{3\rightarrow 5}$) higher than **3-Os-H**, and has methyl adjacent to hydroxide with R(Os-C) = 2.17

Å and $R(\text{Os-H}) = 1.59$ Å. **INS-TS-Os-H** and **5-Os-H** are both structurally and energetically similar to each other, showing that **INS-TS-Os-H** is a late transition state. The overall C-H activation barrier is $\Delta G_{\text{INS}}^{\ddagger} = 31.7$ kcal/mol. However, the total reaction energy is $\Delta G_{\text{INS}} = 30.7$ kcal/mol. For the global activation energy of the catalytic cycle to remain below 35.0 kcal/mol, the barrier of the desired oxy-functionalization of this methyl intermediate must be nearly negligible.

The second insertion pathway is energetically less favorable than the first. Relative to **3-Os-H**, the transition state, **INS'-TS-Os-H**, is uphill by $\Delta G_{3 \rightarrow \text{INS}'\text{-TS}} = 26.6$ kcal/mol, 6.0 kcal/mol more unstable than **INS-TS-Os-H**; its structure has $R(\text{Os-C}) = 2.27$ Å, $R(\text{C-H}) = 1.57$ Å, and $R(\text{Os-H}) = 1.61$ Å, similar to those in **INS-TS-Os-H**. The product **6-Os-H**, in which hydride is adjacent to hydroxide, is 24.4 kcal/mol ($\Delta G_{3 \rightarrow 6}$) higher in energy than **3-Os-H**, and has $R(\text{Os-C}) = 2.20$ Å and $R(\text{Os-H}) = 1.59$ Å, similar to those in **5-Os-H**. The total C-H activation barrier is $\Delta G_{\text{INS}'}^{\ddagger} = 37.7$ kcal/mol, and the total reaction energy is $\Delta G_{\text{INS}'} = 35.5$ kcal/mol, indicating that this is a kinetically inaccessible and thermodynamically unstable reaction.

We also noticed that in this system C-H activation through an insertion is kinetically more favorable than through a substitution fashion. This can also be rationalized in terms of frontier molecular orbital interactions between the five-coordinated intermediate **3** and methane (**Scheme A.3**). Disregarding geometric factors, insertion pathways are governed by two pairs of molecular orbital interactions: (a) metal $d_{\pi} \rightarrow \text{C-H } \sigma^*$ ($\Delta_A = E(\sigma^*) - E(d_{\pi})$), and (b) $\text{C-H } \sigma \rightarrow \text{metal } d_{\sigma}$ ($\Delta_B = E(d_{\sigma}) - E(\sigma)$). On the other hand, substitution pathways are ruled by (a) oxygen $p_{\pi} \rightarrow \text{C-H } \sigma^*$ ($\Delta_C = E(\sigma^*) - E(p_{\pi})$), and (b) $\text{C-H } \sigma \rightarrow$

metal d_σ ($\Delta_B = E(d_\sigma) - E(\sigma)$). Since one of the molecular orbital interactions is present in both pathways ($\text{C-H } \sigma \rightarrow \text{metal } d_\sigma$), the difference between barriers depends on the other interaction. Our results show that in the Os system $\Delta_A = 8.2$ eV is smaller than $\Delta_C = 11.8$ eV, suggesting that metal $d_\pi \rightarrow \text{C-H } \sigma^*$ is stronger than oxygen $p_\pi \rightarrow \text{C-H } \sigma^*$. [It should be noted that all the orbital energies discussed in this work are based on B3LYP/LACVP** level of theory with Poisson-Boltzmann polarizable continuum model] Accordingly, the insertion pathway is more facile than the substitution.



Scheme A.3

Moreover, this arrangement of molecular orbital energies ($\Delta_A = 8.2$ eV $>$ $\Delta_B = 9.9$ eV in Os-H case) distinguishes the *nucleophilic* driving force behind these insertions from the *electrophilic* insertion of $(\text{H}^+ \text{-bipyrimidine})\text{Pt}(\text{Cl})$ into methane. We recently reported that the $\text{C-H } \sigma \rightarrow \text{metal } d_\sigma$ interaction ($\Delta_B = 12.2$ eV) was *stronger* than the metal $d_\pi \rightarrow \text{C-H } \sigma^*$ interaction ($\Delta_A = 18.1$ eV) in that system due to the relative stability of the occupied and unoccupied Pt orbitals.

The C-H activation free energy surfaces of the Re system resemble those of Os qualitatively. At pH = 14, the resting state is **1-Re-H**. Protonation and one hydroxide dissociation from **1-Re-H** are endergonic by $\Delta G_{1\rightarrow 2} = 4.8$ kcal/mol and $\Delta G_{1\rightarrow 3} = 4.0$ kcal/mol, respectively (**Figure A.1** (c)). The product of the hydroxide dissociation, **3-Re-H**, also has an hydroxide ligand distorted from its octahedral position, indicating a notable $d_{\sigma}-p_{\pi}$ interaction ($R(\text{Re-OH}) = 1.94$ Å, $\theta_1 = 137.9^\circ$, $\theta_2 = 131.8^\circ$).

For the substitution pathway the Re complex poses a higher barrier than Os and Ru, $\Delta G_{3\rightarrow \text{SUB-TS}} = 37.9$ kcal/mol. The transition state, **SUB-TS-Re-H**, has $R(\text{Re-C}) = 2.40$ Å, $R(\text{C-H}) = 1.42$ Å, $R(\text{O-H}) = 1.22$ Å, and $R(\text{Re-O}) = 2.02$ Å. The product, **4-Re-H**, is 22.5 kcal/mol ($\Delta G_{3\rightarrow 4}$) uphill compared to **3-Re-H**. This is significantly more endergonic than the Ru and Os systems ($\Delta G_{3\rightarrow 4} = 7.5$ kcal/mol for Ru and 10.6 kcal/mol for Os). The overall C-H activation barrier of this mechanism is $\Delta G_{\text{SUB}}^\ddagger = 41.9$ kcal/mol, suggesting that methane C-H activation is unlikely to take place via substitution.

Similar to the Os system, two insertion transition states are located in the Re system. Relative to the pentacoordinate intermediate **3-Re-H**, these are endergonic $\Delta G_{3\rightarrow \text{INS-TS}} = 22.9$ kcal/mol and $\Delta G_{3\rightarrow \text{INS}'\text{-TS}} = 30.4$ kcal/mol, more so than in the Os case. However, $\Delta G_{3\rightarrow 5}$ and $\Delta G_{3\rightarrow 6}$ are 14.5 and 18.6 kcal/mol, respectively, smaller than those in the Os system ($\Delta G_{3\rightarrow 5} = 19.6$ kcal/mol and $\Delta G_{3\rightarrow 6} = 24.4$ kcal/mol). Because of the relative ease of hydroxide dissociation, the overall C-H activation barriers are $\Delta G_{\text{INS}}^\ddagger = 26.9$ and $\Delta G_{\text{INS}'}^\ddagger = 34.4$ kcal/mol, lower than those at their Os analogues. This suggests that this Re complex is promising for activating methane C-H bonds through an insertion mechanism.

Compare to those three systems, we found that the displacement of metal has significant impact on Gibbs free energy surfaces. Protonation energies of species **1** ($\Delta G_{1\rightarrow 2}$) decreases with the order of Os (7.8 kcal/mol) > Re (4.8 kcal/mol) > Ru (-1.1 kcal/mol), indicating **1-Os-H** is the weakest base, followed by **1-Re-H**, and then **1-Ru-H**. This is consistent with experimental results by Meyer and coworkers showing that the pKa of **2-Os-H** is 11.0 while that of **2-Ru-H** is larger than 11.0.^{22,24} The weaker basicity of **1-Os-H** compared to **1-Ru-H** is primarily due to **1-Os-H** having a larger magnitude of the metal-to-bipyridine π -backbonding than **1-Ru-H**, making the Os atom more electron-deficient.^{27,28} As a result, more electron density is drawn from hydroxide to Os, making the hydroxide in **1-Os-H** a weaker base. This is supported by our ALMO calculations showing that the charge transfer of $M(OH)_2 \rightarrow$ bipyridine in **1-Os-H** (4.9 eV) is much larger than that in **1-Ru-H** (2.9 eV), while the difference in the bipyridine $\rightarrow M(OH)_2$ is relatively small (3.9 eV for **1-Os-H** and 3.4 eV for **1-Ru-H**). In fact, we calculate that in the absence of π -accepting ligands the protonation energies of $(NH_3)_4Os(OH)_2$ and $(NH_3)_4Ru(OH)_2$ are similar: -9.7 kcal/mol and -12.2 kcal/mol, respectively. The higher basicity of **1-Re-H** relative to **1-Os-H** is expected due to its lower nuclear charge.

The energy cost of dissociating a hydroxide from **1** ($\Delta G_{1\rightarrow 3}$) has the order Os (11.1 kcal/mol) > Ru (5.2 kcal/mol) > Re (4.0 kcal/mol). It is common to see $\Delta G_{1\rightarrow 3}(Os) > \Delta G_{1\rightarrow 3}(Ru)$, since the third-row transition metals bind ligands more tightly than do second-row transition metals. $\Delta G_{1\rightarrow 3}(Os) > \Delta G_{1\rightarrow 3}(Re)$ is also expected, because Os^{II} is more electron-deficient than Re^I and is expected to bind anionic hydroxide more tightly.

$\Delta G_{3 \rightarrow \text{SUB-TS}}$, the energy cost (from pentacoordinate **3**) to cleave methane C-H bonds via substitution, has an order of Re (37.9 kcal/mol) > Os (30.7 kcal/mol) > Ru (25.9 kcal/mol). **3-Re-H** posing a larger $\Delta G_{3 \rightarrow \text{SUB-TS}}$ may be related to the thermodynamic instability of its product, **4-Re-H**, relative to those of ruthenium and osmium. $\Delta G_{3 \rightarrow 4}$ is 22.5 kcal/mol for Re, while only 7.5 and 10.6 kcal/mol for Ru and Os, and in accord with Hammond's postulate **3-Re-H** involves a later transition state and a larger $\Delta G_{3 \rightarrow \text{SUB-TS}}$. The total substitution barriers (from the dihydroxide resting states at pH = 14) involving Re and Os are similar for all ligands (41.8 kcal/mol for Os and 41.9 kcal/mol for Re), suggesting the contrary effects of increasing nucleophilicity on hydroxide dissociation and C-H cleavage approximately cancel at the transition state.

A larger $\Delta G_{3 \rightarrow \text{SUB-TS}}$ for **3-Os-H** than for **3-Ru-H** is also related to the stabilization of the five-coordinate products by the degree of π -bonding between the metal and hydroxide. Since this interaction is to be broken in the transition state, the stronger the interaction, the larger the barrier. The magnitude of the $d_{\sigma}-p_{\pi}$ interaction is accessible through the metal-OH rotation barrier, since rotation orthogonalizes the oxygen lone pair and d_{σ} orbital. Our results show that this barrier is 12.4 kcal/mol for **3-Os-H**, whereas it is only 7.1 kcal/mol for **3-Ru-H**; accordingly, **3-Os-H** poses a larger $\Delta G_{3 \rightarrow \text{SUB-TS}}$.

When comparing $\Delta G_{3 \rightarrow \text{INS-TS}}$ between the Os and Re systems, we found that insertion reactions are slightly more facile for **3-Os-H** (20.6 kcal/mol) than for **3-Re-H** (22.9 kcal/mol). This was unexpected based on the highly reducing nature of Re^{I} . Analyzing the intrinsic reaction coordinate of the insertion pathway by EDA-ALMO (**Figure A.2**), we found that early in the reactions the CH_4 -to-metal charge transfer stabilization term

dominates the metal-to-CH₄ term. Both terms remain significant at the transition states, where they are closer in magnitude for Os than for Re. This emphasizes the persisting importance of metal electrophilicity in these metals. As the reaction proceeds, metal-to-CH₄ charge transfer plays an increasing role in stabilizing the seven-coordinate product; since Re is more nucleophilic, $\Delta G_{3 \rightarrow 5}$ of Re is less endothermic than in the case of Os. The total insertion barriers are lower for the rhenium complexes, since dissociation of hydroxide is unambiguously promoted by nucleophilicity.

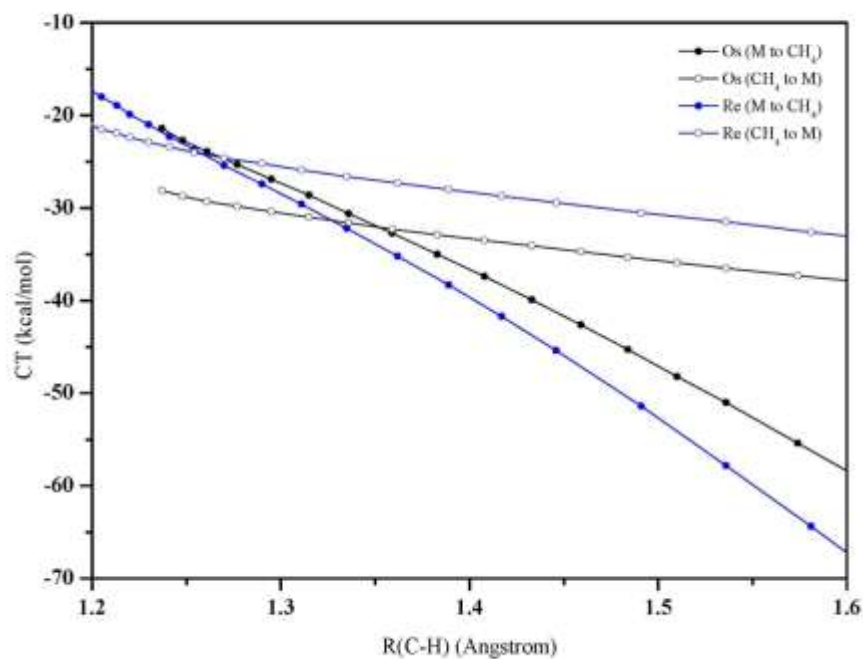
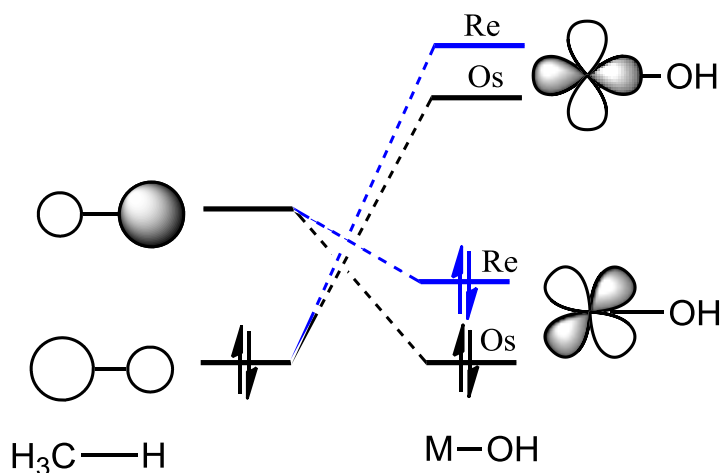


Figure A.2 Metal-to-CH₄ and CH₄-to-metal charge transfer along intrinsic reaction coordinate of the insertion pathways.

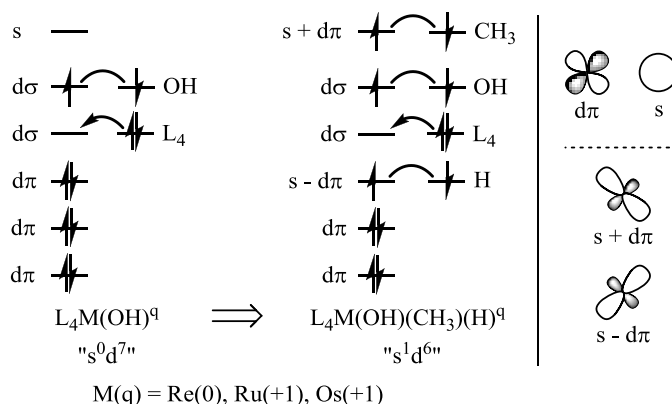


Scheme A.4

The Lack of Insertion Pathway in the Second-row Transition metal Among the three metals, we found that Ru system is distinguished from the others by the absence of an insertion pathway. This may be traced to the intrinsic *s* and *d* orbital energy splittings of atoms. The atomic spectra show the ground state of osmium, a quintet s^2d^6 configuration, lies 5144 cm^{-1} below the s^1d^7 state. The quintet s^1d^7 ground state of ruthenium lies 7483 cm^{-1} below the s^2d^6 state, a reversal of 36 kcal/mol . This trend can be observed across the transition series. The generation of seven-coordinated species **5** or **6** requires the metal to form two new covalent bonds to carbon and hydrogen. This is accomplished by hybridizing an occupied d_{π} orbital with a formally unoccupied *s* orbital to produce two orthogonal “ $s + d$ ” and “ $s - d$ ” hybrids (Scheme A.5). The *s* orbitals of 3rd row transition metals are both spatially contracted and energetically stabilized relative to the orbitals of higher angular momentum, which do not interact as strongly with the nucleus. Accordingly, *s-d* hybridization is energetically favorable for Os and

Re, but is unfavorable for Ru, resulting in the absence of insertion mechanisms.

Moving across an isoelectronic series in the third row (Re^{I} , Os^{II} , Ir^{III}), the 5d orbitals of lower principle quantum number are stabilized relative to the 6s. In the Ir^{III} cation, the s^1d^7 ground state lies 17210 cm^{-1} below the s^2d^6 configuration. As a result, CH activation by iridium(III) methoxide and carboxylate complexes employ the substitution mechanism rather than access Ir(V) intermediates. Steric factors, a constant in these calculations, can also influence insertion barriers.



Scheme A.5

C-H Activation by Os^{II} , Ru^{II} , and Re^{I} with Substituted Bipyridine Ligand Having established fundamental C-H activation mechanisms for Ru, Os, and Re 2,2'-bipyridine complexes, we further investigated the substituent effect by replacing hydrogen atoms at 4 and 4' positions of 2,2'-bipyridine by $\mathbf{X} = \text{NO}_2$, OH, NH_2 , and O^- for the Os and Ru systems, and $\mathbf{X} = \text{NO}_2$, OH, and NH_2 for the Re system. For $\mathbf{X} = \text{O}^-$ and OH, we place four explicit water molecules, one with each substituent \mathbf{X} .

We found that this substituent effect has significant impact on the equilibria among the aquo hydroxide (**2**), dihydroxide (**1**), and hydroxide species (**3**). As X becomes more donating, both protonation and hydroxide dissociation become exothermic (**Figure A.3**), causing changes in the resting states. For ruthenium, the resting states are the aquo hydroxo species **2**, except for X = NO₂, where dihydroxide species **1** is the resting state. For third row elements, the resting states at pH = 14 are dihydroxide species **1**, except for X = O⁻ (osmium) and X = NH₂ (rhenium), where the resting state is the five-coordinated species **3**.

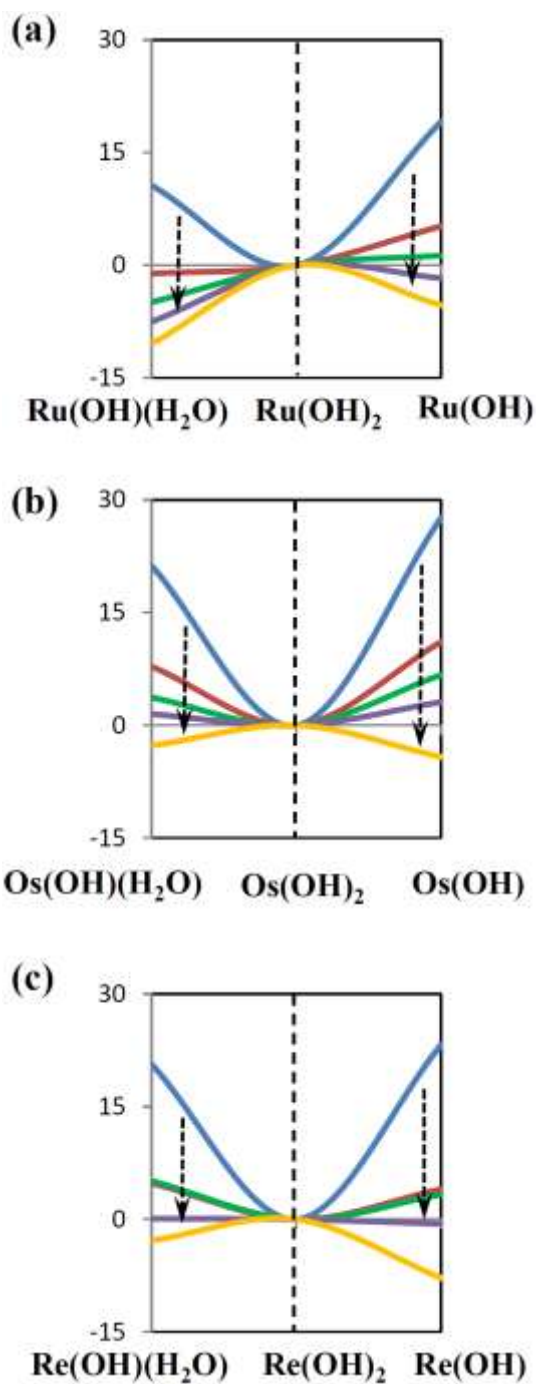


Figure A.3 Substituent effect on the free energies of $(4,4'\text{-X-bipyridine})_2M(OH)(H_2O)$, $M(OH)_2$, and $M(OH)$ bipyridine species, where blue, red, green, purple, and yellow lines represent $X = NO_2, H, OH, NH_2,$ and O^- , respectively.

The variation of protonation energies of **1** ($\Delta G_{1\rightarrow 2}$) with **X** may be rationalized in terms of the electron density variation on the metal and oxygen due to the different π -donating abilities of **X**. When a more π -donating **X** is present, electron density is pushed through overlapping π orbitals to metal and oxygen atoms. It causes an increased basicity of hydroxides by destabilizing oxygen lone pair orbitals, facilitating the protonation. This is supported by our calculated data showing that including the solvent effect the oxygen lone pair orbital energies are -7.4, -6.7, -6.4, -6.2, and -5.7 eV for **1-Os-NO₂**, **-H**, **-OH**, **-NH₂**, and **-O**, respectively.

Substituents' influence on hydroxide dissociation from dihydroxide complexes ($\Delta G_{1\rightarrow 3}$) can be rationalized by increased $d_{\pi-p_{\pi}}$ repulsion between metal and hydroxide. The metal-hydroxide bond is thereby weakened, resulting in facile hydroxide dissociation. This is evidenced by an increasing bond length from most π -withdrawing to most π -donating bipyridine ligand, e.g., R(Os-O) = 2.01 Å for **1-Os-NO₂** and 2.10 Å for **1-Os-O**.

We found that for each metal $\Delta G_{3\rightarrow \text{SUB-TS}}$ is remarkably constant regardless of the substituent (**Figure A.4**): for M = Ru $\Delta G_{3\rightarrow \text{SUB-TS}}$ are 25.6, 25.9, 25.5, 25.3, and 26.6 kcal/mol for **X** = NO₂, H, OH, NH₂, and O⁻, respectively, which is a constant around 25.8 kcal/mol. For M = Os and Re with **X** = NO₂, H, OH, and NH₂, $\Delta G_{3\rightarrow \text{SUB-TS}}$ are a constant around 31.1 and 37.8 kcal/mol, respectively.

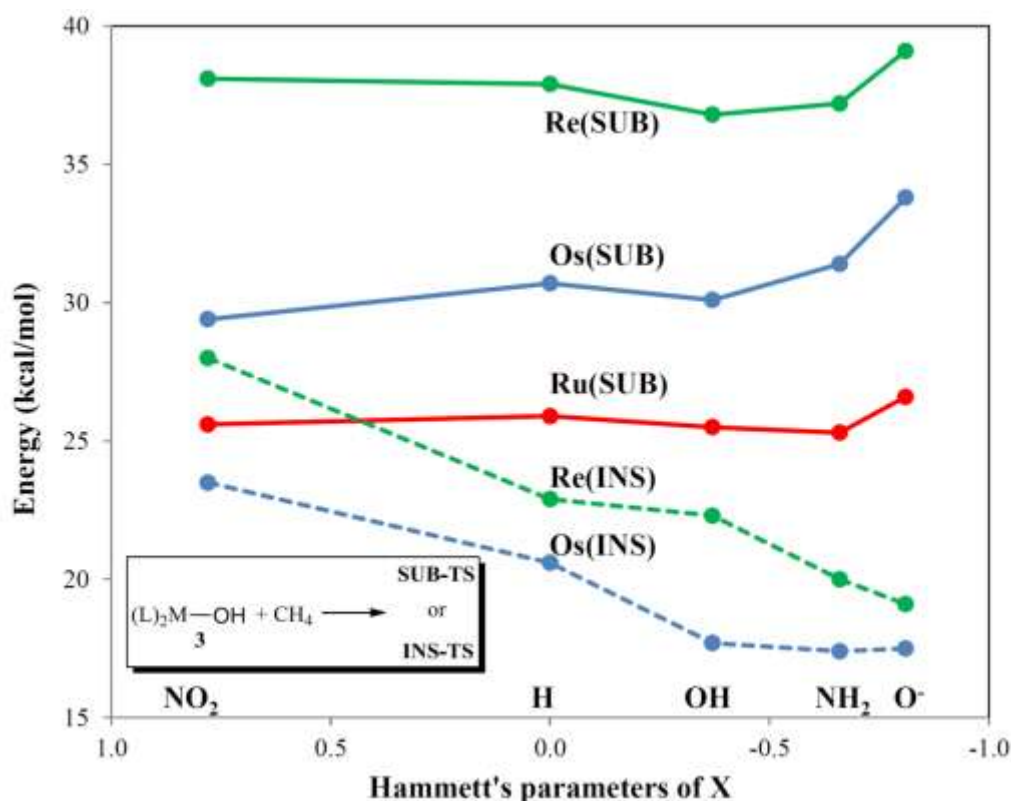


Figure A.4 Substituent effect in methane C-H activation barriers, where five-coordinated intermediate **3** + CH_{4(g)} is the reference point.

The independence of $\Delta G_{3 \rightarrow \text{SUB-TS}}$ on **X** can be rationalized by the frontier molecular orbital interaction. For substitution reactions, both oxygen $p_{\pi} \rightarrow \text{C-H } \sigma^*$ and C-H $\sigma \rightarrow$ metal d_{σ} interactions are important (**Scheme A.3**). With **X** more π -donating, more electron density is pushed toward metal and hydroxide, increasing the orbital energy of oxygen p_{π} and metal d_{σ} , but leaving C-H σ^* and C-H σ orbital energy unchanged. This causes Δ_{C} to decrease (e.g., hydroxide basicity to increase), facilitating C-H activation;

however, it also causes Δ_B to increase, inhibiting C-H activation and resulting in a constant $\Delta G_{3 \rightarrow \text{SUB-TS}}$ (**Figure A.5**).

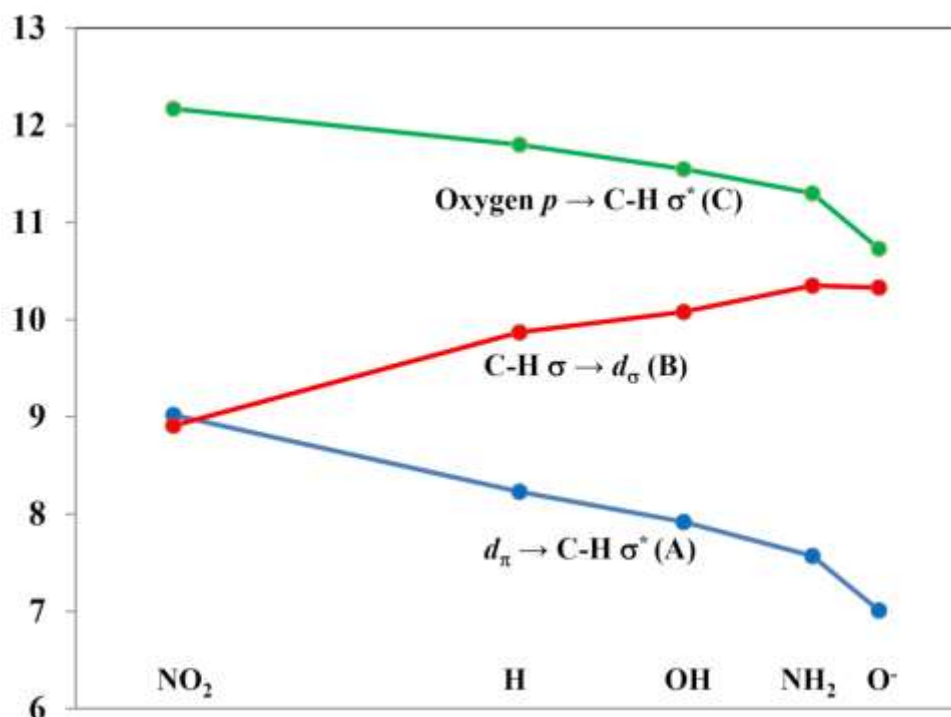


Figure A.5 Substituent influence on three frontier molecular orbital interactions that are responsible for methane C-H cleavage by the five-coordinated intermediate **3**.

On the other hand, $\Delta G_{3 \rightarrow \text{INS-TS}}$ shows a dependence on **X**: with more donating substituents, $\Delta G_{3 \rightarrow \text{INS-TS}}$ decreases (from now on, we discuss the **INS** pathway and ignore **INS'**, since the former is energetically more favorable). For example, $\Delta G_{3 \rightarrow \text{INS-TS}}$ decreases from 23.5 kcal/mol for $\text{X} = \text{NO}_2$ to 17.5 kcal/mol for $\text{X} = \text{O}^\bullet$. This can also be rationalized by frontier molecular orbital interactions. In contrast to the substitution

reaction, the insertion reaction is governed by one interaction: metal $d_{\pi} \rightarrow \text{C-H } \sigma^*$ (ΔA). When the π -donating power of X increases, the occupied metal d_{π} orbital becomes unstable, resulting in a small Δ_A (**Figure A.5**) and therefore small $\Delta G_{3 \rightarrow \text{INS-TS}}$.

Taking the resting state of each case (at pH = 14) as a reference point of the free energy surface, we obtained the total free energy barrier ($\Delta G_{\text{SUB}}^{\ddagger}$ and $\Delta G_{\text{INS}}^{\ddagger}$) and reaction energy (ΔG_{SUB} and ΔG_{INS}) for the C-H activation mechanisms of all cases. The results are summarized in **Figure A.6** and **Figure A.7**, from which promising C-H activation systems can be identified. It should be noted that species **1** is not always the resting state of all reaction mechanisms. For example, the resting state in **Ru-O** case is the aquo complex **2-Ru-O**, but in **Os-O** case the resting state is the pentacoordinate **3-Os-O**.

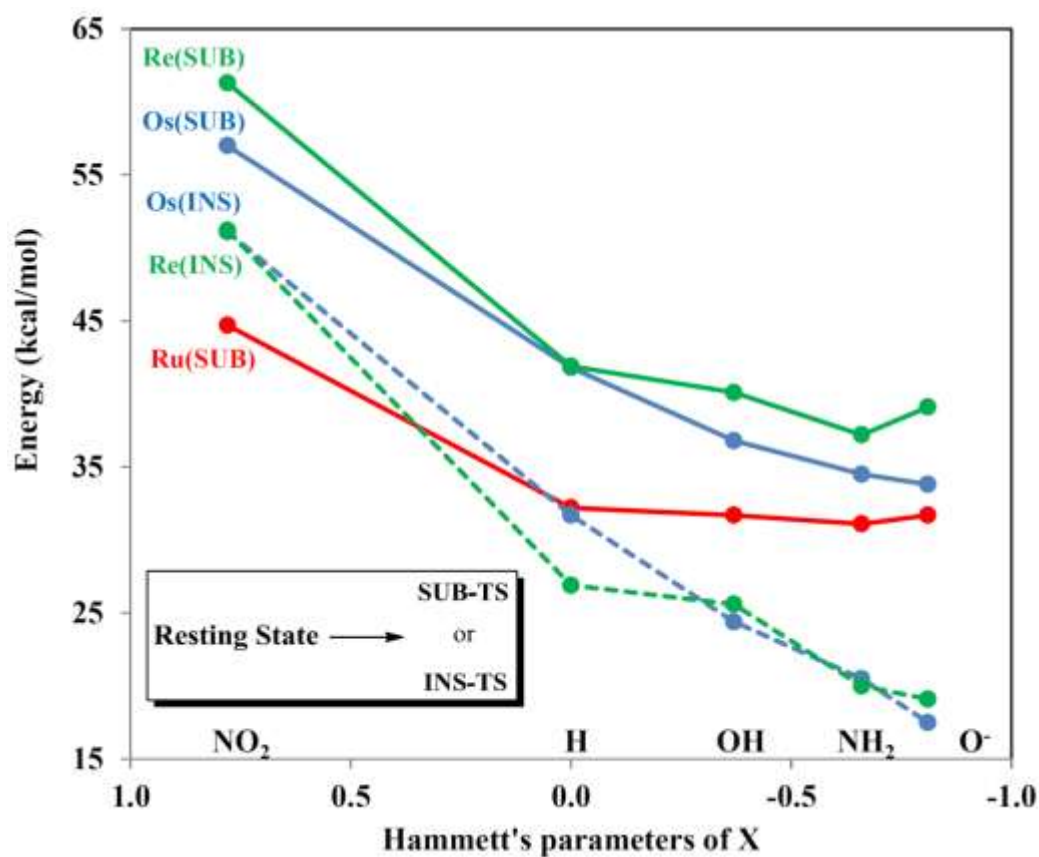


Figure A.6 Substituent effect in the overall methane C-H activation barrier, where the resting state of each system + $\text{CH}_4(\text{g})$ is the reference point (red, blue, and green lines represent Ru, Os, and Re systems, respectively, and solid and dashed line represent substitution and insertion pathway, respectively).

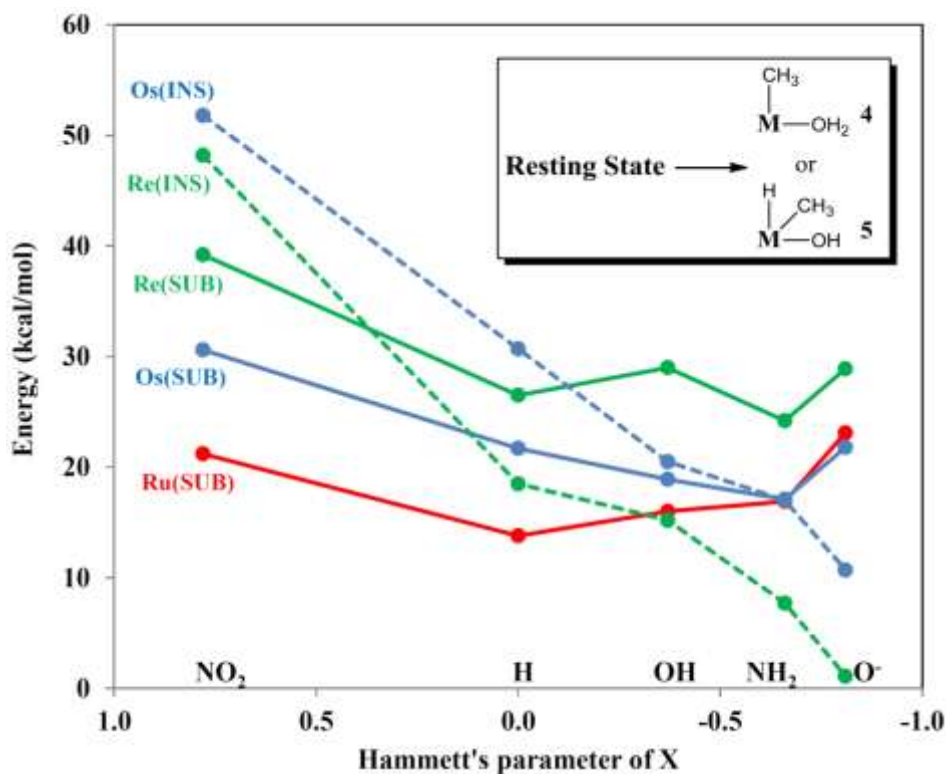


Figure A.7 Substituent effect in the overall reaction energy, where the resting state of each system + CH_{4(g)} is the reference point (red, blue, and green lines represent Ru, Os, and Re systems, respectively, and solid and dashed line represent substitution and insertion pathway, respectively).

For Os and Re systems, the barriers of the substitution pathway are all above 34.5 kcal/mol, suggesting these complexes are not practical for activating methane C-H bond. On the other hand, the insertion pathway poses a much lower total C-H activation barrier than the substitution pathway. Especially for substituents with very negative Hammett parameters, X = NH₂, and O¹⁻, the overall C-H activation barriers are below 30 kcal/mol, suggesting high reactivity at 200°C. Moreover, the corresponding reaction energies (ΔG_{INS}) become less endothermic with donating substituents, especially the **Re-O** case,

whose insertion product **5-Re-O** is only 1.1 kcal/mol higher than the resting state.

This indicates that those are promising for the integration of C-H activation with a subsequent electrophilic functionalization mechanism.

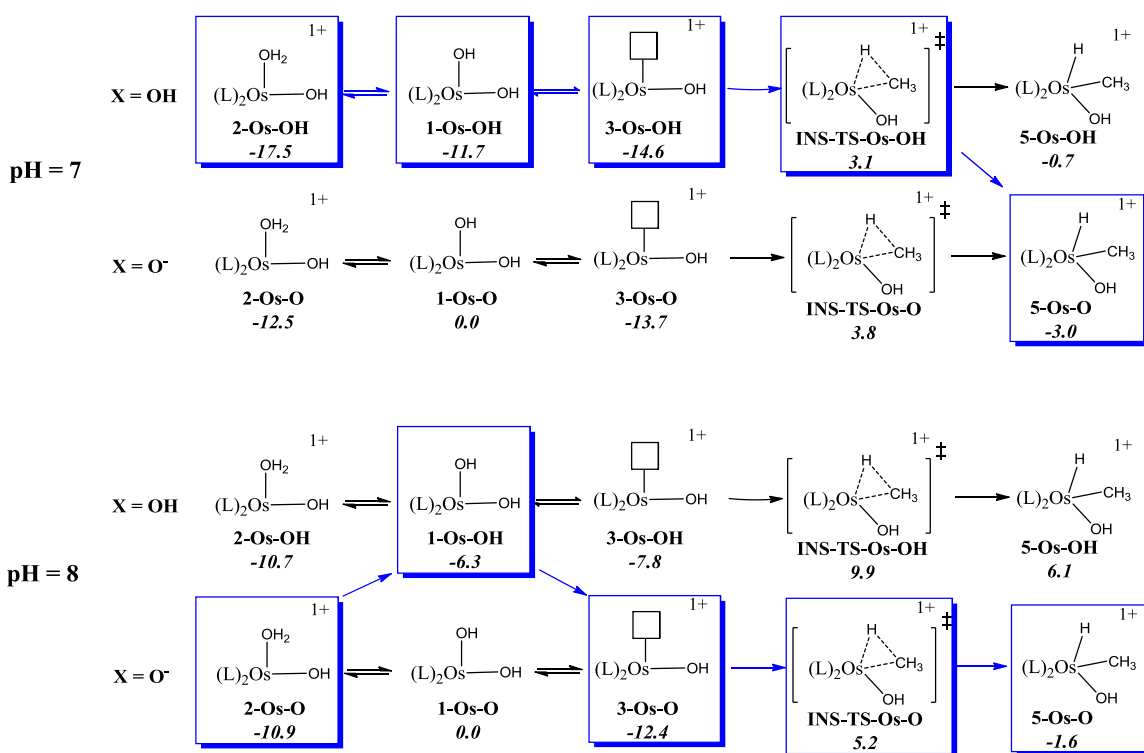
For the Ru system, complexes with **X** = H, OH, NH₂, and O¹⁻, due to having $\Delta G_{\text{SUB}}^{\ddagger}$'s lower than 33.0 kcal/mol and ΔG_{SUB} 's below 25.0 kcal/mol, are also promising for methane C-H activation and oxy-functionalization. Interestingly, the overall methane C-H activation in this system is almost a constant again but only for X = H, OH, NH₂, and O¹⁻. This is due to a similar water dissociation energy ($\Delta G_{2 \rightarrow 3} \approx 5.7$ kcal/mol) from species **2**, the resting state.

Importantly, we found that for all the Os bipyridine systems studied in this work the insertion product is always slightly lower than the transition state. Since catalyzed C-H activation reactions are often demonstrated by H/D exchange reactions between hydrocarbons and deuterated solvents, alkyl intermediates may be reversibly formed without being detected by H/D exchange reactions.

pH-dependent Gibbs Free Energy Surfaces **Os-O** differs from **Os-OH** by one proton on each substituent **X**. Therefore, it is expected that the two Gibbs free energy surfaces are tangled with each other, and at different pH different pathway is responsible for methane C-H cleavage. We found that at pH = 7, **2-Os-OH** is the resting state and **INS-TS-Os-OH** is the low energy transition state, resulting a C-H activation barrier of 20.6 kcal/mol (**Scheme A.6**). When pH value is increased to 8.0, the low energy pathway switched. The resting state is **2-Os-O** and the low energy transition state is **INS-TS-Os-O**, and most importantly, the overall barrier is decreased to 17.6 kcal/mol. This result

suggests that for ligands with protic substituents, the C-H activation barrier can be tuned by pH.

Based on these free energy surfaces, C-H activation rates are not predicted to increase indefinitely with pH, but to have an optimum range. Since the internal substitution and insertion transition states involve one fewer hydroxide than the dihydroxide resting states, an inhibition by hydroxide is expected at high pH.



Scheme A.6

Oxy-Functionalization by Model Oxidant (acac)₂Os^{VI}(O)₂ Since the utility of metal-mediated C-H activation is the generation of an alkyl group more reactive than the substrate, we tested the lability of the M-CH₃ bonds in one potential oxy-functionalization mechanism. To our knowledge, reductive functionalization of Group 9 metal alkyls is rare and unknown for Groups 7 and 8. We have lately identified oxy-functionalization mechanisms amenable to negatively polarized alkyl groups M^{δ+}-R^{δ-}, including the electrophilic attack of peroxide,⁶ H₂SeO₃,⁸ and OsO₄⁷ on methylrhenium moieties. Insertion of SO₂ and other sulfur and selenium electrophiles into M-CH₃ bonds of several metals are known and may lead to new catalytic cycles. Furthermore, Mayer reported low-temperature C-O bond formation mechanisms involving rhenium oxo-alkyl/aryl species.^{30,31} Here we consider the external attack of (acac)₂Os^{VI}(O)₂ (a model for base-stable, air-regenerable electrophilic metal oxo's) on the methyl intermediates above to indicate their reactivity toward electrophiles.

Although the C-H activation pathways leading to seven-coordinate species **5** give lower overall C-H activation barriers and reaction energies for Os and Re systems (for example, $\Delta G_{\text{INS}}^{\ddagger}$ and ΔG_{INS} are only 20.0, and 7.7 kcal/mol for **1-Re-NH₂** + CH₄ → **5-Re-NH₂**), these intermediates may not be suitable for the direct functionalization mechanism considered here. The transfer of hydride, able to form bonds in opposite directions with no geometric strain, is expected to be more facile than the transfer of methyl anion with its directional bond. We used **5-Re-NH₂**, the product of methane C-H activation via the insertion fashion, as an example to demonstrate this point.

The transfer of methyl from **5-Re-NH₂** to (acac)₂Os(O)₂ poses a free energy barrier of $\Delta G_{\text{MT}}^\ddagger = 26.7$ kcal/mol (**Figure A.8** (a)). The transition state, **MT-TS**, has $R(\text{Re-C}) = 2.66$ Å, $R(\text{C-O}) = 1.89$ Å, and $R(\text{Os-O}) = 1.84$ Å. Importantly, integrating this barrier with the previous C-H activation step yields a cumulative barrier of 34.4 kcal/mol. This suggests the potential of this Re complex to participate in a complete catalytic cycle. However, we found the transfer of hydride to be more facile (b). The barrier is only $\Delta G_{\text{HT}}^\ddagger = 6.6$ kcal/mol, 20.1 kcal/mol lower than that of the methyl transfer, with the $R(\text{Re-H}) = 1.83$ Å, $R(\text{H-O}) = 1.35$ Å, and $R(\text{Os-O}) = 1.82$ Å at the transition state **HT-TS**. This indicates that the oxy-functionalization is obviated by this undesired pathway.

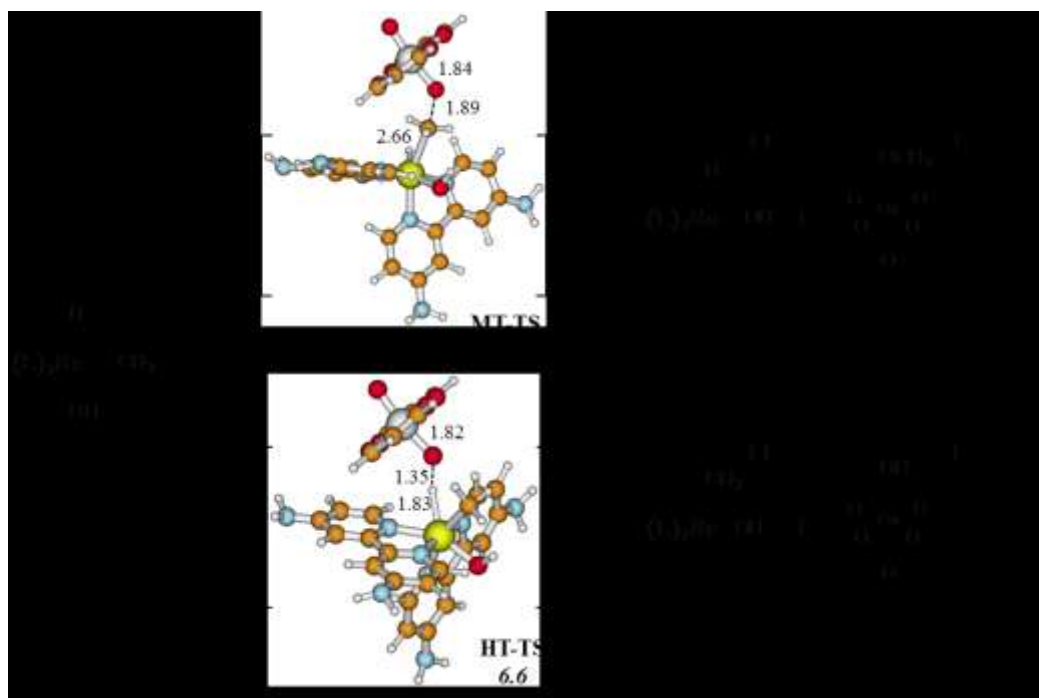


Figure A.8 The free energy surfaces of (a) methyl and (b) hydride transfer from **5-Re-NH₂**, a methane C-H insertion product, to a mode oxidant (acac)₂Os(O)₂. The unit is kcal/mol for energy and angstrom for bond length.

The hydride **5** may proceed to the octahedral intermediate **4** via deprotonation by basic solvent. If so, the insertion pathway may be compatible with functionalization by electrophilic attack. We therefore focused on the octahedral methyl intermediates, which are produced directly by the substitution pathway.

We found that the replacement of metal has a significant impact on the free energy surfaces of (acac)₂Os(O)₂ electrophilic attack on **4-Ru-H**, **4-Os-H**, and **4-Re-H**. The functionalization barrier $\Delta G_{\text{MT}}^{\ddagger}$ is 35.6 kcal/mol for **4-Os-H**, 26.8 kcal/mol for **4-Ru-H**, and only 21.7 kcal/mol for **4-Re-H** (**Figure A.9**). The M-CH₃ bond lengths are 2.59, 2.41, and 2.60 Å, and the O-CH₃ bond lengths are 2.18, 1.83, and 1.77 Å for **MT-TS-Ru-H**, **MT-TS-Re-H**, and **MT-TS-Os-H**, respectively.

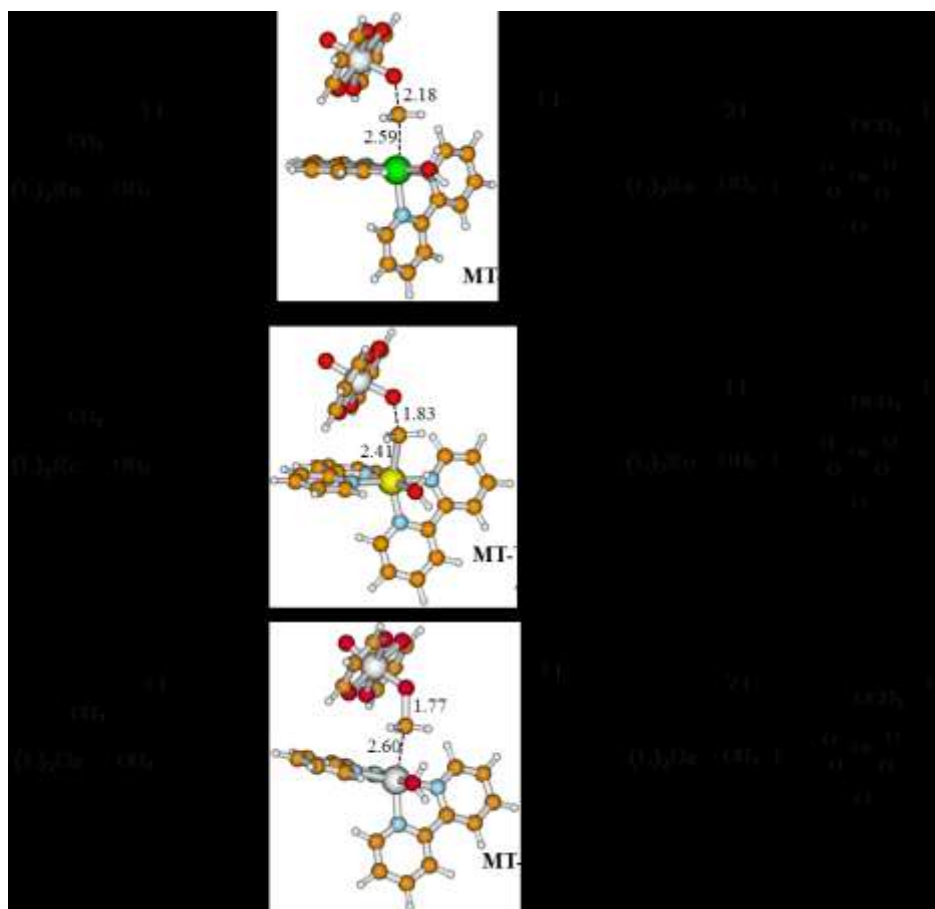


Figure A.9 The free energy surfaces of methyl transfer from **4-Ru-H**, **4-Os-H**, and **4-Re-H** to methyl oxidant $(\text{acac})_2\text{Os}(\text{O})_2$. The unit is kcal/mol for energy and angstrom for bond length.

The barrier of this electrophilic attack is controlled by the electron density at the methyl group of species **4**: a more electron-rich methyl is more susceptible to electrophilic attack. *Here we introduce an important concept that the relative electron density of a methyl group can be determined by its own carbon 1s orbital energy: the more electron-rich the methyl, due to the Coulomb repulsion between valence electrons*

and core electrons, the higher its own carbon $1s$ orbital energy. We found that taking methane in gas phase as a reference, the relative carbon $1s$ orbital (E_{1s}) of **4-Re-H**, **4-Ru-H**, and **4-Os-H** are 21.3, 17.4, and 16.5 kcal/mol, respectively, inversely proportional to the trend in $\Delta G_{\text{MT}}^\ddagger$.

Although the barriers for this elementary step are thermally accessible, the overall C-H activation + functionalization barrier, the energy difference between **MT-TS** and the resting state at pH = 14, is 40.6, 57.3, and 48.2 kcal/mol for **Ru-H**, **Os-H**, and **Re-H**. For the Os and Re systems, the complete reaction is not feasible under thermal conditions due to the high energy of species **4**. Therefore, we focused on the Ru system to study the π -substituent effect of this oxy-functionalization pathway by changing the substituents at the 4 and 4' positions of 2,2'-bipyridine.

We found that the substituent ($\mathbf{X} = \text{NO}_2, \text{H}, \text{OH}, \text{NH}_2, \text{O}^{1-}$) on bipyridine influences the oxy-functionalization as significantly as the metal center (**Table A.2**). $\Delta G_{\text{MTS}}^\ddagger$ are 33.3, 26.8, 24.0, 20.1, and 19.0 for $\mathbf{X} = \text{NO}_2, \text{H}, \text{OH}, \text{NH}_2, \text{O}^{1-}$, respectively, indicating that $\Delta G_{\text{MT}}^\ddagger$ decreases as \mathbf{X} becomes more π -donating. *This is a surprising and important result, because it shows that although the π -influence of substituent \mathbf{X} has no net effect on substitution C-H activation pathways, it does affect the functionalization step, making the Ru bipyridine complexes with strong π -donating \mathbf{X} the best candidates among those in this work.*

Table A.2 Substituent effect the free energy surfaces of oxy-functionalization by methyl transfer from $(\text{bpy})_2\text{Ru}(\text{CH}_3)(\text{H}_2\text{O})$ (**4**) to $(\text{acac})_2\text{Os}(\text{O})_2$ (unit: kcal/mol).

X	4	→	MT-TS	→	9
NO ₂	0.0		33.3		14.7
H	0.0		26.8		1.6
OH	0.0		24.0		-1.2
NH ₂	0.0		20.1		-6.5
O ¹⁻	0.0		19.0		-8.4

Moreover, we found E_{1s} s are 6.9, 17.4, 20.8, 22.7, and 23.1 kcal/mol for **4-Ru-NO₂**, **4-Ru-H**, **4-Ru-OH**, **4-Ru-NH₂**, and **4-Ru-O¹⁻**, inversely proportional to $\Delta G_{\text{MT}}^\ddagger$'s with $R^2 = 0.91$ (**Figure A.10**). This demonstrates that E_{1s} , an easily accessible parameter, can serve as an indicator of electrophilic functionalization barriers within a family of catalysts.

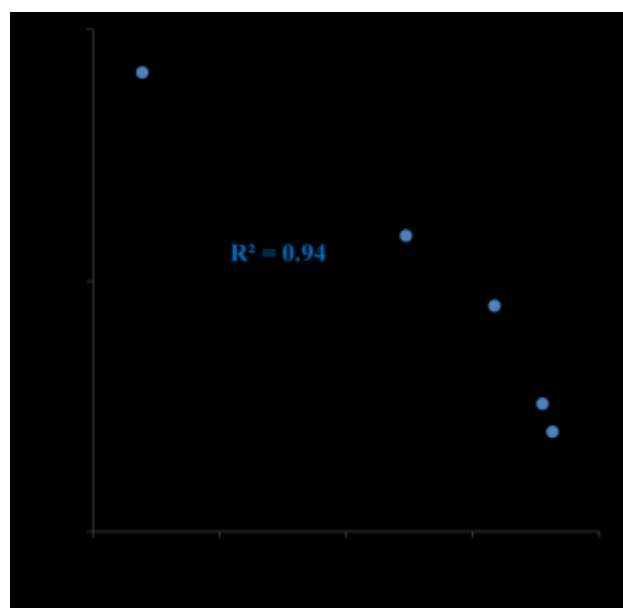
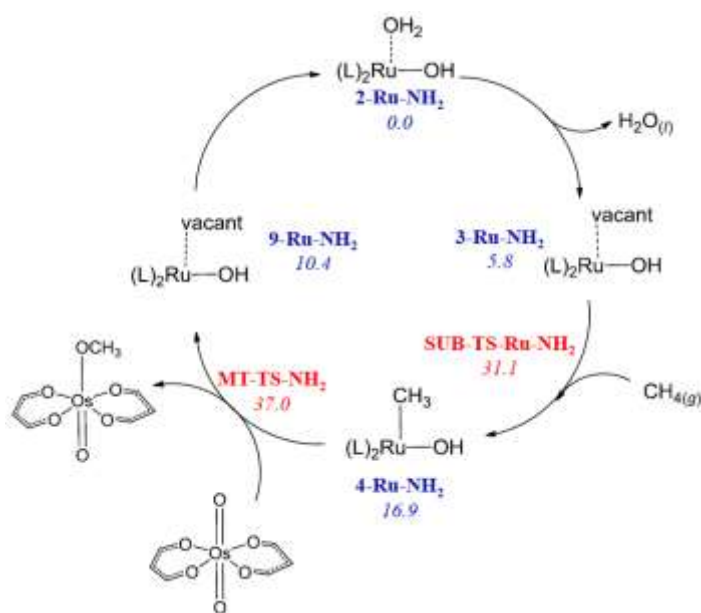


Figure A.10 The relation between methyl carbon 1s orbital energy and methyl transfer barrier (solid circle represents carbon 1s orbital energy in **4**, while hollow circle represents that in **10**).

Potential Catalytic Systems Among those systems that we studied here, Ru bipyridine complexes are more promising than those of Os and Re in activating and functionalizing methane for two reasons. First, they give reasonable methane C-H activation barriers and also give thermodynamically stable products. Second, due to having very different size and energy of $5s$ and $4d$ orbitals, those catalysts cannot activate C-H bond via an insertion fashion. Therefore there is no $(\text{bpy})_2\text{Ru}(\text{OH})(\text{H})(\text{CH}_3)$ seven-coordinated species, which cannot be functionalized through the methyl transfer pathway, since the hydride transfer is much more facile.

Among five Ru bipyridine complexes we studied here, Ru 4,4'-amine bipyridine complex is more encouraging for the methane C-H activation and functionalization process. The resting state of this reaction is $(\text{bpy})_2\text{Ru}(\text{OH})(\text{H}_2\text{O})$ (**2-Ru-NH₂**, **Scheme A.7**). Then a 5.8 kcal/mol free energy cost is needed to remove a water molecule to form a vacancy (**3-Ru-NH₂**) for accommodating methane. Methane C-H bond is cleaved through a substitution fashion with a barrier of 31.1 kcal/mol (compared to the resting state), leading to the formation of a Ru hydroxide methyl complex (**4-Ru-NH₂**), which is 16.9 kcal/mol uphill compared to the resting state. Methyl transfer functionalization step poses a barrier of 37.0 kcal/mol, resulting in **9-Ru-NH₂**, which acquire a water to form the resting state.

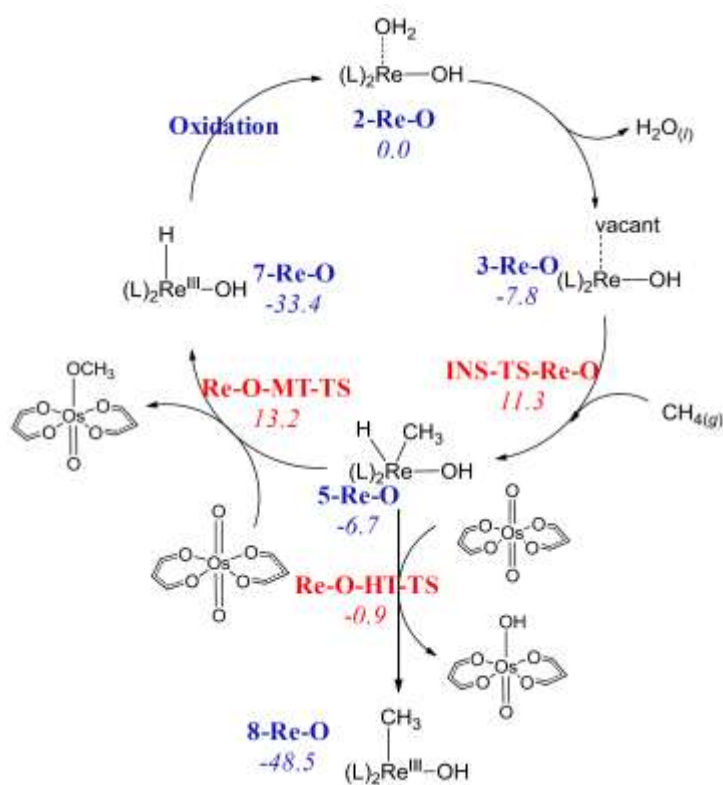


Scheme A.7

Although when reacting with the model oxidant, species **7** (the insertion product) has a lower barrier in transferring the hydride (leading to the undesirable side-product) than in transferring methyl, it is still worth to look at the overall C-H activation and functionalization due to the low C-H activation barrier and reaction energy. We only showed the **Re-O** case, since it gives the lowest methane C-H insertion barrier and reaction energy among all the cases we studied here.

We found the resting state is **3-Re-O** and there is only a 19.1 kcal/mol barrier for it to cleave methane C-H (**Scheme A.8**). Importantly, the C-H activation product, **5-Re-O**, is only 1.1 kcal/mol uphill than the resting state. The methyl at **5-Re-O** is then transferred to the model oxidant with a barrier of only 19.9 kcal/mol leading to **7-Re-O**, a Re(III) complex. This is 1.9 kcal/mol higher than C-H activation barrier and therefore is the rate-determining step. The overall C-H activation + functionalization barrier is only 21.0

kcal/mol and the reaction energy is downhill by 25.6 kcal/mol, both of which indicate this is a kinetically accessible and thermodynamically favorable reaction. However, as we have shown in the previous section, this mechanism is inhibited by a more favorable hydride transfer pathway (with an overall 6.9 kcal/mol barrier, 14.1 kcal/mol lower than that of methyl transfer). If this step can be prevented, this C-H insertion + nonreductive functionalization mechanism can be utilized for the methanol production in room temperatures.



Scheme A.8

A.4 Conclusions

We have studied methane C-H activation and functionalization by Os, Ru, and Re bipyridine complexes by DFT. We found Os/bpy and Re/bpy can activate methane C-H bonds through either a substitution pathway or an insertion pathway, while Ru/bpy can only through a substitution pathway. This is due to Ru, a second row transition metal, having *4d* and *5s* orbitals that are different in size and energy, making the hybridization difficult and therefore resulting in the absence of an insertion pathway.

The displacement of substituents at 4 and 4' positions of 2,2'-bipyridine by $\mathbf{X} = \text{NO}_2$, OH, NH₂, and O⁻ for the Os and Ru systems, and $\mathbf{X} = \text{NO}_2$, OH, and NH₂ for the Re system has a significant influence on C-H activation free energy surfaces. With X being more π -donating, both protonation ($\Delta G_{1\rightarrow 2}$) and hydroxide dissociation energies ($\Delta G_{1\rightarrow 3}$) decrease. This leads to the resting state gradually change from [(bpy)₂M(OH)₂] to [(bpy)₂M(OH)] in Os/bpy and Re/bpy systems and to [(bpy)₂M(OH)(H₂O)] in Ru/bpy. We also found that substitution barriers ($\Delta G_{3\rightarrow \text{SUB-TS}}$) are independent of substituent X, while insertion barriers ($\Delta G_{3\rightarrow \text{INS-TS}}$) decrease as X becomes more π -donating.

For Os/bpy and Re/bpy, the substitution barriers are all above 34.5 kcal/mol, suggesting that they are not practical for activating methane C-H bond. On the other hand, the insertion pathways pose a much lower total C-H activation barrier than the substitution pathway. Especially for substituents with negative Hammett parameters, $\mathbf{X} = \text{NH}_2$, and O¹⁻, the overall C-H activation barriers are below 30 kcal/mol, suggesting high reactivity at 200°C. However the resulting seven-coordinated products are not suitable for the nonreductive functionalization mechanism. The transfer of hydride, able to form

bonds in opposite directions with no geometric strain, is more facile than the transfer of methyl.

For the Ru/bpy, complexes with $X = H, OH, NH_2,$ and O^1 have ΔG_{SUB}^\ddagger 's lower than 33.0 kcal/mol and ΔG_{SUB} 's below 25.0 kcal/mol, suggesting that they are promising for methane C-H activation and oxy-functionalization. Moreover, the resulting products show a strong influence by the substituents on 4 and 4' positions of 2,2'-bipyridine in the nonreductive functionalization reaction. The functionalization barrier decreases as X being more π -donating. *This is a surprising and important result, because it shows that although the π -influence of substituent X has no net effect on substitution C-H activation pathways, it does affect the functionalization step.*

A.5 References

1. Periana, R. A.; Taube, D. J.; Gamble, S.; Taube, H.; Satoh, T.; Fujii, H. *Science* **1998**, *280*, 560.
2. Periana, R. A.; Taube, D. J.; Evitt, E. R.; Loffler, D. G.; Wentrcek, P. R.; Voss, G.; Masuda, T. *Science* **1993**, *259*, 340.
3. Jones, C. J.; Taube, D.; Ziatdinov, V. R.; Periana, R. A.; Nielsen, R. J.; Oxgaard, J.; Goddard, W. A. *Angew. Chem. Int. Ed.* **2004**, *43*, 4626.
4. Periana, R. A.; Mironov, O.; Taube, D.; Bhalla, G.; Jones, C. J. *Science* **2003**, *301*, 814.
5. Muehlhofer, M.; Strassner, T.; Herrmann, W. A. *Angew. Chem. Int. Ed.* **2002**, *41*, 1745.

6. Conley, B. L.; Ganesh, S. K.; Gonzales, J. M.; Tenn, W. J.; Young, K. J. H.; Oxgaard, J.; Goddard, W. A.; Periana, R. A. *J. Am. Chem. Soc.* **2006**, *128*, 9018.
7. Conley, B. L.; Ganesh, S. K.; Gonzales, J. M.; Ess, D. H.; Nielsen, R. J.; Ziatdinov, V. R.; Oxgaard, J.; Goddard, W. A.; Periana, R. A. *Angew. Chem. Int. Ed.* **2008**, *47*, 7849.
8. Tenn, W. J.; Conley, B. L.; Hovelmann, C. H.; Ahlquist, M.; Nielsen, R. J.; Ess, D. H.; Oxgaard, J.; Bischof, S. M.; Goddard, W. A.; Periana, R. A. *J. Am. Chem. Soc.* **2009**, *131*, 2466.
9. Becke, A. D. *Phys Rev A* **1988**, *38*, 3098.
10. Becke, A. D. *J Chem Phys* **1993**, *98*, 5648.
11. Lee, C. T.; Yang, W. T.; Parr, R. G. *Phys Rev B* **1988**, *37*, 785.
12. Francel, M. M.; Pietro, W. J.; Hehre, W. J.; Binkley, J. S.; Gordon, M. S.; Defrees, D. J.; Pople, J. A. *J. Chem. Phys.* **1982**, *77*, 3654.
13. Hehre, W. J.; Ditchfie.R; Pople, J. A. *J. Chem. Phys.* **1972**, *56*, 2257.
14. Hay, P. J.; Wadt, W. R. *J. Chem. Phys.* **1985**, *82*, 299.
15. Zhao, Y.; Truhlar, D. G. *Acc. Chem. Res.* **2008**, *41*, 157.
16. Zhao, Y.; Truhlar, D. G. *Theor. Chem. Acc.* **2008**, *120*, 215.
17. Clark, T.; Chandrasekhar, J.; Spitznagel, G. W.; Schleyer, P. V. *J. Comput. Chem.* **1983**, *4*, 294.
18. Krishnan, R.; Binkley, J. S.; Seeger, R.; Pople, J. A. *J. Chem. Phys.* **1980**, *72*, 650.
19. Martin, J. M. L.; Sundermann, A. *J. Chem. Phys.* **2001**, *114*, 3408.
20. Gross, C. L.; Girolami, G. S. *J. Am. Chem. Soc.* **1998**, *120*, 6605.
21. Gould, G. L.; Heinekey, D. M. *J. Am. Chem. Soc.* **1989**, *111*, 5502.

22. Dobson, J. C.; Meyer, T. J. *Inorg. Chem.* **1988**, *27*, 3283.
23. Dobson, J. C.; Takeuchi, K. J.; Pipes, D. W.; Geselowitz, D. A.; Meyer, T. J. *Inorg. Chem.* **1986**, *25*, 2357.
24. Pipes, D. W.; Meyer, T. J. *Inorg. Chem.* **1986**, *25*, 4042.
25. Feng, Y.; Lail, M.; Barakat, K. A.; Cundari, T. R.; Gunnoe, T. B.; Petersen, J. L. *J. Am. Chem. Soc.* **2005**, *127*, 14174.
26. Tenn, W. J.; Young, K. J. H.; Bhalla, G.; Oxgaard, J.; Goddard, W. A.; Periana, R. A. *J. Am. Chem. Soc.* **2005**, *127*, 14172.
27. Taube, H. *Pure & Appl. Chem.* **1979**, *51*, 901.
28. Slep, L. D.; Pollak, S.; Olabe, J. A. *Inorg. Chem.* **1999**, *38*, 4369.
29. Mann, J. B.; Meek, T. L.; Knight, E. T.; Capitani, J. F.; Allen, L. C. *J. Am. Chem. Soc.* **2000**, *122*, 5132.
30. Brown, S. N.; Mayer, J. M. *J. Am. Chem. Soc.* **1996**, *118*, 12119.
31. DuMez, D. D.; Mayer, J. M. *J. Am. Chem. Soc.* **1996**, *118*, 12416.

A COMPUTATIONAL STUDY ON THE CATALYTIC OXIDATION OF *n*-BUTANE TO MALEIC ANHYDRIDE BY VANADIUM PHOSPHORUS OXIDE

B.1 Project Overview

Maleic anhydride (MA) plays an important role in polymer chemistry. Its main use is in the production of unsaturated polyesters, which find wide application in bodies of boats and cars.¹ MA is predominantly manufactured by the oxidation of *n*-butane over vanadium phosphorus oxide (VPO) catalysts.^{1,2} This catalytic oxidation is the only commercial process that uses alkanes as feedstock.¹

VPO is a unique catalyst compared to others. It has the ability (probably due to its particular crystal structure) to control its oxidation power, converting *n*-butane to MA without the release of intermediates. In contrast, in similar conditions, TiO₂-supported vanadium oxide also activates *n*-butane but converts it to the total oxidation product CO₂.¹ Moreover, in contrast to other selective oxidations which involve less than four electrons, this process involves 14 electrons.

Numerous studies have been directed toward understanding the reaction mechanism underlying this remarkable system, but no clear consensus has emerged.¹⁻³ In order to shed light on this unique catalytic oxidation reaction, We propose to conduct a computational study (based on both quantum mechanics and molecular mechanics) on this system. The initial goal is to get insight into the reaction mechanisms of this catalytic system, and to have strategies for improving the selectivity to MA especially at high *n*-butane conversion rate. The final goal, however, is to design a homogeneous

organometallic catalyst that possesses the same catalytic ability as VPO, based on the insights gained from this computational study.

B.2 Specific Aims

Aim 1: Identify the active sites

Aim 2: Reaction mechanism study

Aim 3: ReaxFF dynamic study

B.3 Background and Significance

The active VPO catalyst is synthesized through a thermal treatment of the precursor $\text{VOHPO}_4 \cdot 0.5\text{H}_2\text{O}$ (hemihydrate) at 683 K under the flow of air containing 1.5% *n*-butane and 10% O_2 .⁴ This treatment lasts for 24 to 48 hours, during which *n*-butane is selectively oxidized to MA. This procedure is stopped when the conversion and selectivity of *n*-butane to MA have reached a steady state. The active VPO catalyst not only has vanadyl pyrophosphate, $(\text{VO})_2\text{P}_2\text{O}_7$ (VPP), as the major component (> 90%) with vanadium in the +4 oxidation state, but also contains a small amount of different phases of vanadyl orthophosphate, VOPO_4 , with vanadium at +5 oxidation state.⁵ Experiments have shown the presence of V^{+5} is crucial for activating *n*-butane C-H bonds and oxidizing furan to MA.⁶

It is generally believed that active VPO is composed of two components: the bulk-layers (**BL**, **Figure B.1**) and the surface-layers (**SL**).^{1,2,7} The structure of the **BL**

resembles that of VPP, and it plays the role of supporting active surface layers. There are neither chemical reactions nor oxygen exchange with **SL** taking place in the **BL**. As a result, its structure and the oxidation state of its vanadium remain unchanged during the reaction. In contrast, experiments have shown that the **SL** is a dynamic surface. It is responsible for oxidizing *n*-butane selectively to MA, during which the surface is gradually reduced and its catalytic power decreases.⁸ The reduced **SL** is then regenerated by reacting with gaseous O₂.

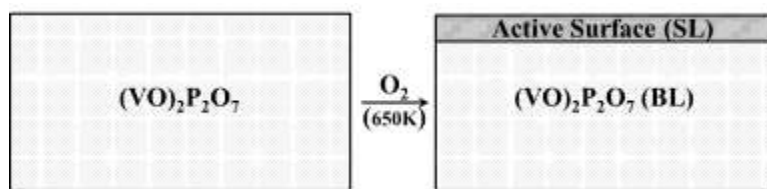


Figure B.1 Schematic description of the composition of the VPO catalyst

Although numerous experimental^{1,2} and theoretical studies⁹⁻¹² have been devoted to understanding this system, the reaction mechanism of this complicated selective oxidation is still unclear. The primary reason is due to absence of well-identified intermediates when the reaction proceeds in industrial conditions (steady-state with less than 2 % of *n*-butane in the air).²

The absence of intermediate has been an important subject of extended research. Centi *et al.* have compared initial reactivity of *n*-butane to butene at non-steady-state conditions, in which they found that the rate of butene oxidation is 50 times faster than

that of *n*-butane.¹³ Considering that the initial concentration of *n*-butane is less than 2 %, which would lead to a much lower concentration of butene, the new formed and highly reactive butene would then be consumed quickly by the catalyst. As a result, the authors rationalize the absence of intermediates due to a kinetic reason. Indeed, with a much higher concentration of *n*-butane (30 % of *n*-butane and less than 10 % of O₂), the authors observe a large amounts of butenes and butadiene.

Similar results were found in nonequilibrium transient experiments. Gleaves *et al.* have developed and applied a TAP (temporal analysis of products) reactor, in which the extremely low pressure conditions facilitate desorption of intermediates, to study the reaction mechanism of *n*-butane oxidation to MA by the VPO catalyst.¹⁴ They observed a series of intermediates including butenes, butadiene, furan, carbon dioxide, carbon oxide, and water. By comparing the time at which the maximum intensity of each intermediate appears, the reaction sequence of *n*-butane evolution to MA was suggested: *n*-butane → butenes → butadiene → furan → MA (the olefinic route, **Figure B.2**).

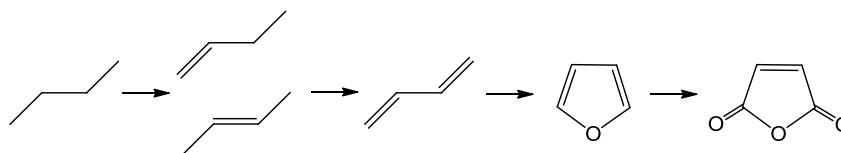


Figure B.2 The reaction sequence of the olefinic route

This proposed sequence was soon challenged by Zhang-Lin *et al.*¹⁵ and recently by

Chen *et al.*,^{16,17} both of whom question the unusual conditions applied in previous studies that lead to the desorption of intermediates. Zhang-Lin *et al.* have performed a kinetic study of oxidation of *n*-butane, butadiene, and furan catalyzed by VPO.¹⁵ By measuring the reactant conversion rate and MA formation rate from those oxidation reactions, the authors suggest that there is a direct and major route from *n*-butane to MA. During the course of this route, the activated *n*-butane forms an alkoxide intermediate on the surface and maintains σ -bonded with the catalyst surface. Importantly, there is no desorption until the final product MA is formed (the alkoxide route **Figure B.3**).

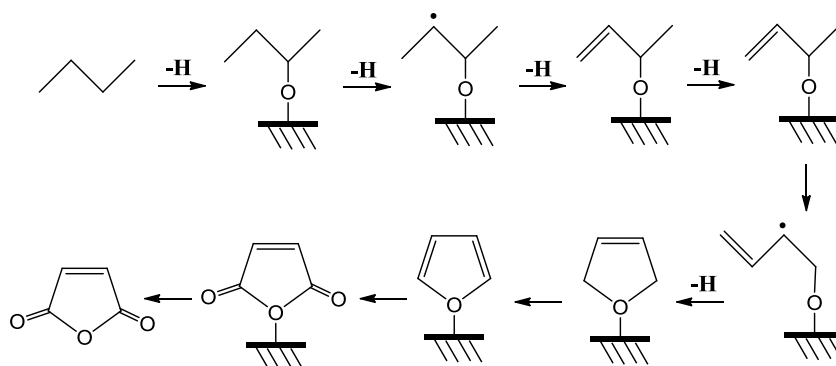
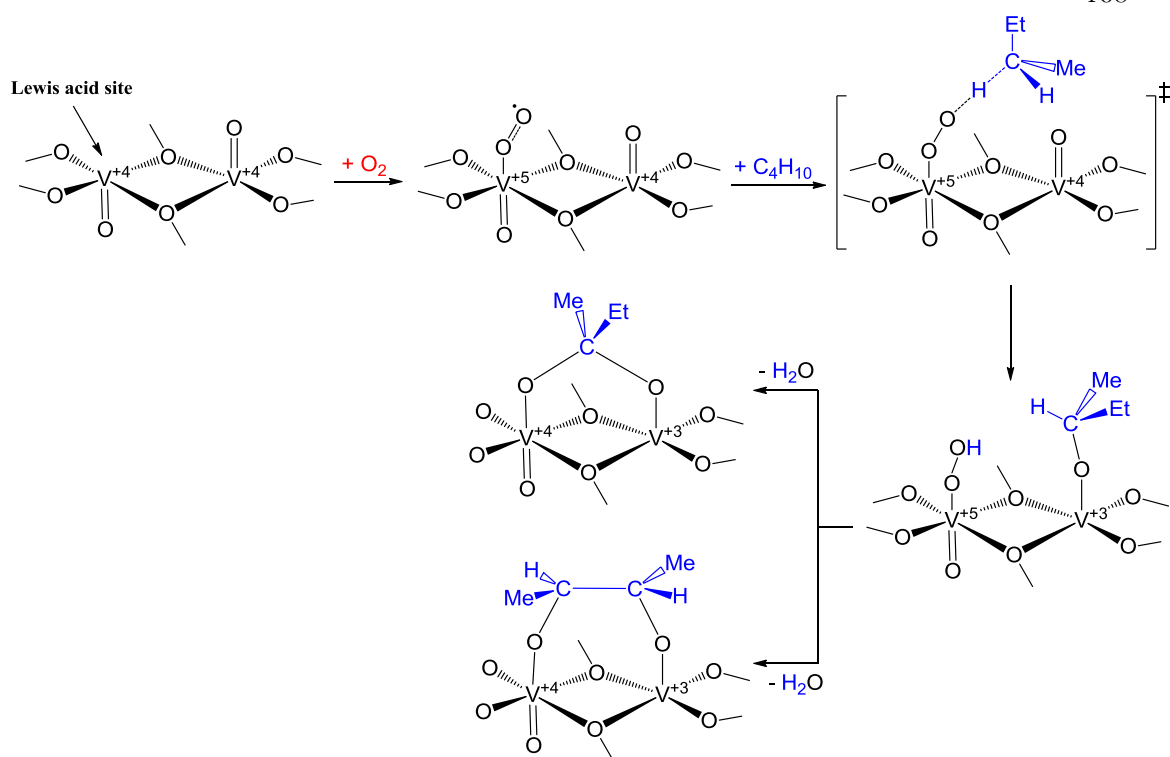


Figure B.3 The reaction sequence of the alkoxide route

Chen *et al.* have studied the reaction of ^{13}C -isotopically labeled *n*-butane on VPO under the conditions that no molecular oxygen is present and vanadium of VPO has an average oxidation state of +4.56.^{16,17} The authors found that butadiene produced from $[1,4\text{-}^{13}\text{C}]n$ -butane is completely scrambled, but the label of maleic acid is largely

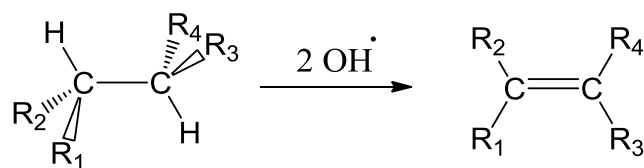
unscrambled. As a result they conclude that butadiene is not an intermediate on the *n*-butane → maleic acid (or MA) route.

Besides the debate in the reaction mechanism, some basic questions such as what sites on the surface are responsible for the activation of *n*-butane C-H bonds remain debated. Grasselli and coworkers have proposed that molecular oxygen can bind with the Lewis acid site of vanadium on the VPP surface forming a superoxo species (**Scheme B.1**).¹⁸ Then the activation of the *n*-butane is achieved by hydrogen abstraction from one of the methylene of *n*-butane by this superoxo species to form a surface bound hydroperoxy and a alkyl radical, which is quickly captured by the adjacent vanadyl group to give a surface bound alkoxy group. Subsequently, the hydroperoxy group abstracts hydrogen either from the same methylene group or from one of adjacent CH_x to generate water and a metal bound ketaloxy or glycoloxy group. This proposed active site is consistent with the transient experimental observation by Gleaves *et al.*,¹⁴ which shows that it is crucial for molecular oxygen to chemisorb through a dissociative and irreversible fashion on the surface to form highly reactive surface oxygen, so that the surface is capable of activating alkane and furan C-H bonds.



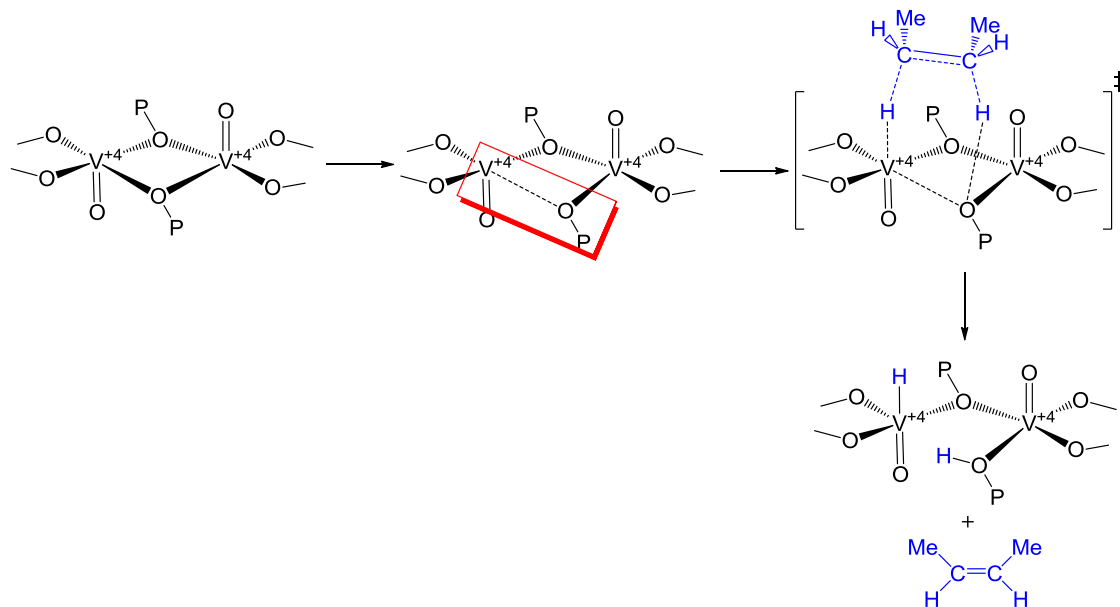
Scheme B.1

Centi *et al.* have performed a kinetic study of the oxidation of a series of C_2 - C_7 alkanes (ethane, propane, *n*-butane, *n*-pentane, *n*-hexane, *n*-heptane, 2-methylbutane, and cyclohexane) on VPO.² The authors found that a good correlation between the rate constant of alkane depletion and the rate constant of the hypothetical reaction of simultaneous abstraction of two hydrogen atoms from the alkane (**Scheme B.2**).



Scheme B.2

As a result, Centi *et al.* proposed that the active site is a $[\text{V}^{+4}\text{---O-P}]$ reactive couple (Scheme B.3, red square), and alkane C-H activation is through a simultaneous two hydrogen abstraction fashion, leading to the formation of alkenes. This is consistent with the experimental observation that the presence of structure defects, which leads to an enhancement of the Lewis acidity of surface unsaturated vanadium ions, increases the rate of *n*-butane consumption.



Scheme B.3

Recently, experiments have shown that in the course of the transformation of $\text{VOHPO}_4 \cdot 0.5\text{H}_2\text{O}$ to VPO ^{5,8} or during the selective oxidation of *n*-butane to MA by VPO ,¹⁹ the small domains of $\alpha_{\text{I-}}$, $\alpha_{\text{II-}}$, β -, δ -, and γ -phases of VOPO_4 are formed on the surface. This opens a possibility that V^{+5} responsible for alkane and furan activation may come from those small amount of VOPO_4 .

Interestingly, when comparing the structures of these VOPO_4 phases to VPP, we find that the significant structural change does not take place at vanadium (**Figure B.4**) but at phosphorus (**Figure B.5**). In both VPP and VOPO_4 , each vanadium atom is bound to four O-P motifs. On the other hand, in VPP each phosphorus atom binds to one O-P and three O-V motifs, whereas in VOPO_4 for all phases phosphorus binds with four O-V motifs.

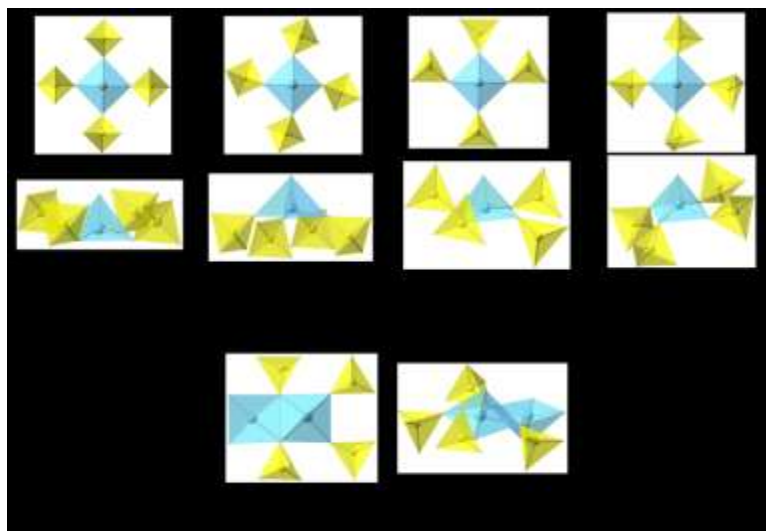


Figure B.4 The local environment of vanadium at different phases of VOPO₄ and VPP.

The blue polyhedron represents the VO₆ or V₂O₈ motif, while the yellow represents PO₄ or P₂O₇.

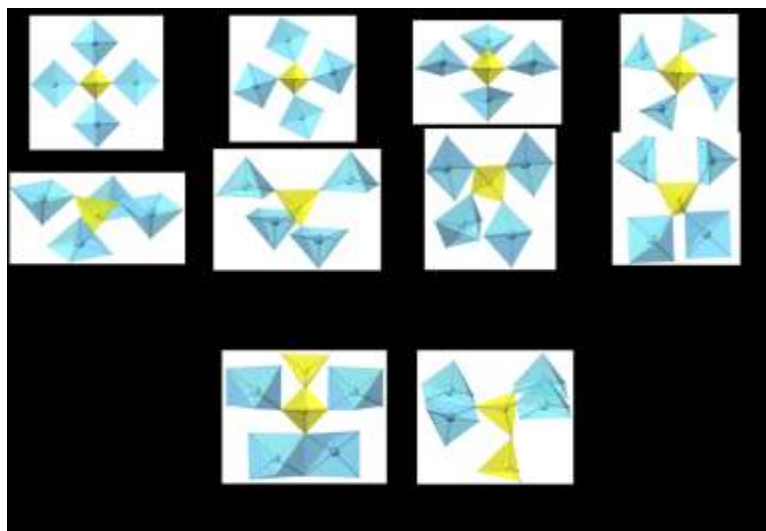
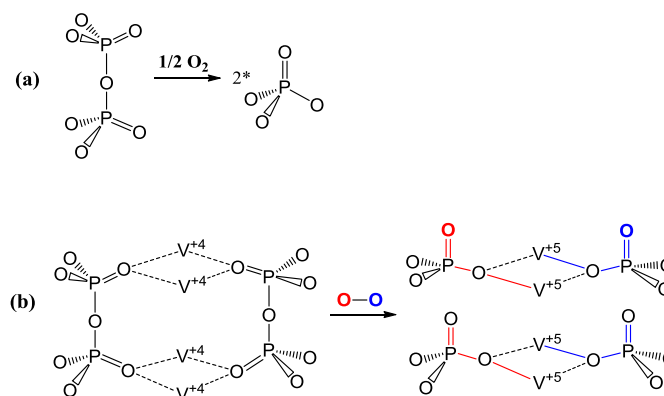


Figure B.5 The local environment of phosphorus at different phases of VOPO₄ and VPP.

The blue polyhedron represents the VO₆ or V₂O₈ motif, while the yellow represents PO₄ or P₂O₇.

This suggests that the oxidation of VPP to VOPO₄ occurs by converting one pyrophosphate to two ortho-phosphates (**Scheme B.4** (a)), rather than by adding gaseous O₂ to vanadium of VPP. In such a way, two of the dative bonds in the V-(O)₂-V motif of VPP becomes covalent, and concurrently two V⁺⁴ are oxidized to V⁺⁵ (b). *The increase of vanadium oxidation state may enhance the reactivity of the surface toward n-butane C-H activation. Thus certain sites on the surfaces of VOPO₄ may be the reactive centers for*

this VPO chemistry. This idea, which has never been explored before, is the heart of this proposition.



Scheme B.4

Numerous industrial and academic efforts have been devoted to this unique catalytic reaction.^{1,3,14,20} Nevertheless, the maximum yield of the process in MA production is still in the range of 60-70%, and it is even lower at high *n*-butane conversions.^{1,21} Improvement of the yield of this catalytic process would bring in enormous economic and environmental benefits. A better understanding the reaction mechanisms is needed to provide better strategies for increasing the selectivity to MA at high *n*-butane conversions. The computational study proposed in this proposition would serve this purpose.

Besides being a solid-gas catalyst, VPO is also a solid-liquid catalyst. Recently, it has been shown that VPO catalyzes the oxidation of cyclohexane to cyclohexanol and cyclohexanone,²² and the oxidation of a variety of alcohols to corresponding ketones²³

both in acetonitrile using hydrogen peroxide as an oxidant at 65 °C. Moreover, VPO also catalyzes the oxidation of *p*-cymene to tertiary cymene hydrogen peroxide at 100 °C using gaseous O₂ as an oxidant.^{24,25} The reaction mechanism from this proposed study may be also suitable for these solid-liquid reactions, and further provide suggestions to increase the yield to the desired products, since the catalyst used in these reactions is the same as the title reaction.

B.4 Preliminary Work

We have applied density functional theory with full three-dimensional periodicity to study VPP, the major component of VPO, focusing on its magnetic properties and electronic structure.²⁶ In this study, we used hybrid function B3LYP, in which exact exchange is included, due to its good performance in predicting band gaps and band structures, and the strength of spin-spin coupling interaction. Our calculations have revealed several important characteristics of this unique material.

Frontier orbital analysis shows that the highest occupied molecular orbitals are composed by unpaired electrons localized at vanadium $3d_{xy}$, and lowest unoccupied molecular orbitals are antibonding orbital combinations of V($3d_{xy}$ or $3d_{yz}$) and O ($2p_x$ or $2p_y$) of vanadyl groups (V=O). Two groups of orbitals are separated by a band gap of 3.61 eV, consistent with experimental observation. Importantly, by varying cell parameter a and monitoring the variation of V-O bond lengths (**Figure B.6** (a)), we found that the V-O bonds of V-(OPO)₂-V are covalent and rigid, whereas the bonds of V-(O)₂-V are fragile and dative (b).²⁶

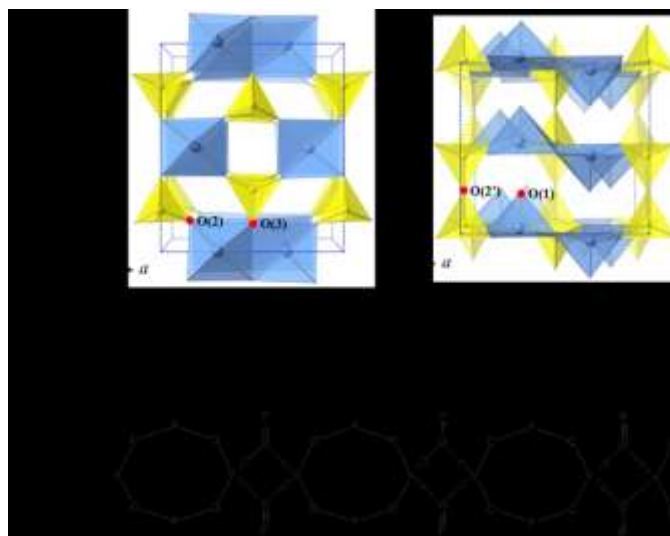


Figure B.6 Polyhedral views of the crystal structure of VPP (the blue polyhedron represents the V₂O₈ motif, while the yellow represents P₂O₇ (a)), and the valence bond description of the bonding along the chain (b).

More recently, we evaluated the C-H activation power of various lattice oxygen atoms on the unoxidized VPP surface by density functional theory (PBE functional). This is accomplished by calculating binding energies of these oxygen atoms to a hydrogen atom. Since, in solid-gas reactions, an alkane C-H bond is usually cleaved through hydrogen abstraction with a transition state close in energy to the radical pair product (**Figure B.7**), these hydrogen binding energies (D_{H}) can simply reflect C-H cleavage barriers: the larger the D_{H} is, the lower the barrier is.

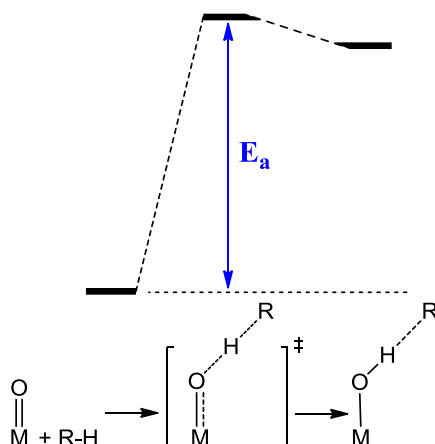
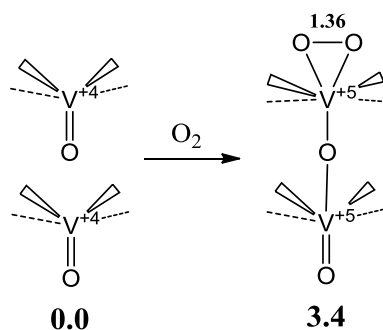


Figure B.7 When R-H bond is activated by a metal-oxo through a hydrogen abstraction pathway, the product is close in energy to the transition state. As a result, E_a can simply be estimated using D_{H} .

Surprisingly, we find that even the largest D_{H} is only 58.2 kcal/mol (V=O(1), **Figure B.6**). Even the weakest C-H bond in *n*-butane still has a bond dissociation energy of 98.3 kcal/mol, and therefore the C-H cleavage by V=O(1) would pose a barrier higher than 40.1 kcal/mol. This projected barrier is far from the experimental number ($E_a = 12.9 \sim 23.6$ kcal/mol, depending on the degree of oxidation of VPO). The barrier will be even higher if the entropy penalty of binding gaseous *n*-butane to the surface is taken into account. Therefore, our calculations clearly indicate that it is not the VPP surface that is responsible for *n*-butane C-H activation.

Some researchers have proposed that gaseous O_2 may adsorb on the VPP surface oxidizing V^{+4} to V^{+5} and forming very reactive oxygen species in the form of peroxy or superoxy.¹⁸ We investigated this possibility and find this scenario unlikely. The unpaired

electrons are localized at very stable $3d_{xy}$ orbitals, and in order to bind with O_2 a great price has to be paid to promote these electrons to high energy orbitals such as $3d_{xz}$ or $3d_{yz}$, so that O_2 can bind with vanadium. The O_2 -V adduct product may be thermodynamically unstable if the new formed V-O bonds are not strong enough to compensate the electron excitation energy. Indeed, our calculations show that binding O_2 to the VPP surface is uphill by 3.4 kcal/mol (electronic energy), although two V^{+4} do oxidize to V^{+5} (**Scheme B.5**).



Scheme B.5 Binding a gaseous O_2 to the VPP surface leads to the oxidation of two V^{+4} to V^{+5} . However, this oxidation is uphill by 3.4 kcal/mol, indicating it is a thermodynamically unstable reaction.

*Those preliminary results and the experimental discovery of $VOPO_4$ on the VPO surface during the *n*-butane selective oxidation again strongly suggest that some surface sites of $VOPO_4$ may be the reactive centers for alkane and furan activation. Therefore, in this proposition the search of active sites for *n*-butane and furan activation will be*

focused on VOPO₄ surfaces.

Method: For electronic and magnetic structure study, all calculations used the B3LYP²⁷⁻²⁹ flavor of density-functional theory (DFT) with full three-dimensional periodicity. B3LYP has been shown to predict band gaps of such inorganic oxides accurately since it provides a better description of the localization of the *d* orbitals.^{30,31} Thus it is expected to yield spin exchange couplings more accurate than nonhybrid methods such as PBE and PW91.^{32,33} To describe the various antiferromagnetic and ferromagnetic spin couplings, we used spin-unrestricted and spatially unrestricted B3LYP (as implemented in the CRYSTAL06 code).

The reciprocal space was sampled with a shrink factor of 3 to define the *k*-point net (eight *k*-points in the irreducible Brillouin zone), which we found is sufficiently dense to provide good numerical accuracy. Each atom is described by all-electron Gaussian type basis sets: 86-411d31G for V, 85-21d1G for P, and 8-411d11G for O, all of which have double zeta plus polarization quality.

In addition, we carried out a full optimization of the VOPO bulk structure, including atomic positions and cell parameters under orthorhombic symmetry. This was done to assess the adequacy of the DFT description of this system. The optimized cell parameters are $a = 7.669 \text{ \AA}$, $b = 9.617 \text{ \AA}$, and $c = 8.453 \text{ \AA}$ at 0K, in a good agreement with experimental numbers at 300K ($a = 7.571 \text{ \AA}$, $b = 9.536 \text{ \AA}$, and $c = 8.362 \text{ \AA}$).³⁴ In addition, we found that the calculated atomic coordinates deviate from the experimental values an RMS of only 0.07 \AA . This indicates that the B3LYP functional and basis set combination provides a good description of VOPO, making it suitable for this study.

For evaluating the C-H activation power of various sites, all the calculations were performed by DFT (PBE³⁵ functional) as implemented in PWSCF. Vanderbilt-type ultrasoft pseudopotentials with a 30 Ry plane-wave cutoff are used to describe spin-polarized wavefunction of the system. Brillouin zone is sampled by a 2×1×1 Monkhorst-Pack k -point net.

B.5 Research design and Methods

Aim 1: Identify the active sites

Experimental Design: We propose to apply density functional theory with the full three-dimensional periodicity to optimize the bulk structure of VPP and the bulk structures of six different phases (α_I , α_{II} , β , γ , δ , and X_1) of VOPO₄, all of which have been found to appear on the VPO surface during the selective oxidation of *n*-butane to MA. There are two proposed goals for these calculations. The first one is to understand how facile the reduction/oxidation reaction is between VOPO₄ and VPP. Since the surface is very dynamic during the reaction, the redox reaction energy should be small between VPP and VOPO₄ that possesses the active sites. The second is to evaluate the performance of the functional that will be applied in this work by the relative stability of those VOPO₄ suggested by experiments (β phase is the most stable one, followed by γ , α_{II} , α_I , and δ).³⁶

It should be noted that among those phases only the crystal structure of α_I , α_{II} , β -phases are known, and the rest are not. Nevertheless, Volta and coworkers have studied the hydration of different phases of VOPO_4 by X-ray diffraction, ^{31}P NMR, and ^{51}V NMR, and proposed the structures of γ - and δ -phases.³⁷ Misono and coworkers have studied the oxidation of VPP by gaseous O_2 by Raman spectroscopy, X-ray photoelectron spectroscopy, and transmission electron diffraction.^{19,38} The authors observed the formation of $X_1\text{-VOPO}_4$ as a thin surface on top of VPP and proposed a structure of this novel phase. Those proposed crystal structures will be starting points for geometry optimizations, and then the NMR spectroscopies and Raman spectroscopies of those optimized structures will be computed and compared to experiments to confirm the computationally predicted structures.

Then we will cleave bulk VOPO_4 along the direction that breaks less strong chemical bonds. This task is very straight forward for α_I - and α_{II} -phase, since they have layered structures and are easily cleaved along the (001) direction, which would break only van der Waals interactions (**Figure B.8**). It may be also an easy task for γ -, X_1 -, and δ -phase of VOPO_4 , since both of them are suggested to have layered structures. However, for β -phase, we will cut the bulk structure along the directions that breaks less covalent bond. Since the cleavage would unavoidably break strong covalent bonds, we will use hydrogen to saturate the broken chemical bonds.

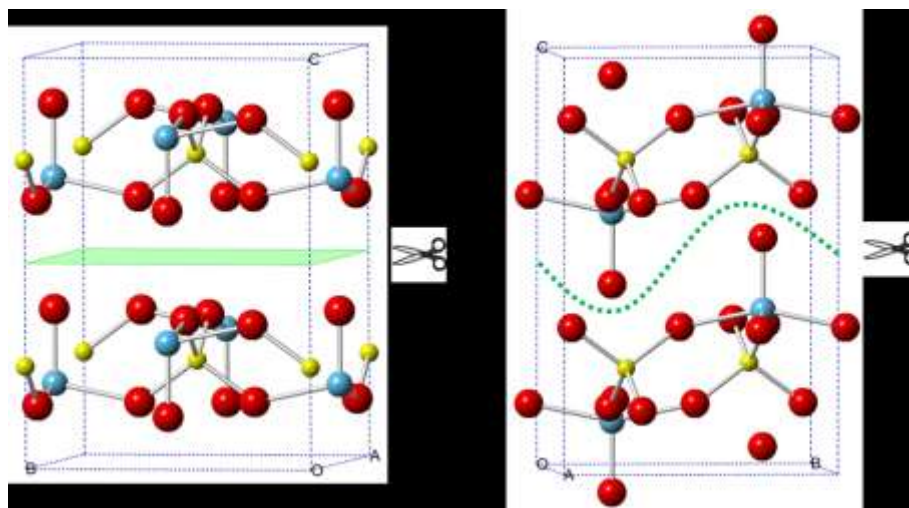
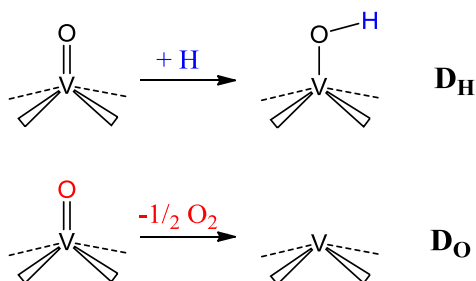


Figure B.8 The crystal structures of α_I - and α_{II} -VOPO₄ and the cleavage direction that would lead to the most stable surfaces.

After determining the most stable surfaces for each VOPO₄ phase, we will evaluate (1) the C-H activation power and (2) the oxidation power of each surface oxygen and vanadium. This is achieved by computing their (1) binding energy to a hydrogen atom (D_H , **Scheme B.6**) and (2) desorption energy of a surface oxygen atom to form 0.5 mole of O₂ (D_O). Since during the selective oxidation of *n*-butane to MA, eight hydrogen atoms are removed from and three oxygen atoms are inserted into the substrate, the active sites for C-H activation should possess a largest D_H and the reactive centers for oxy-functionalization should have the smallest D_O .



Scheme B.6

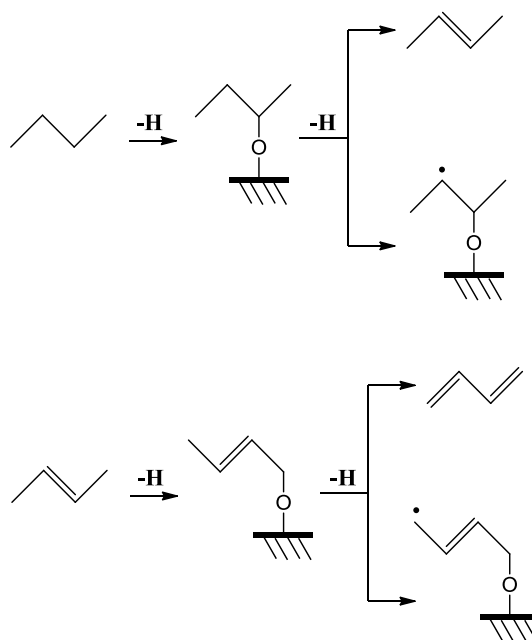
Although for the search of the active sites for *n*-butane C-H activation we will calculate the binding energy of not only surface oxygen but also vanadium to a hydrogen atom, we don't expect that any vanadium would possess a strong V-H bond. This is because that the first row and early transition metal always forms a weak bond with hydride or alkyl.

Method: For evaluating the C-H activation power of various sites, all the calculations will be performed by DFT (PBE functional) as implemented in the PWSCF. Brillouin zone is sampled by a different density of Monkhorst-Pack *k*-point net depending on the volume of bulk structure. Vanderbilt-type ultrasoft pseudopotentials with a 30 Ry plane-wave cutoff are used to describe wavefunction of the system.

Aim 2: Reaction mechanism study

Experimental design: We propose to study the reaction mechanism of selective oxidation of *n*-butane to MA. As stated in the previous section, based on experimental

evidence two very different reaction mechanisms have been proposed. In this proposition, we will focus on the olefinic route mechanism, since the experiments based on which this mechanism is proposed are sound. However, in some of the individual steps, such as *n*-butane \rightarrow butene and butene \rightarrow butadiene, the alkoxide route will be also evaluated and compared to the potential energy surfaces from the olefinic route (**Scheme B.7**).

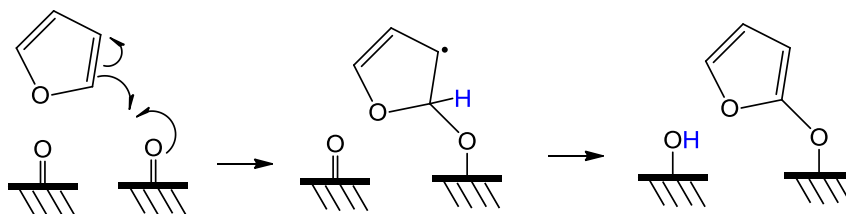


Scheme B.7

We will first focus on two individual reactions on VOPO_4 surfaces: *n*-butane \rightarrow butenes, and furan \rightarrow MA. This is because that the transient experiments using TAP reactors have shown that a very reactive oxidized surface is needed for the two steps.¹⁴

Then we will also study the other two individual reactions: butene \rightarrow butadiene, and butadiene \rightarrow furan. Since experiments have shown that the last two reaction steps can proceed not only on the oxidized surface but also on the unoxidized surface,¹⁴ we will study those reactions use both VOPO₄ and VPP surfaces.

We would expect the first step for *n*-butane \rightarrow butenes is a hydrogen abstraction by surface oxygen; however, it may not be the case for furan activation. The C-H bond of furan is 20 kcal/mol stronger than that of *n*-butane, and therefore a direct hydrogen abstraction would pose a high barrier and thus is unlikely. We will expect the furan is activated by binding its C1 to surface oxygen so that an unpaired electron is localized at C2, which is followed by hydrogen abstraction from C1 by another surface oxygen atom (Scheme B.8).



Scheme B.8

Method: For evaluating the C-H activation power of various sites, all the calculations were performed by DFT (PBE functional) as implemented in the PWSCF. Vanderbilt-type ultrasoft pseudopotentials with a 30 Ry plane-wave cutoff are used to describe wavefunction of the system. Brillouin zone is sampled by a $2 \times 1 \times 1$ Monkhorst-Pack *k*-

point net. Transition states of the reaction pathways are located by the nudged elastic band (NEB) with climbing image technique.

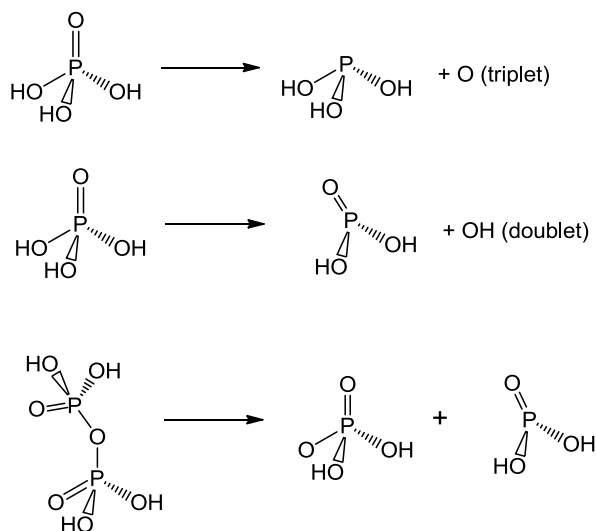
Aim 3: ReaxFF dynamic study

Experimental design: We will develop a new set of ReaxFF force field parameters (**VPO-CHO**) for studying the dynamics of this catalytic system. This requires a force field that can provide (1) accurate description of interactions inside vanadium oxide (**VO**), (2) accurate description of interactions between vanadium oxide and hydrocarbons (**VO-COH**), (3) accurate description of interactions inside phosphorus oxide structures (**PO**), and (4) accurate description of the interactions between vanadium oxide and phosphorus oxide (**VO-PO**).

Fortunately, Chenoweth *et al.*³⁹ have developed a set of ReaxFF parameters to study the reactions of hydrocarbons with vanadium oxide catalysts, in which **VO** and **VO-COH** have been well parameterized. In order to complete this **VPO-CHO** force field what we will include more QM potential energy surfaces describing interactions inside phosphorus oxide (**PO**) and the interaction between vanadium oxide and phosphorus oxide (**VO-PO**) into the training set.

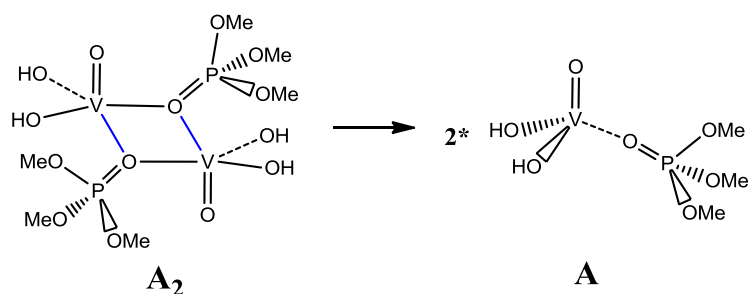
We will include at least three QM potential energy surfaces into the training set to describe the P-O covalent bond interaction. Those surfaces are (1) the dissociation of oxygen atom from O=P(OH)_3 , (2) the dissociation of OH radical from O=P(OH)_3 , and (3) the dissociation of $(\text{OH})_2\text{OP-O-PO(OH)}_2$ to O=PO(OH)_2 and O=P(OH)_2 (**Scheme B.9**). Besides, we will also include several QM angle bending surfaces to describe O-P-O and

O=P-O covalent angle interactions. Moreover the QM equations of state of two phosphorous oxide bulk (P_2O_5), in which phosphorous oxide forms a layered structure, will be also included into the training set.



Scheme B.9

For enabling ReaxFF to describe the interaction between **VO** and **PO**, we will include QM potential energy surfaces of (1) the dissociation of a four-membered VPO cluster (**A₂**, **Scheme B.10**), (2) the equation states of VPP and six different phases of $VOPO_4$, and importantly (3) the redox reaction energies of $VPP + O_2 \rightarrow VOPO_4$. The inclusion of these QM data should be able to provide an excellent training set for parameterized the ReaxFF.



Scheme B.10

Once the ReaxFF parameters are successfully optimized, we will apply them to study the dynamics of the catalytic system. At least five molecular dynamic simulations will be performed including (1) the oxidation of VPP to $VOPO_4$ by gaseous O_2 , (2) the oxidative hydrogenation (ODH) of *n*-butane to butenes, (3) ODH of butenes to butadiene, (4) the oxidation of butadiene to furan, and (5) the oxidation of furan to MA. It should be noted that we plan to study the dynamics of each individual reaction step instead of the complete catalytic reaction n -butane \rightarrow MA, because the study of the whole reaction would need a large time scale (\sim second), but the study of each step would take a much smaller time scale (\sim nanosecond).

Method: NVT MD simulations will be performed to study the individual step in the selective oxidation of *n*-butane to MA. A time step of 0.25 fs will be used and the temperature of the simulation box will be controlled by a Berendsen thermostat with a temperature-damping constant of 0.1 ps.

In order to accelerate MD simulations but in the same time avoid the melting of the catalyst, we will use a dual-temperature thermostat keeping the V, P, and O atoms

associated the catalyst at 600 K, while the C, H, and O atoms associated with the substrates at 2000 K.

B.6 References

1. Hodnett, B. K. *Heterogeneous Catalytic Oxidation*; John Wiley & Sons Ltd: New York, NY, 2000.
2. Centi, G.; Trifiro, F.; Ebner, J. R.; Franchetti, V. M. *Chem. Rev.* **1988**, *88*, 55.
3. Ballarini, N.; Cavani, F.; Cortelli, C.; Ligi, S.; Pierelli, F.; Trifiro, F.; Fumagalli, C.; Mazzoni, G.; Monti, T. *Top. Catal.* **2006**, *38*, 147.
4. Horowitz, H. S.; Blackstone, C. M.; Sleight, A. W.; Teufer, G. *Appl. Catal.* **1988**, *38*, 193.
5. Hutchings, G. J.; Desmartin-chomel, A.; Olier, R.; Volta, J. C. *Nature* **1994**, *368*, 41.
6. Coulston, G. W.; Bare, S. R.; Kung, H.; Birkeland, K.; Bethke, G. K.; Harlow, R.; Herron, N.; Lee, P. L. *Science* **1997**, *275*, 191.
7. Hodnett, B. K.; Delmon, B. *Ind. Eng. Chem. Fundam.* **1984**, *23*, 465.
8. Volta, J. C. *Catal. Today* **1996**, *32*, 29.
9. Thompson, D. J.; Ciobica, I. M.; Hodnett, B. K.; van Santen, R. A.; Fanning, M. O. *Surf. Sci.* **2003**, *547*, 438.
10. Haras, A.; Duarte, H. A.; Salahub, D. R.; Witko, M. *Surf. Sci.* **2002**, *513*, 367.
11. Witko, M.; Tokarz, R.; Haber, J.; Hermann, K. *J. Mol. Catal. A:Chem.* **2001**, *166*, 59.
12. Schiott, B.; Jorgensen, K. A.; Hoffmann, R. *J. Phys. Chem.* **1991**, *95*, 2297.

13. Centi, G.; Fornasari, G.; Trifiro, F. *J. Catal.* **1984**, *89*, 44.
14. Gleaves, J. T.; Ebner, J. R.; Kuechler, T. C. *Catal. Rev. Sci. Eng.* **1988**, *30*, 49.
15. Zhang-Lin, Y.; Forissier, M.; Sneed, R. P.; Vadrine, J. C.; Volta, J. C. *J. Catal.* **1994**, *145*, 256.
16. Chen, B.; Munson, E. J. *J. Am. Chem. Soc.* **2002**, *124*, 1638.
17. Chen, B.; Munson, E. J. *J. Am. Chem. Soc.* **1999**, *121*, 11024.
18. Agaskar, P. A.; Decaul, L.; Grasselli, R. K. *Catal. Lett.* **1994**, *23*, 339.
19. Koyano, G.; Okuhara, T.; Misono, M. *J. Am. Chem. Soc.* **1998**, *120*, 767.
20. Centi, G. *Catal. Today* **1993**, *16*, 5.
21. Batiot, C.; Hodnett, B. K. *Appl. Catal. A General* **1996**, *137*, 179.
22. Pillai, U. R.; Sahle-Demessie, E. *Chem. Commun.* **2002**, 2142.
23. Pillai, U. R.; Sahle-Demessie, E. *Appl. Catal. A general* **2004**, *276*, 139.
24. Makgwane, P. R.; Ferg, E. E.; Billing, D. G.; Zeelie, B. *Catal. Lett.* **2010**, *135*, 105.
25. Makgwane, P. R.; Ferg, E. E.; Zeelie, B. *Chemcatchem* **2011**, *3*, 180.
26. Cheng, M. J.; Nielsen, R. J.; Tahir-Kheli, J.; Goddard, W. A. *Phys. Chem. Chem. Phys.* **2011**, *13*, 9831.
27. Becke, A. D. *Phys. Rev. A.* **1988**, *38*, 3098.
28. Becke, A. D. *J Chem Phys* **1993**, *98*, 5648.
29. Lee, C. T.; Yang, W. T.; Parr, R. G. *Phys Rev B* **1988**, *37*, 785.
30. Muscat, J.; Wander, A.; Harrison, N. M. *Chem. Phys. Lett.* **2001**, *342*, 397.
31. Perry, J. K.; Tahir-Kheli, J.; Goddard, W. A. *Phys Rev B* **2001**, *6314*, 144510.
32. Martin, R. L.; Illas, F. *Phys. Rev. Lett.* **1997**, *79*, 1539.
33. Munoz, D.; Harrison, N. M.; Illas, F. *Phys Rev B* **2004**, *69*, 085115.

34. Saito, T.; Terashima, T.; Azuma, M.; Takano, M.; Goto, T.; Ohta, H.; Utsumi, W.; Bordet, P.; Johnston, D. C. *J. Solid State Chem.* **2000**, *153*, 124.
35. Perdew, J. P.; Burke, K.; Ernzerhof, M. *Phys Rev Lett* **1996**, *77*, 3865.
36. Xue, Z. Y.; Schrader, G. L. *J. Phys. Chem. B* **1999**, *103*, 9459.
37. Benabdelouahab, G. F.; Volta, J. C.; Olier, R. *J. Catal.* **1994**, *148*, 334.
38. Shimoda, T.; Okuhara, T.; Misono, M. *Bull. Chem. Soc. Jpn.* **1985**, *58*, 2163.
39. Chenoweth, K.; van Duin, A. C. T.; Persson, P.; Cheng, M. J.; Oxgaard, J.; Goddard, W. A. *J. Phys. Chem. C* **2008**, *112*, 14645.

